PROCEEDINGS

ISBN 978-618-84774-3-8

ISSN 2654-2099

International EEITE-2020 Symposium

eeite2020.hmu.gr

2nd International Symposium in Electronic Engineering, Information Technology & Education

12-14 October 2020

Hellenic Mediterranean University

Dept. of Electronic Engineering

Chania, Crete, Greece

ONLINE (due to COVID)

Proceedings of the 2nd International Symposium in **E**lectronic **E**ngineering, **I**nformation **T**echnology & **E**ducation EEITE-2020, October 12-14, Chania, Crete, Greece

eeite2020.hmu.gr

Hosted by the Department of Electronic Engineering, Hellenic Mediterranean University

ISSN 2654-2099 **ISBN 978-618-84774-3-8**

Copyright - Department of Electronic Engineering, Hellenic Mediterranean University.

TOPICS

ELECTRONICS & OPTOELECTRONICS

Electronics

Circuits and Systems, Analog Circuits, Digital Circuits, Mixed Signal Circuits, Nonlinear Circuits and Systems, Sensing and Sensor Networks, Filters and Data Conversion Circuits, RF and Wireless Circuits, Photonic and Optoelectronic Circuits, Low Power Design and VLSI Physical Design, Biomedical Circuits, Assembly and Packaging, Test and Reliability, Advanced Technologies (i.e. MEMS and Nano-electronic Devices) Signal Processing, Signal Processing Theory, Digital Signal Processing Algorithms, Digital Filter Design & Implementation, Array Processing, Adaptive Signal Processing, Audio, Speech and Language Processing, Image Processing, Video Processing, Medical Signal Processing & Medical Imaging Electrical Power Systems, Power Engineering and Power Systems, Electromagnetic Compatibility, Energy Conversion, High Voltage Engineering and Insulation, Power Delivery, Power Electronics, Illumination

Optoelectronics

Physics of semiconductors, Optoelectronics, Nanostructures, Semiconductor Devices, Electro-optics, Optical fiber communications, Optical Interference Coatings and Color, Optical Imaging, Quantum Optics, Optical Physics, Photoelectric Effect, Compound Semiconductor Devices and Circuits, Laser Diodes, Electrical Conduction, Laser Matter-Plasma Interaction, Pulsed Power Optoelectronic Plasma Devices, Electronic Band Structure, Nanodevices & Nanosensors, Nanoelectronics, Nanophotonics and Optics, Nanosensoring in diagnostics and industry, Nanotechnology for Energy and the Environment, Nanofabrication, Nanocomposites and Multifunctional Materials, Sensors, Condensed Matter Theory, Nitride Semiconductors, Carbon: Nano tubes and Graphene, Organic semiconductors, Electron devices and applications, Material Science, Natural Nano structured Materials, Bio Optics, Magnetic Materials

TELECOMMUNICATIONS

Small Antennas

Adaptive (smart) arrays, Antennas for 5G communications, Antenna measurements, Antennas on/in IC packages, Body-Centric Antennas, Broadband antennas, Conformal antennas, Magnetic Nanoparticles, Graphene or Carbon-nanotubes in Antennas, Measurements for SAR of handheld devices, MEMS/nano technology for antennas, Millimeter-wave/Terahertz antennas, Modeling and simulations, Non-Foster/active elements, On-chip antennas, Reconfigurable antennas, Reflectarrays, Ultra-wideband (UWB) antennas, Wearable antennas, 3D printed antennas and structures

Innovative Structures

Analysis and design of EM materials, Artificial magnetic conductors (AMC), Electromagnetic anisotropy, Electromagnetic bandgap (EBG) structures, Frequency selective surfaces (FSS), Fractal Structures, Single and double negative metamaterials, Electromagnetic Skins: Epidermal, Flexible and Stretchable Antennas, Sensing Substrates, Automotive systems, Biomedical and Healthcare applications, Bluetooth/WLAN (PDAs, laptops), Energy harvesting, Hyperthermia and RF Ablation, GPS systems, Medical Diagnostic and Therapeutic Applications, Millimeter-wave/terahertz communications and imaging, MIMO systems

Applications

RFID antennas and Wireless Sensing systems, Software-defined / cognitive radio, Satellite communications, UWB communications, WBAN systems, Wireless communication systems (handheld devices, base stations), Wireless power transmission and harvesting for implanted systems, 5G communication systems, Simultaneous transmit and receive systems

AUTOMATION & INFORMATICS

Computers and Information Technology
Computer Architecture, Computational Biology and Bioinformatics, Knowledge and Data Engineering, Learning Technologies, Multimedia Services and Technologies, Mobile Computing, Parallel/Distributed Computing and Grid Computing, Pattern Analysis and Machine Intelligence, Software Engineering, Visualization and Computer Graphics

Controls
Control Theory and Applications, Adaptive and Learning Control System, Fuzzy and Neural Control, Mechatronics, Manufacturing Control Systems and Applications, Process Control Systems, Robotics and Automation, Control Theory and Applications, Visual Control, Machine Learning, Intelligent Systems and Approach, Modelling and simulation

ENVIRONMENTAL ENGINEERING

Renewable Energy Sources, Smartgrids Technologies & Applications, Smart grid for distributed energy resources, Smart grid in interdependent energy infrastructures, Smart grid for intelligent monitoring and outage management, Smart grid applications and technologies, Smart grid for plug-in vehicles and low-carbon transportation alternatives, Smart grid for cyber and physical security systems, Energy Management and Environmental issues, Hybrid Power Systems, Distributed and Co-Generation Systems, Wind Energy Systems, Solar Energy Systems, Hydro Power Plants, Hydrogen Systems and Fuel Cell, Power Market and Power System Economics

ENGINEERING EDUCATION & STEM

Computational Intelligence, Mobile computing, Ubiquitous and pervasive computing, Serious games, Educational Robotics, Smart educational technology, Human Computer Interaction, Public understanding of Science, Innovative teaching in STEM Disciplines, Modelling and model-based reasoning, Curricular programs that integrate STEM, Project based learning, Conversion of knowledge, Women and STEM disciplines, Didactic transpositions, Pedagogical aspects of educational technology.

COMMITTEES

Organizing Committee

– Dr. Ioannis Fitilis, Assistant Professor

– Dr. Ioannis Chatzakis, Associate Professor

– Dr. Antonios Konstantaras, Associate Professor

– Dr. Konstantinos Petridis, Associate Professor

– Dr. Ioannis Vardiambasis, Associate Professor

– Dr. Ioannis Kaliakatsos, Emeritus Professor

Reviewers

– Dr. Baklezos Anargyros, Researcher, School of Electrical & Computer Engineering, National Technical University of Athens

– Dr. Barbounakis Ioannis, Ass. Professor, Dept of Electronic Engineering, Hellenic Mediterranean University

– Dr. Fitilis Ioannis, Ass. Professor, Dept of Electronic Engineering, Hellenic Mediterranean University

– Dr. Hamacek Ales, Asc. Professor, Department of Technologies & Measurement, University of West Bohemia, Pilsen, Czech Republic

– Dr. Ioannidou Melina, Asc. Professor, Dept of Information & Electronic Engineering, International Hellenic University

– Dr. Kalderis Dimitrios, Ass. Professor, Dept of Electronic Engineering, Hellenic Mediterranean University

– Dr. Kaliakatsos Ioannis, Em. Professor, Dept of Electronic Engineering, Hellenic Mediterranean University

– Dr. Kokkinos Evangelos, Asc. Professor, Dept of Electronic Engineering, Hellenic Mediterranean University

– Dr. Konstantaras Antonios, Asc. Professor, Dept of Electronic Engineering, Hellenic Mediterranean University

– Dr. Kouridakis Stylianos, Lecturer, Dept of Electronic Engineering, Hellenic Mediterranean University

– Dr. Maravelakis Emmanuel, Asc. Professor, Dept. of Electronic Engineering, Hellenic Mediterranean University

– Dr. Maras Andreas, Em. Professor, Dept. of Informatics and Telecommunications, University of Peloponnese

– Dr. Petrakis Nikolaos, Lecturer, Dept. of Electronic Engineering, Hellenic Mediterranean University

– Dr. Sergaki Elefteria, Lab Teaching Staff, School of Electrical & Computer Engineering, Technical University of Crete

TABLE OF CONTENTS

THE IMPACT OF CORONA VIRUS TO HIGHER EDUCATION
(pp.1-5)
E. Lourakis, G. Triantafillou, M. Anastasakis, S. Kouridakis and K. Petridis

TRENDS IN QOE MODELING
(p.p.6-9)
G. Liodakis, P. Sergios and I.O. Vardiambasis

ICT REGULATION MEETS COVID-19 PANDEMIC: FOCUS ON WIRELESS NETWORKS
(pp.10-13)
G. Liodakis and I.O. Vardiambasis

SEISMIC BIG DATA MINING USING DEEP LEARNING NEURAL NETWORKS
(pp. 14-20)
A. Konstantaras and T. Frantzeskakis

SELF ORGANISED FUTURES MAPS NEURAL NETS AND HUBRIDS TO JORDAN ELMAN NETWORKS IN PORTFOLIO SELECTION
(pp. 21-25)
N. Loukeris, G. Polychronopoulos, A. Giovanis and E. Kokkinos

THE OVERVIEW OF MACHINE LEARNING APPLICATIONS FOR AGRICULTURE BASED ON HYPERSPECTRAL DATA
(pp. 26-29)
B. Ruszczak and Z. Kawalec

PAVING THE WAY FOR REALISTIC MODELING OF RIS-ENABLED COMMUNICATIONS
(pp. 30-33)
G. Liodakis and I.O. Vardiambasis

IMPLICATIONS ON ELF ELECTRIC FIELD DISTRIBUTION DUE TO SPACECRAFT CONDUCTIVE BOUNDARIES
(pp. 34-39)
A.T. Baklezos, I.O. Vardiambasis, T.N. Kapetanakis, N. Fragiadakis and C.D. Nikolopoulos

ESTIMATION OF RADIATED EMISSIONS OF SPACEWIRE LINK VIA HEURISTIC APPROACH FOR EMC ASSESSMENT
(pp. 40-44)
C.D. Nikolopoulos, A.T. Baklezos, T.N. Kapetanakis, N. Fragiadakis and I.O. Vardiambasis

WEARABLE ANTENNA DESIGN FOR BODY-CENTRIC COMMUNICATIONS
(pp. 45-56)
T.N. Kapetanakis, C.D. Nikolopoulos, K. Petridis and I.O. Vardiambasis

DEVELOPMENT OF ALL-TEXTILE ANTENNAS FOR THE ISM BAND
(pp. 57-61)
M. Pavec, T.N. Kapetanakis, C.D. Nikolopoulos, A.T. Baklezos, D. Moravcova, R. Soukup, T. Blecha, A. Hamacek, D. Stratakis, J. Chatzakis, M.P. Ioannidou and I.O. Vardiambasis

ABSORPTION ANALYSIS OF HIGH-BRIGHTNESS LIGHT-EMITTING DEVICES USING PHOTOCURRENT SPECTROSCOPY
(pp. 62-64)
A. Jaeger and H. Meinert

CUSTOM EFFICIENT SWITCHED-MODE LED POWER SUPPLY
(pp. 65-68)
V. Dumbrava, D. Pagodinas, A. Noreika and S. Kilius

MCR – WPT ANALYSIS AND DESIGN REVISION
(pp. 69-70)
N.A. Abu-Zaid

NUMERICAL STUDY OF NANOSCALE HEAT TRANSFER IN MOS TRANSISTOR SYSTEM
(pp. 71-72)
O. Zobiri and A. Atia

A TABLETOP PLASMA FOCUS NEUTRON SOURCE
(pp. 73-79)
I. Fitilis, A. Skoulakis, E.L. Clark, E. Kaselouris, M. Bakarezos, J. Chatzakis, V. Dimitriou, N.A. Papadogiannis and M. Tatarakis

ADVANCES IN PLASMA PARTICLE ACCELERATOR SUDIES VIA PIC SIMULATIONS ON THE HPC FACILITY – ARIS
(pp. 80-87)
I. Tazes, G. Andrianaki, A. Grigoriadis, G. Koundourakis, A. Skoulakis, E.L. Clark, E. Kaselouris, Y. Orphanos, J. Chatzakis, I. Fitilis, M. Bakarezos, V. Dimitriou, N.A. Papadogiannis and M. Tatarakis

NEW TRENDS IN PLASTIC RECYCLING FOR 3D PRINTING
(pp. 88-95)
N. Bolanakis, A. Driukas, D. Kalderis and E. Maravelakis

NEURAL NETWORK ESTIMATION OF THE ELECTROMAGNETIC FIELD SCATTERED BY A DIELECTRIC CIRCULAR CYLINDRICAL ROD IN CASE OF OBLIQUELY INCIDENT PLANE WAVES
(pp. 96-108)
T.N. Kapetanakis, A.T. Baklezos, C.D. Nikolopoulos, N. Petrakis, A. Konstantaras, M.P. Ioannidou and I.O. Vardiambasis.

THE IMPACT OF CORONA VIRUS TO HIGHER EDUCATION

Emmanouil Lourakis[1], George Triantafillou[2], Marinos Anastasakis[1], Stelios Kouridakis[1] and Konstantinos Petridis[1,2]

[1]Department of Electronic Engineering, Hellenic Mediterranean University
[2]International Relations Office, Hellenic Mediterranean University

1. INTRODUCTION

In January 2020, the World Health Organization (WHO) declared the coronavirus disease 2019 (COVID19) a Public Health Emergency of International Concern, and in March 2020 recognized COVID19 as a pandemic. The global Higher Education (H.E.) was impacted severely from the COVID-19 pandemic resulting in a significant transformation in the past six months [1]. Institutions have faced economic crises in the past, but the challenges posed by COVID-19 were unprecedented [2]. The pandemic spread fast across the globe and found H.E. Institutions mostly unprepared. Universities around the world were forced to cancel courses and lock down their facilities because of the growing coronavirus pandemic. The impact was felt on all H.E. stakeholders: students, researchers, academics, Institutions, Funding Agencies, and local societies. Students across the higher education sector have been forcefully impacted by the spread of COVID-19. According to United Nations for culture, science education, 58 million higher education students underwent an abrupt transition from face to face (f2f) learning to Online Learning during the COVID-19 pandemic [3]. E-learning [4] is one of the modern methods of our era, which in principle facilitates the transition from a 'teacher' oriented lecture to a 'student' oriented lecture. It is considered as a modern form of student-centered, interaction-oriented learning delivery that secures a learning environment from anywhere, at any time, with various sources of digital technology [5]. The learner becomes more able to discover, analyze, build, and acquire high-level learning & digital skills. However, the abrupt transition from the f2f to online learning was accompanied by a lot of challenges ranging from mobility restrictions, to social distancing from their peers, to changes in their study plans, to learning online models and to missing scholarship interviews [6]. Academics were also affected from the abrupt transition to online teaching, dealing with online exams, handling their research grants and mobility restrictions [9]. In the online learning environment, the teachers' role is not limited to providing knowledge; their role is much more comprehensive as they should also stimulate learning. Institutions were forced to close campuses and switch to online learning and digital tools with limited notice. Among the biggest challenges that HEIs faced included keeping students & staff safe and well informed about the pandemic, investing in online management tools, keeping open the research laboratories and maintaining research activities and dealing with missing funds due to low enrolment of international students to their programs (more than five million students in an annual base migrate for their studies) [11, 12]. Finally, as Higher Education Institutions are interconnected with the local society, they affect each other. As a result of the impact on Higher Education Institutions, local societies have experienced lower demand for student accommodation, lower consumption, increased demand for internet bandwidth [15] in parallel with the increased need to maintain a health system that can cope with the pandemic. Whereas the local societies can manage the demand of high bandwidth Internet, with the introduction of 5G Communication, the Higher Educational Institutions should inform and update the local societies about the developments regarding the fighting of pandemic. Through the effects of the situation in H.E. emerged the need for discovering the actual problems in H.E. stakeholders, along with methods of mitigating them. In the following sections there is a comprehensive presentation of the survey's findings and proposed actions for each category separately.

2. MATERIALS AND METHODS

The first axis of the survey was conducted through an online structured questionnaire [7] containing fifteen qualitative questions , in an attempt to decrypt the trends in the total of opinions between undergraduate and postgraduate students. Data was gathered with the use of Google forms in the time period from May 4th, 2020 to July 12th same year. The participants were 916 students with the sample margin of error to be ±3.16 in a confidence interval of 95%. The majority of the sample was undergraduate students with a percentage of 87.9% of the sample, with the rest 12.1% to be postgraduate students. The geographical origin of the students was mainly Europe with a percentage of 89.1% and the rest 10.9% outside of Europe. A second axis was devised via a series of three webinar held on April 27th, May 4th and May 7th on the challenges of Online Teaching & How to be a better Online Teacher [10]. More than 1,600 colleagues registered (85% of them had no prior experience in online teaching) in the webinar and more than 700 different colleagues followed it live. The speakers were experts in the fields of (a) teaching science and (b) online teaching and tried to answer the questions posed by the registered participants prior to the webinar. The total questions that the webinar addressed were 897. The third axis of the quest for problems caused by the pandemic in the institutions, was done through the literature. Since the campus life through close collaboration and proximity increased the risk of infection spread, they transformed their administration, educational and research operation functions[11,12]. Funding agencies (etc. Erasmus Project, HORIZON 2020) have experienced a negative impact on ongoing or planned activities [13,14] such as the need to manage the number of requests to extend the lifetime of awarded projects and keep alive the research activities (e.g. HORIZON 2020) and staff and student mobility (e.g. Erasmus).

3. RESULTS AND DISCUSSION

The students' perspective, as revealed through this survey, showed the following categories of barriers. The latter can be categorized into four categories (a) barriers between learner/learner; (b) lecturer / learner; (c) learner / technology; and (d) learner/thematic topic. The main results are listed below

- Technical problems: internet connection issues occurring during a (synchronous) lecture (barrier regarding the interface learner/technology)
- Social interactions: the perceived limited social interactions that a synchronous environment can afford or restrictions when collaborating online for a group assignment (26.6% of the participants – learner/learner). Moreover, 40% of the participants declared a much higher stress during the online learning & forthcoming exams compared to the period prior to COVID-19 (learner / lecturer & learner/ technology)
- Soft Skills required for online learning (23.8% declared lack of time management and motivation skills needed to handle their online learning pathway) (learner/learner)
- Administrative issues: problems such as textbooks not delivered on time, lack of Open Educational Sources or lack of announcements (learner /lecturer)
- Instructor issues: problems that undergraduates perceived as being caused by their lecturers, such as not using synchronous methods or adopting a fast pace in covering the curriculum (46.1% of the participants were not satisfied with the pace of lecturers and on the level of their understanding during the online teaching) (learner/lecturer)
- Subject related issues: the limitations of online environments in relation to certain subjects of study such as Mathematics, Music, Physics, Medicine and Engineering (learner/thematic topic)
- Technology related issues: limitations posed by the platform used in synchronous online learning, such as the number of participants permitted in an online lecture (23.9 **%** of the participants declared issues with the technology employed along online learning) – (learner/technology)

- Distractions: issues related to working from a home environment (54.1 % of the participants declared problems to be focused) (learner/learner)
- Access: not having access to online learning e.g. not owning a laptop or having an internet connection (learner/learner)
- e-class (Leaning Management Tool) issues: problems occurring during an online lecture such as accidents with open microphones and disruptions caused by background noise or undergraduates not following the norms of a class. (learner/technology)
- Technical skills: barriers related to undergraduates' unfamiliarity with technologies used in online learning (5.3 % of the participants) (learner/technology)

The students view regarding the online learning was not positive: 29.6% of the participants are negative towards online learning whereas the 55.6% voted for blended learning schemes.

From the teacher's perspective the survey collected and categorized the following issues:

- Assignments and Assessment methodologies; how to run secure online test & exams (29%)
- How to teach Online (the Pedagogy & soft skills required to follow) (21%)
- Technology to be employed and how to use it (18%)
- Emotional Engagement with the Learners (15%)
- How to run online laboratories (6%)
- Emotional Support for Teachers (3%)
- The Blended Mobility Schemes (2%)
- How to keep the staff & student mobilities live (2%)
- Other (4%)

Most of the above findings are in accordance with the relative literature not excluding other problems that this survey didn't discovered.

4. CONCLUSION

The covid19 pandemic and the followed lockdowns caught the H.E. stakeholders of guard. Students were affected the most since they are the recipients of knowledge higher education provides. Academic professors and university staff were also deeply affected by the abrupt change of the way classes were delivered in the lockdown period. The majority of the institutions were unprepared in terms of massive online course delivery and e-learning strategies.
Based on the results along with the challenges referenced in the literature the recommendations for curing these issues for each category of H.E. stakeholders, are as follows:

Table 1. Proposed actions concerning the student's challenges.

CHALLENGE	ACTION
Social Interaction	• Build the framework (train the students and teachers how to provide support) to emotional support our learners even in the case of blended learning era • Build support centers within the institutions that will provide tutoring and emotional support
Soft Skills for Online Learning How to Learn Online (How to handle Distractions, Time Management, Critical Thinking, Problem Solving, Stress Management)	Build a module (HMU already offers this module through its International relations Office Academy) on how to learn online Build a Soft Skills Module for the students (more focused on the online learning).
Instructor Issues	Training and Seminars how to teach online
Technology Related Issues	Tips of the most appropriate technology (and open source

	if this is possible) to be used along online teaching & learning Training in enhancing students digitalization literacy
Subject Related Issues	How to run virtual labs (construction, delivery) How to run online exams How to use and find OER

Table 2. Recommended actions for academics.

CHALLENGE	ACTION
How to build an online module	Tips on how to build interactive online modules (technology to be employed and list of things to follow)
Assignments and Assessment methodologies; how to run secure online test & exams	Seminars and Training Events on how to run these tasks online
Online Labs (mainly in the fields of engineering and health related courses)	How to build (e.g. software) Seminars & Training Examples – Samples
Emotional Engagement with the Learners	Pedagogy & Tips
Emotional Support of Teachers	Training and Seminars to Teachers
The Next Day: Blended Mobility & Flipped Classroom Approaches	Setting up the framework and provide training to teachers
How to use and find OER	A training seminar to teachers
How to use learning analytics to support your teachers & students	A training module and a seminar
Keeping the Staff and Students Mobility Alive (even after the COVID-19 era)	Strategies to keep staff and student mobilities alive

Table 3. Possible solutions for Institutions.

CHALLENGE	ACTION
Keep the staff & student mobilities alive	Design Strategies for cooperation within the consortium and beyond to enhance virtual and later on face to face mobilities
Use Digital technology to improve education	Generate pools of online joint online modules that will be offered by the consortium
How to keep research alive	Develop the strategies to keep research alive
Run Secure Online Exams	Development a Protocol to run secure online exams
Enhance the Digital Operation of Higher Education	Application of Blockchain Technology and Micro credentials in all the Universities Operations
Provide emotional and support to its stakeholders (students, academics, other personnel)	Create Online 24hours help-lines or Social Media Webpages to provide filtered information about the Pandemic and the actions should be followed

Table 4. Proposed actions concerning the local societies.

CHALLENGE	ACTION
High Bandwidth Internet	Communication with the local Governance Bodies for the sustainability and Maintaining of such network
Update the local society about the pandemic	Seminars and Online Talks regarding the most recent developments against the pandemic
Support the high unemployment	Through the Support centers and the Life Long learning

	Platforms the HEIs will provide online seminar courses to enhance the skills (soft and hard) of the local unemployment population in order to be more ready the next day

ACKNOWLEDGMENT

The authors would like to express appreciation for the support of Dr. Frangiskos Georgilas for the quantitatively analysis of our survey data.

REFERENCES

[1] The impact of the Coronavirus on the global higher education, https://www.qs.com, 2020
[2] B. Giridharan, Engaging with Students and Faculties online in the Era of the Corona Virus Pandemic: A Higher Education Perspective, Journal of Humanities and Social Sciences Research, Horizon J. Hum. & Soc. Sci. 2(S): 103 – 110, (2020)
[3]Organization, W.H. WHO Timeline – COVID-19. https//www.who.int/fr/news-room/detail/27-04-2020-who-timeline---covid-19
[4] How to Learn Online, a MOOC offered by EdX platform, https://www.edx.org/course/how-to-learn-online
[5] B. Khan, Learning Features in an open, flexible and distributed environment. AACE Journal 2005, 13(2), 137 - 153
[6]] A. Pragholapati, 'COVID-19 Impact on Students', 2020 - 10.35542/osf.io/895ed
[7] https://forms.gle/4egQ9qjzgpZyq7DPA
[8] Lin Y. Muilenburg and Zane L. Berge, Student barriers to online learning: A factor analytic study, Distance Education, Vol.26, No. 1, May 2005, pp. 29-48
[9] F. Darby, (2020), 'How to recover the joy of teaching after an online pivot', http://www.chronicle.com/article/How-to - Recover - the – Joy
[10] http://petridischania.hmu.gr/webinar/
[11] The impact of coronavirus on higher education, https://www.timeshighereducation.com/hub/keystone-academic-solutions/p/impact-coronavirus-higher-education
[12] The absent student – How covid-19 will change college, The Economist, August 8th – 14th 2020 issue
[13] Coronavirus impact, https://ec.europa.eu/programmes/erasmus-plus/resources/coronavirus-impact_en
[14] Coronavirus: European Commission takes special measures for Erasmus+ and Horizon 2020, https://www.eua.eu/news/475:coronavirus-european-commission-announces-special-measures-for-erasmus-and-horizon-2020.html
[15] Why the internet (probably) won't break during the coronavirus pandemic; https://www.vox.com/recode/2020/3/25/21188391/internet-surge-traffic-coronavirus-pandemic
[16] http://www.athenaeuropeanuniversity.eu/webinar-in-5g-communications-an-introduction-to-the-public/

TRENDS IN QoE MODELING

Liodakis, G.[1], Sergios, P.[1], and Vardiambasis, I.O.[1]

[1] Laboratory of Telecommunications & Electromagnetic Applications, Department of Electronic Engineering, Hellenic Mediterranean University
Chania, Crete, Greece
gsl@hmu.gr

1. INTRODUCTION

Since the introduction of the Quality of Experience (QoE) concept, all proposed definitions from academia and industry are user-centric and try to capture the user's subjectivity towards a specific network service (VoIP, web browsing, video streaming, etc.). According to the recent definition of the International Telecommunication Union (ITU), QoE is "the degree of delight or annoyance of the user of an application or service. It results from the fulfillment of his or her expectations with respect to the utility and/or enjoyment of the application or service in the light of the users' personality and current state", ITU (2016). Over the past few years, QoE has not only become a prominent issue for delivering network services, but also represents a paradigm shift from considering only the Quality of Service (QoS) guarantees.

As described in ITU (2016), QoE assessment is the process of measuring or estimating the QoE for a set of users of an application or service with a dedicated procedure. On the other hand, by QoE modeling, we understand the identification of the relevant parameters and the quantification of their influence on QoE. In essence, QoE modeling and assessment is one of the three key components for the QoE management of current and forthcoming networks for service delivery, Barakabitze et al. (2020). The other two components include the QoE monitoring & measurement and the QoE optimization & control components. More specifically, the monitoring and measurement of QoE-related information through the appropriate probes can provide inputs for QoE estimation models. Then, given the QoE model, through the dynamic control of relevant mechanisms (e.g. for communication resource allocation) and the proper optimization procedures (e.g. when and where to apply them), the target of QoE management for maximizing the users' QoE may be achieved.

The aim of this paper is not to provide an exhaustive review of research literature, but to point out the necessity for new QoE models and metrics that are focused on the network user as a human being. In such a way, not only a better understanding of the user experience will be provided but also an effective QoE management will be facilitated in light of the proliferation of challenging services, such as immersive services (augmented reality, virtual reality, etc.), over either wired or wireless networks. Thus, main well-established QoE modeling approaches and research directions for human-centered QoE modeling are presented in Sections 2 and 3, respectively. Finally, in Section 4, business-related implications of achieving more accurate QoE modeling will be detailed.

2. CURRENT QoE MODELING APPROACHES

The interaction between users and services is accompanied by the so called Influence Factors (IFs). An IF may potentially affect QoS metrics (e.g., in terms of packet loss or delay) and QoE metrics such as the typical Mean Opinion Score (MOS). Moreover, IFs can be summarized into 3 categories: system IFs (consisting of content-related, media-related, network-related and device-related factors), context IFs and human IFs, Zhao et al. (2017). In general, however, direct exploitation of the great majority of the IFs for QoE modeling purposes is not possible for many reasons.

The QoE modeling approaches may be classified according to various classification criteria, such as the type of application or service (e.g., VoIP and IPTV transmission) or the availability of reference information (e.g., full reference, reduced reference and no-reference models for video transmission). In this paper, we discriminate between mathematical and machine learning-based (ML) QoE models, if a whitebox or blackbox modeling approach is adopted, respectively. Both mathematical and ML-based QoE models aim to get a QoE value (or a QoE vector composed by different QoE components) through a mapping function f (see Figure 1), by the aid of a set of measurable input parameters (p_1, p_2, p_3, … , p_n). In general, the input parameters correspond to QoS metrics or values from a selected set of IFs appropriate to the QoE modeling application/service use case. The QoE value (or the QoE vector) should represent the QoE metric(s) of interest, such as the MOS score. Other QoE metrics beyond the MOS score and without its limitations may be found in Hossfeld et al. (2016).

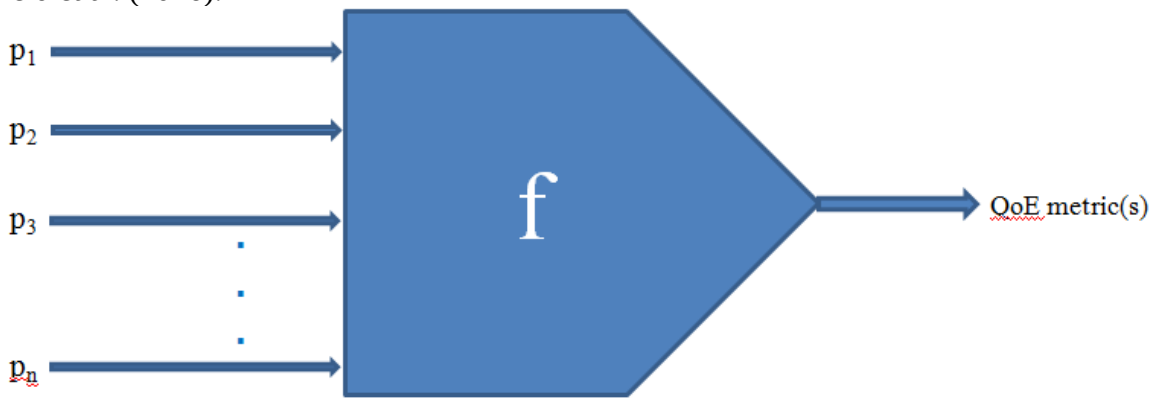

Figure 1. QoE modeling through mapping function f.

Mathematical QoE models rely on analytical expressions or statistical analysis in order to extract the users' QoE. Some input parameters (a specified set of QoS metrics, for example) as well as users' assessments are typically acquired in a laboratory testbed setting. In other cases, such as the extraction of parametric objective QoE models, part of the whole modeling process is carried out at the network planning stage (i.e., before the network deployment itself) whereas specific formulas take into account individual transmission impairments. Examples of mathematical implementation of the mapping function f include the QoE models for the two popular over-the-top (OTT) services of VoIP and Dynamic Adaptive Streaming over HHTP (DASH) video streaming, as provided by the simple analytical expressions of Eqs. [1] and [2], respectively:

$$QoE = f(PLR) = \alpha e^{-\beta PLR} + \gamma \qquad [1]$$

where $\alpha = 3.01$, $\beta = 4.473$, $\gamma = 1.065$, PLR stands for the Packet Loss Rate, and,

$$QoE = f(n,t,d) = 3.5e^{-4.5t/d - 5.7n/d} + 1.5 \qquad [2]$$

where n is the number of stalls, t is the total stall duration and d is the video duration.

ML-based QoE models, on the other hand, rely on algorithmic methods in order to implement the mapping function f. As such a mapping is highly complex, it is expected that ML techniques may cope with the nonlinear relationship between p_i (i.e., QoS metrics and quantified IFs) and QoE metrics. Various ML-based techniques, including Deep Learning (DL) techniques, have been recently utilized to demonstrate their appropriateness for QoE modeling, such as recurrent neural networks, convolutional neural networks, Bayesian Network or Gaussian process classifiers, etc. For instance, in Lopez-Martin et al. (2018), video QoE prediction is based on information directly extracted from the network packets using DL techniques. More specifically, a binary DL classifier

(good or bad quality) is used in order to detect common classes of anomalies (blur, color bleeding, black pixel, etc.) at the current time instant and predict them at the next immediate instant. Going beyond the QoS data concerning the individual under consideration application session, in Vasilev et al. (2018), the authors take into account network congestion (e.g., number of competing sessions, QoS measures on bottleneck), context information (e.g., type of device, content provider) and hidden variables (namely metrics that cannot be directly measured but can be still inferred from QoS metrics) for a DASH video streaming scenario. Their ML-based approach provides prediction for the following major relevant QoE metrics: the average video bitrate of the downloaded segments, the average video bitrate variation (thus, quantifying the quality changes over the different downloaded segments) and the re-buffering ratio (i.e., the stalling time over the duration of the video streaming session).

However, although both QoE modeling approaches have their merits, they present some drawbacks and challenges. In particular, mathematical models become impractical in cases of complex relationships between QoS and QoE metrics, and non-accurate due to simplification abstractions in order to get a closed form expression. On the other hand, ML-based models in a networking setting usually suffer from the unavailability, the granularity or the scalability of QoS data as well as their subsequent use as training data for various reasons. Thus, the prediction accuracy of ML-based models is highly affected, while their limitations due to computing requirements may lead to operational and performance trade-offs for real time QoE management.

3. FROM QoE TO HUMAN-CENTERED QoE MODELING

For both current as well as future innovative applications and services that are under development, there exists a trend towards regarding the user as a human being. Stated in another way, the user is not only a bandwidth consumer/prosumer with plain interactivity requirements, but also an entity that is characterized by his perceptual requirements with regard to the service he experiences. Thus, as it relates to QoE modeling, we should take into account various aspects of the human dimension, such as human behavior, human senses, body physiology and brain cognition issues.

Two instances that are quite representative of user behavior from a human-centered point of view, are analyzed in Hossfeld et al. (2019): the first instance is the user (im)patience resulting from waiting times and determines how long a user is willing to wait to receive a service after having initiated a service request, while the second one is the user (in)tolerance related to low service quality. More specifically, by the use of a mapping function f between the waiting time *t* and QoE, various use cases (web browsing, online authentication and adaptive video streaming services) and service scenarios (with shared or limited resources, etc.), are examined. The authors argue for the importance of incorporating such behavioral aspects that are often ignored in QoE modeling, with subsequent implications to resource allocation or service configuration decisions.

As it concerns the emerging immersive multimedia applications, a fully immersive experience for multisensory extended reality applications (i.e., across the whole spectrum from augmented to mixed to virtual reality applications) is hard to achieve, assess and model. Actually, all components of the QoE management loop require novel approaches and new challenges arise. These challenges include the following, Van Damme et al. (2020): no standardized methodologies exist for subjective testing of multimodal experiences; the time-critical characteristics of non-entertainment related immersive experiences make real-time end-user quality assessment essential; accurate and real-time prediction related to implementation issues of each individual multisensory application; proactive quality optimization and content enhancement algorithms (in case of late delivery) should be implemented in order to optimize user perception.

In light of the aforementioned discussion for a human-centered focus, the concept of Quality of Physical Experience (QoPE) has been recently coined in order to take into account physical factors originating from the human nature of the user along with current approaches. This new

QoPE concept should be further elaborated and quantitatively defined in conjunction with the well established QoS and QoE metrics for QoE modeling of each class of applications and services.

4. CONCLUSION

With the emergence of new services/applications and of new technologies and architectures for wired and wireless networking (next generation Passive Optical Networks (PONs), evolution of WiFi networks, 5G and future 6G cellular systems), it is envisioned that new well-defined QoE metrics and new QoE models are required. Thus, the practice of using the well-established MOS values for QoE modeling purposes, should be enhanced appropriately. A possible direction we are striving for may lie in incorporating the user's uncertainty in standard MOS values. More generally, both mathematical and ML-based QoE models should be more human-centered. In other words, new mapping functions towards a QoS-to-QoPE modeling paradigm should be introduced.

All in all, in line with the QoE modeling trends presented in this paper, it is expected that the overall QoE management will be provided in a way closer to user-human needs with implications for all the stakeholders of the service/application delivery chain. In essence, a transition from Service Level Agreements (SLAs) to Experience Level Agreements (ELAs) is occurring with implications to specific issues related to the stakeholders, as depicted in Table 1.

Table 1. Implications of QoE modeling and QoE management for stakeholders.

Service providers	OTT/Streaming providers, application developers, marketing teams, sales support
Fixed and Mobile network providers	network designers, network performance engineers, customer support
Equipment manufacturers	user devices, network devices
Regulatory authorities	SLAs/ELAs for QoS/QoE/QoPE
Users of applications & services	

5. REFERENCES

Barakabitze, A.A., N. Barman, A. Ahmad, S. Zadtootaghaj, L. Sun, M.G. Martini, and L. Atzori. 2020. QoE Management of Multimedia Streaming Services in Future Networks: A Tutorial and Survey. IEEE Communications Surveys & Tutorials, 22 (1): 526-565.

Hossfeld, T., P.E. Heegaard, M. Varela, and S. Moeller. 2016. QoE beyond the MOS: an in-depth look at QoE via better metrics and their relation to MOS. Quality and User Experience Journal, 1: Article 2.

Hossfeld, T., L. Atzori, P.E. Heegaard, L. Skorin-Kapov, and M. Varela. 2019. The interplay between QoE, user behavior and system blocking in QoE management. 22nd Conference on Innovation in Clouds, Internet and Networks and Workshops (ICIN): 112-117.

ITU Recommendation P.10/G.100. 2016. Vocabulary for performance and quality of service. Amendment 5: New definitions for inclusion.

Lopez-Martin, M., B. Carro, J. Lloret, S. Egea, and A. Sanchez-Esguevillas. 2018. Deep learning model for multimedia quality of experience prediction based on network flow packets. IEEE Communications Magazine, 9: 110-117.

Van Damme, S., M. Torres Vega, and F. De Turck. 2020. Human-centric quality management of immersive multimedia applications. 6th IEEE Conference on Network Softwarization: 57-64.

Vasilev, V., J. Leguay, S. Paris, L. Maggi, and M. Debbah. 2018. Predicting QoE factors with machine learning. IEEE International Conference on Communications: 1-6.

Zhao, T., Q. Liu, and C.W. Chen. 2017. QoE in video transmission: A user experience-driven strategy. IEEE Communications Surveys & Tutorials, 19 (1): 285-302.

ICT REGULATION MEETS COVID-19 PANDEMIC: FOCUS ON WIRELESS NETWORKS

Liodakis G. * and I.O. Vardiambasis

Laboratory of Telecommunications & Electromagnetic Applications, Department of Electronic Engineering, Hellenic Mediterranean University
Chania, Crete, Greece
* gsl@hmu.gr

1. INTRODUCTION

Since the recognition of COVID-19 as a pandemic by the World Health Organization (WHO), the vital role of network connectivity in supporting society and economy is unquestionable, Saeed (2020). However, the dramatic shift from face-to-face interactions to remote communication for various activities (teleworking, education, healthcare, entertainment, retail activities, etc.) was associated with a plethora of challenges for all parties involved in the Information and Communications Technologies (ICT) sector, Kshetri (2020). These challenges range from keeping both wired and wireless networks resilient in order to cope with the traffic surge to security aspects of ICT services to other indispensable regulatory measures.

In such a framework, the aim of this paper is to shed light on the impact of COVID-19 pandemic to regulatory initiatives related to wireless networks during the first phase of the pandemic (i.e., first semester of 2020). More specifically, in Section 2, an overview of the regulatory measures taken on a global scale is provided by means of the initiative carried out by the International Telecommunication Union (ITU). Then, in Sections 3 and 4, we present a representative and critical examination of measures related to two major regulatory issues, namely net neutrality and spectrum policy, respectively. Finally, Section 5 concludes the paper with some generic directions regarding the regulation of the wireless networking arena.

2. ICT REGULATION AND ITU

Network resilience, i.e. the ability of existing networks to support the needs of current users, was of paramount importance for both network operators and users just after the COVID-19 pandemic outbreak due to the dramatic need for networking. According to reports from network operators and other involved parties (e.g., CTIA (2020)), wired networks (and not wireless ones) were primarily affected by the network traffic increase. However, a remarkable traffic increase stressed cellular wireless networks, also. In particular, threats to wireless network resilience included the following:

- spatiotemporal traffic patterns, that changed overnight (much less mobility, shift of traffic from dense business areas to other areas, etc.),
- surging of traffic volumes (e.g. due to mobile data use increase from 4G and 5G vertical markets),
- radical change of wireless consumer behavior, as exemplified by the exploitation of WLAN from an increased number of household members.

Network resilience, however, should not be regarded only from a technical point of view. Regulation and policy issues play, also, an important role. Thus, the ITU set up the Global Network Resiliency Platform (ITU-GNRP), which is a place where policy makers, National Regulatory Authorities (NRAs), operators and service providers, as well as other interested stakeholders can share information, view what ICT-related policy and regulatory practices have been introduced around the world for combating COVID-19. More specifically, Figure 1 depicts the number of such measures and initiatives on a daily basis, as well as their aggregate number for the time period

under consideration. All these regulatory practices may be searched according to region/country, to organization type (regional and international organiazations, technical community and civil society, telecom/ICT operators and servive providers, telecom/ICT policy makers and regulators) as well as according to topic. In particular, the regulatory topics were classified as follows:

- accessibility,
- affordability,
- broadband availability,
- broadcasting,
- consumer protection,
- digital identity,
- emergency telecommunications,
- financial incentives,
- privacy,
- Quality of Service (QoS) & Quality of Experience (QoE),
- regulatory harmonization,
- regulatory innovation and experimentation,
- spectrum management,
- traffic management,
- universal service strategies.

As it is obvious from the above classification, the wide spectrum of regulatory practices itself is a clear evidence of the role of ICT regulation and policy has to play during the COVID-19 pandemic or in other similar situations.

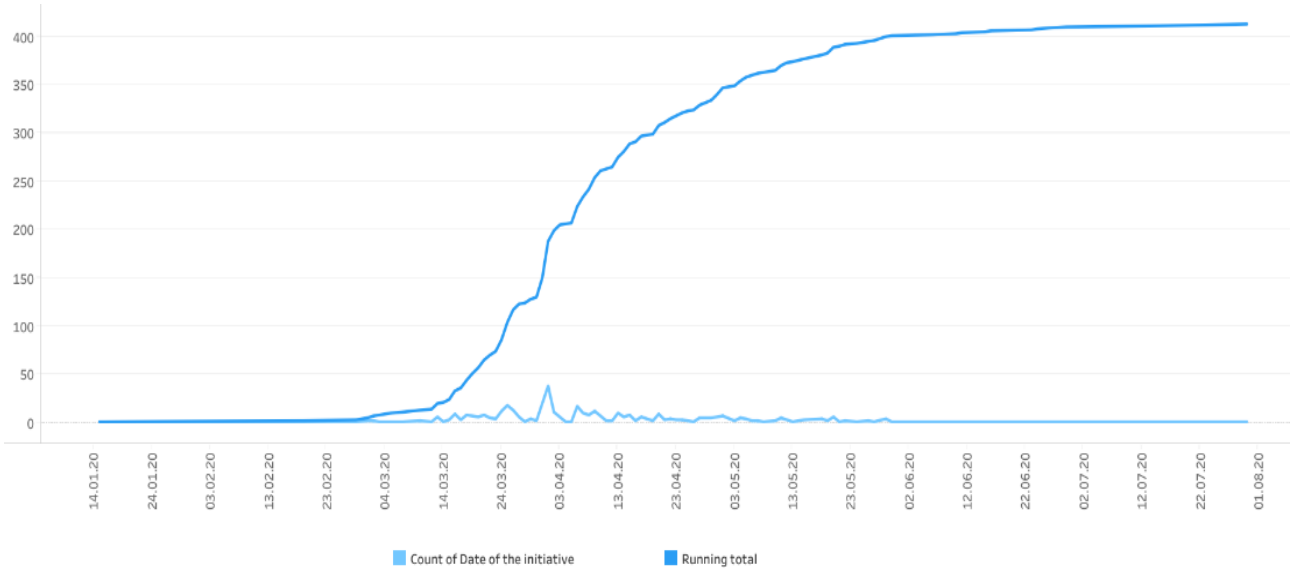

Figure 1. Evolution of worldwide regulatory measures and initiatives over time.

3. NET NEUTRALITY IN THE COVID-19 ERA

Generally speaking, network neutrality is the absence of discrimination and restrictions on the transmission of content. In particular, when net neutrality is regarded from a european perspective, it is about laying down measures concerning open internet access and retail charges for regulated intra-EU communications. More specifically, according to EU Regulation 2015/2120, operators are prohibited to apply exceptional traffic management measures to prevent impending network congestion and have to mitigate the effects of exceptional or temporary network congestion,

provided that equivalent categories of traffic are treated similarly. Moreover, different types of zero-rating practices are permissible by taking into account some criteria.

After the ascertainment that the increase in Internet traffic has not led to a general network congestion during the outbreak of COVID-19 pandemic, and taking into account the network neutrality framework in EU described above in a nutshell, the European Commission and the Body of European Regulators for Electronic Communications (BEREC) published a Joint Statement on 19-3-2020, European Commission and BEREC (2020). The central point of this statement is the full commitment to ensure an Open Internet in the EU. The latter had to be achieved by the operators, which are authorized to intervene only in exceptional or temporary circumstances through traffic management measures. In addition, a special reporting mechanism was set up in order to ensure regular monitoring of the Internet traffic situation in each Member State and swift response to capacity issues. Also, according to the aforementioned Joint Statement, telecom operators, content and application providers and users could contribute to the smooth functioning of the Internet. Thus, people were encouraged to make responsible use of the Internet with settings that reduce data consumption, while content and application providers were called to cooperate with telecom providers and consider the temporary adaptation of the throughput of video streaming.

In essence, compliance with net neutrality legislation issues during the early COVID-19 period was achieved either on a voluntary basis, or by publishing new guidelines/revisiting existing ones to better handle congested and overloaded (wireless) networks. Relevant indicative examples for wireless networks are as follows:

- YouTube, Netflix, as well as other content providers voluntarily committed to reduce their streaming bitrate (Netflix reduced its streaming speeds in Europe by 25%, while YouTube shifted to SD globally),
- users were advised to apply settings that reduce data consumption, including the use of WLANs (Wi-Fi technology),
- some wireless operators were shaping traffic in real time to meet the changing needs of their customers,
- authorization to prioritize access to content or applications from zero-rated websites related to health services, social welfare, government and public sector. In Greece, for example, the OTE Group mobile operator provided free access (zero-rating) to the digital platforms used for distance learning at schools by the Ministry of Education and Religious Affairs, along with free SMS for 3 months to the Greek Health Operations Centre of the Emergency Aid Centre (EKAV).

Table 1. Spectrum policy during COVID-19 pandemic.

Spectrum policy issue	Short-term regulatory measure	Implications
Flexible spectrum use	Temporary grant access to additional spectrum of either vacant spectrum or unused spectrum of existing licenses	Boost of network capacity and improved QoS
Deployment of new 4G/5G FWA networks in line with policy objectives of universal coverage	Promotion of relevant investments by regulatory authorities	Support of communication needs during the COVID-19 pandemic
Allocation of spectrum for WLANs	Unlicensed use of the 6 GHz band (USA)	Better QoS & offloading of cellular traffic to WiFi 6E networks
Spectrum auctions	Postponements (or cancels)	Delay for 4G network expansions and new 5G network roll-outs
Public consultations for planned tenders for frequencies' allocation	Extensions of deadlines	Delay for the subsequent spectrum auctions

4. SPECTRUM POLICY IN THE COVID-19 ERA

A number of measures and initiatives were undertaken by both NRAs and mobile operators in order to boost the capacity of wireless networks and guarantee the associated QoS requirements. For example, the action of the national USA operators (T-Mobile, Verizon, AT&T) to loan spectrum licenses that were not being used by their existing license holders for 60 days beginning in mid-March 2020, is a paradigm of short-term flexible spectrum use measures. In other cases, the NRA-initiated speed-up of 4G/5G Fixed Wireless Access (FWA) deployments in many countries (Italy, Egypt, Thailand, etc.) proved to be very useful to support the immediate work-from-home and study-from-home user demands during the first phase of the COVID-19 pandemic. Furthermore, the FCC's decision (April 2020) for WiFi 6E (i.e., to open up the 6 GHz frequency band for unlicensed use by WiFi 6 technology) will lead to faster connectivity speeds and improved capacity when compared to both 2.4 GHz and 5 GHz WiFi. It should be mentioned that such an approach for WiFi 6E is already under examination by EU and other NRAs in the light of traffic demand due to COVID-19.

On the other hand, however, other spectrum policy practices were negatively affected by COVID-19. For instance, spectrum auctions for 4G network expansions and new 5G network roll-outs were postponed or cancelled. As a whole, in Table 1, a representative set of spectrum policy issues along with their short-term regulatory measures and associated implications, is depicted.

5. CONCLUSION

COVID-19 has demonstrated the critical role that communication service providers play in general (and mobile operators, in particular) for individuals, businesses and the society as a whole. Resilience of wireless networks was a priority for all stakeholders during the early period of COVID-19, while the net neutrality and spectrum policy issues addressed by this paper were well managed on a short term basis.

However, ICT regulation authorities and policy makers should introduce additional medium and long term regulatory measures concerning 5G network rollouts and wider 5G adoption. More specifically, NRAs should (i) facilitate sharing agreements with fiber network providers in order to deploy denser 5G networks, and (ii) intervene to rights-of-way issues in order to facilitate access to municipal poles and other utilities' infrastructure for a faster 5G network deployment. All in all, the ICT regulatory framework towards a sustainable 5G ecosystem needs to be adapted to the new normal.

6. REFERENCES

CTIA report. 2020. How wireless kept American connected during COVID-19.

European Commission and BEREC. 2020. Joint Statement on coping with the increased demand for network connectivity due to the Covid-19 pandemic.

Kshetri N. 2020. COVID-19 meets Big Tech. IEEE Computer, 53, 08:10-13.

Saeed N., A. Bader, T.Y. Al-Naffouri, and M.S. Alouini. 2020. arXiv:2005.06637v2.

SEISMIC BIG DATA MINING USING DEEP LEARNING NEURAL NETWORKS

Konstantaras, A.[1] and Frantzeskakis, T.[1]

Department of Electronic Engineering, Hellenic Mediterranean University,
Romanou 3, Chania, 73133, Greece
akonstantaras@hmu.gr (corresponding author)

ABSTRACT

Seismic activity along Greek territory, has been a very interesting subject among dominant topics of the Greek science community due to the critical stead the Greek surface extent in reference to its tectonic position. This for the most part is placed on the Eurasian plate, with Crete's location in close proximity to both the Eurasian and African plates, while both of those plates share common points with the Arabian plate, creating a three-plate convergence. This convergence is also in close proximity to Cyprus geographical location, further creating interesting seismically unpredictable high activity to the surrounding regions, including the Greek seismic belt. Throughout this paper, an attempt is made to extract Greek related geological and seismological findings through careful observation to the already existing seismological dataset, via Deep Learning Neural Network model pattern extraction procedures and interactive data visualization. The tools that have been used, revolve around the Anaconda scientific distribution, which contains all the necessary means to conduct data analysis procedures and additionally, it's widely available with free versions, lowering the education and financial required threshold for everyone to easily conduct data mining on both individual and grouped, available datasets and extract correlation features between time patterns and magnitudes of subsequent seismic events for a particular area.

1. INTRODUCTION

With the speed of internet in a state where direct measurements are collected into central databases through high precision sensors, many organizations have real time data available in a relatable website with the license to further distribute those indications for data analysis purposes. Such organization is the Institute of Geodynamics which is the subject of National Observatory of Athens that catalogues real time seismicity. The Institute of Geodynamics provides highly accurate seismic data through its 45 telemetric, digital seismic stations, equipped with broadband 3D component seismometers. The data extracted are carefully revised, archived and are further available in their website in many chronologically arranged catalogues, in the form of plain text, where each group of data is simply separated by spacing. For the research needs of this attempt in analyzing seismological data, the full catalogue will be automatically downloaded, extracted, organized and used in order to transform the data to a suiting format that satisfy the assignment goals. The dataset consists of more than 290900 entries, starting from year 1964 and going as far as 2020, with magnitude sizes between MS 0.1 and MS 7.0 in the Richter scale, seismic depths between 0 km and 244 km and precise timestamp (Konstantaras 2016) in seconds, minutes, hours, day and month and year of each earthquake's occurrence, as well as the geographic position of latitude and longitude coordinates (GI-NOA, 2020).

While the available dataset contains a large sum of earthquake occurrences, for this assignment there will be a data filtering, where only earthquakes of magnitude Ms>=4.0, will be utilized (Konstantaras, 2020). Before any kind of effect can take place in accordance to the values that have been kept, those values must initially be observed, so that the interested individual can roughly understand the shape that the data assumes, preferably in the 3D space. The user must firstly observe the scope of the data that are studied, and how these data are distributed through the field of interest, i.e. the Greek vicinity, make initial deductions as to where the most intense seismic

activity is presented and associate visually observations with additional geographical data, like underground fault mappings or the in depth location of the recorded seismic phenomena, which further depend on the movement and position of the global tectonic plates (Konstantaras, 2006,2007). The data by themselves hold enough information for them to be plotted in the three axis of the cartesian level, with latitude being projected to the Y-axis, longitude being projected to the X-axis and depth in kilometers being projected to the Z vertical axes (Figure 1).

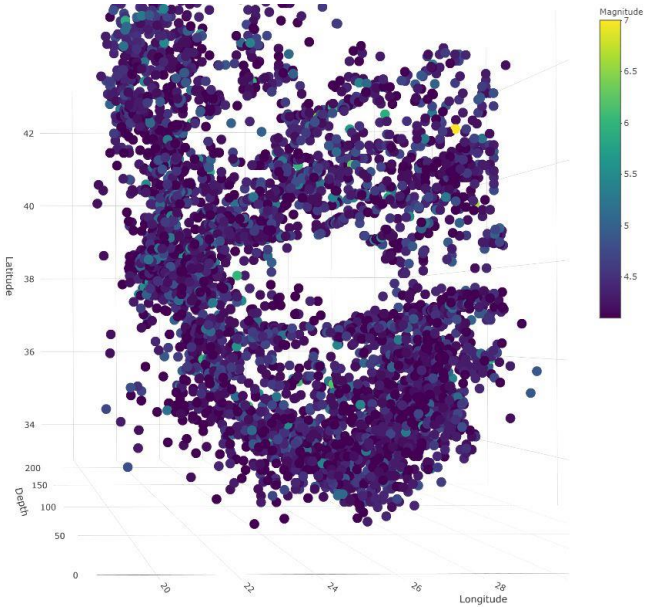

Figure 1. Seismic data of magnitude Ms >= 4.0 plotted with respect to Latitude (North), Longitude (East) and Depth in kilometers. The color-map indicates the magnitude of each seismic event.

Additionally, while the data are being projected (Maravelakis et al., 2012, 2014; Axaridou et al., 2014) to the 3D level (Figure 2), they can be simultaneously color coded according to a fourth value as shown above. It is recommended this value to be either the magnitude, so the user can see the seismic intensity on a seismic point, or the year of occurrence so the user can see how old the earthquakes are in a point and also observe the yearly seismic activity of a certain area, and make further conclusions concerning something that was idle before activated, like a rift, an underground faults, an underwater crack or even a volcano. For reference, a black and white map of Greece was used while seismic data were projected on the map, so the user can pinpoint the earthquake locations of interest and measure seismic activity via observations.

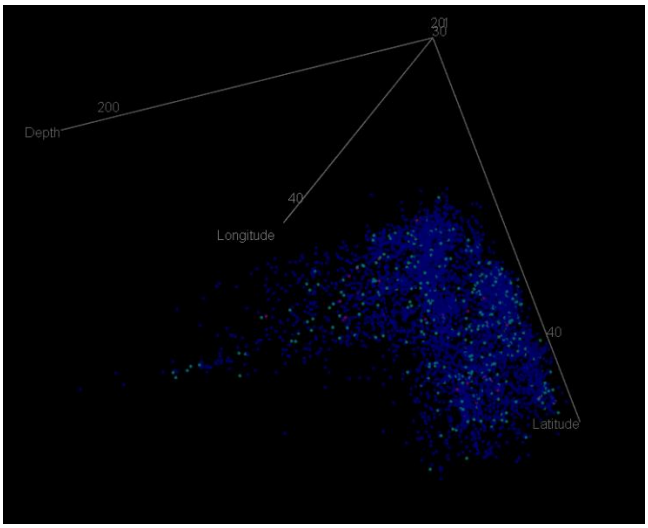

Figure 2. 3D display of seismic data magnitude of Ms>=4.0. On the 3D-viewer (Maravelakis et al., 2014) the figure is interactive and can be rotated or zoomed as the user sees fit.

Following these observations, the user then deploys deep learning neural network for pattern extraction procedure. For this, the user can rely on the scientific distribution of Anaconda, as it contains the whole arsenal required to conduct such designs. Various institutions and companies have developed their own deep learning neural network tools, in order to conduct machine learning tasks, and most of them provide those tools for free, leading to the development of specific versions of those tools for most of the programming languages. For this assignment, some of these tools are utilized and as the base of this assignment is to be object oriented, programming tools that allow breaking the problem into smaller ones were selected. This approach makes it easier to conceptualize behind the procedure throughout the end to end development of an easily maintainable machine learning project with the purpose of predicting magnitude values in a given time and area.

2. METHODOLOGY AND RESULTS

The neural network idea, as many other ideas, initially was inspired by existing phenomena in nature, like the brain structure or the eyes of the fly. It all revolves around the perceptron or neuron, a node that receives a number of inputs, each of them multiplied by a weight of significance, and finally added to a total sum, which sum is then passed through an activation function and produces an output. An activation function decides if a node should activate or not (Winter, 2016). There are many activation functions n and depending on the application, the appropriate function is used. The inputs of the system consist of external information to be passed to the system. Each input connects to an input neuron and those neurons are connected to the output neurons. A group of neurons is called neural network and it contains an input layer and an output layer with optional in between layers called hidden layers.

The capabilities of a neural network change depending on the hidden layers count. If the system utilizes no hidden layers, it is only capable to represent linear separable deductions. With one hidden layer, the neural network can approximate any function that contains a continuous mapping from one finite space to another. With two hidden layers, the system can represent an arbitrary decision boundary to arbitrary accuracy with rational activation functions and can approximate any smooth mapping to any accuracy. With more than two layers, the system can learn complex representations (Heaton Research, 2017). Each artificial neural network contains features and labels. The features are the data fed into the network for it to be trained. The labels are the values that the network is trained upon. Those features and labeled values can be of many different types, but the most usual types used by artificial neural networks are categorical data and numerical data (Konstantaras, 2008, 2012, 2013).

Categorical data represent a decision between other available choices, like the gender of a species, the month of the year or the handwritten digit a system recognizes and categorizes it between zero and nine. The problems that have to do with categorical data are called classification problems and usually consist of more than two neurons in the output layer, meaning that the neural network structure has to predict between some cases and operate a classification based on the input data. If the problem is to predict a numeric value, it is called regression problem. The most common example of a regression problem is one where the user predicts the value of an estate based on the number of its rooms and the square feet of the plot.

This assignment makes a prediction of the seismic magnitude, given values for year, month, day, latitude, longitude and depth, so it is categorized as a regression problem. The values used to predict the magnitude have large differences in size, and because every neuron takes the sum of these values multiplied by their individual weights and then passes this sum to an activation function, those values must be brought to similar in size quantities before training. There are many ways to make all the values alike, this assignment utilizes the standard score or z-score method and is expressed by the function $Zi = (Xi – \mu) / \sigma$ where Zi is the processed value, Xi is the real value, μ is the average value and σ is the standard deviation (AP Statistics, 2020). Every column of data has its own set of μ and σ which are used to reverse this procedure after the predictions have been

made.

Once data have been transformed to similar values, the training can be initiated. The training methods that are used , utilize the use of Tensorflow and Keras libraries. Tensorflow is a symbolic math library that can also be used for machine learning applications, such as neural networks. It was developed by the Google Brain team for internal Google use and it was released under the Apache License 2.0 on November 9, 2015 (Tensorflow, 2020; AP Statistics, 2020). Keras is an open-source neural-network library written in Python. It is capable of running on top of TensorFlow, Microsoft Cognitive Toolkit, R, Theano, or PlaidML. Designed to enable fast experimentation with deep neural networks, it focuses on being user-friendly, modular, and extensible. It was developed as part of the research effort of project ONEIROS (Open-ended Neuro-Electronic Intelligent Robot Operating System) (Keras, 2020), and its primary author and maintainer is François Chollet, a Google engineer (Chollet, 2016). Python has distributions of these libraries that the user can download and install, in order to develop neural network implementations and acquire additional familiarity with the machine learning concepts. After the successful installation of the libraries for the specific programming system, for this assignment the programming system used is Python language of the Anaconda distribution, training can be initiated. The procedure is simple and easy to follow. First, the data are inserted either directly from the internet or from an external data file. Depending on the shape of the data, some changes may need to be made on the data. Those changes are made according to the documentation of the data handling library and for this assignment this library is Pandas. Pandas can handle text data, separated by spaces and new lines, comma separated values, Microsoft Excel files, and convert them into data frames, a type of object in Python. It is again highly recommended that the user studies the documentation of every library that is used, as he can both avoid mistakes and save on valuable time trying to devise something that the library already addresses, like separating the data, decoding it or deleting specific rows. The data are then processed to similar size values before separating which part will form the training dataset. As described in the Keras documentation, the user can determine what type of model wants to design and choose the appropriate model type, what activation function, what optimizer, all of which are fully documented in the official Keras website.

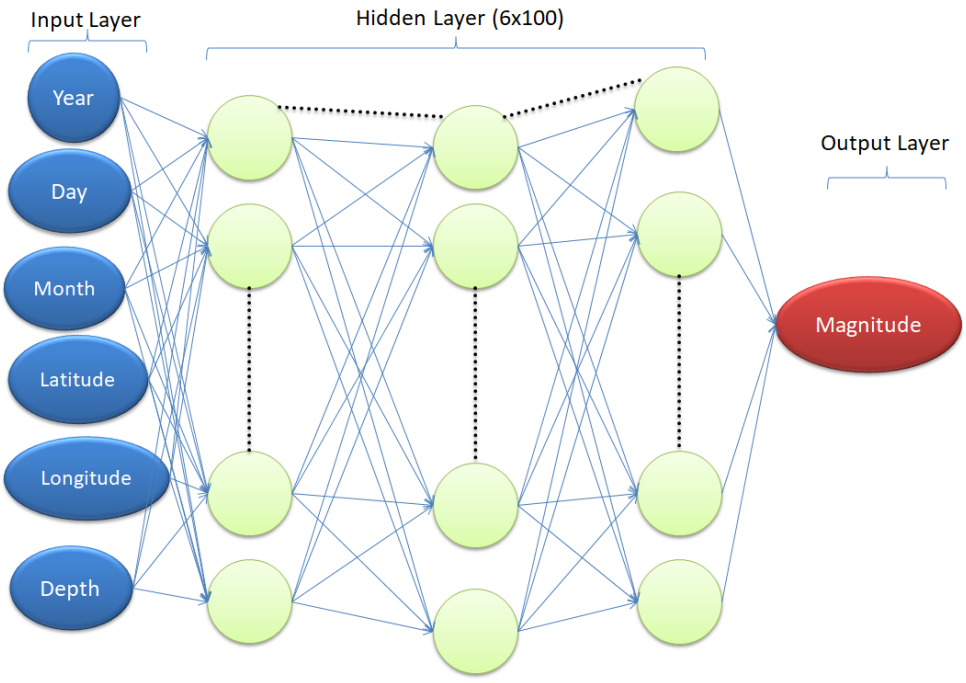

Figure 3. The Artificial Deep Learning Neural Network designed and trained for this assignment.

This assignment uses the sequential model type with six neurons in its input layer, six hidden layers with one hundred neurons each and one output layer (Figure 3). Every neuron of the system is activated by the rectified linear unit, which chooses the max between: a) the sum of the values multiplied by their weights and b) zero. The output layer consists of one neuron, as it should be the case in every regression problem, because the deep learning neural network modifies its weights during the training process according to the output value.

The compilation process must have some parameters configured by the user, like the loss method that will be used, the optimizer type and the metrics. The loss method is a string parameter in the compile function and it represents a scalar value that the network attempts to minimize during the training of the model. It demonstrates how close are the predicted values to the true values. Keras provides many loss methods like mean squared error, mean absolute error, categorical cross entropy and many more, available in the keras losses documentation. The second argument for the compilation function is the optimizer. An optimizer is a parameter that defines learning sizes such as learning rate, momentum, decay of learning rate and more, depending on the optimizer. There are many different and ready to use optimizers that Keras provides, like stochastic gradient descent, adam, adamax and more, but the user can still manage the optimizers parameters if deemed necessary.

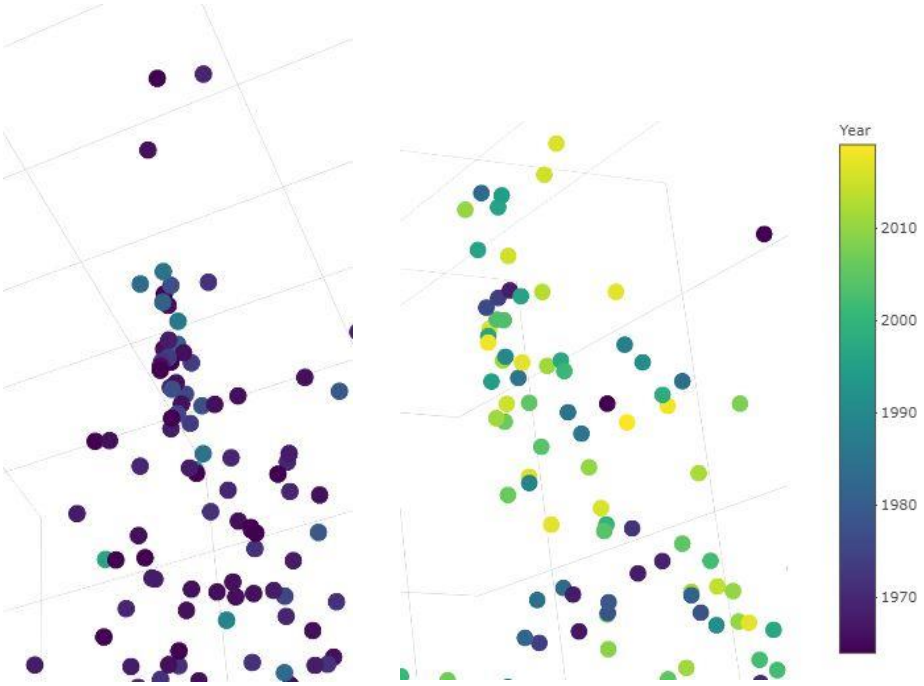

(a) **(b)**

Figure 4. Subplot (a) shows seismic activity of Ms>=4.0 earthquakes. Subplot (b) shows the predicted activity by the deep learning neural network. The similarity of the pattern structure at different time eras is an indication of an underlying mined by the deep learning neural network pattern.

The elements of the functions for this assignment were chosen based on trial and error , so the loss parameter used is the mean squared error and the optimizer is adam. After compilation, the training can be initiated by calling the fit method on the model. The fit method's arguments are the input data or features, the data the network is trained upon or labels, a batch size, an epoch size and a validation dataset. The validation dataset is a slice of the original dataset, preferably thirty percent of the total dataset, and it is not used during training, instead it is used after training to validate how well the model predicted unknown data. The training results, shown in Figure 4, pass to a history type variable that keeps a history of the models attributes like training loss, metric values at successive epochs, validation loss values and validation metrics values. Finally, the trained model can be saved to an external file for later use, and this assignment ends with custom user data in a

form of an Excel file, being predicted using the model created. It is very important that the mean and standard deviation numbers of the predicted value, are maintained so that the Z-Score method can be reversed for real values to be extracted.

3. DISCUSSION AND CONCLUSIONS

Earthquake prediction is a globally vital mater for the coexistence of human infrastructure and the sub terrain activity that manifests with seemingly unpredictable patterns. With the help of the modern ever evolving technology, vast amount of information can be received and later be processed for conclusion and the creation of advisory character metrics, according to the seismic activity that has been observed in various forms. Seismic areas that present activity in the last decade, like the area between the islands of Syrna and Kandelioyssa of Nissiros that presents multiple earthquakes following a vertical pattern, (36,7 Latitude North, 27,14 Longitude East) can be observed for further pattern recognition, with the aid of this assignments tool that was developed. The general purpose of this tool is predicting possible seismic activity and could be used along with other verification for a more spherical approach to the seismic activity in areas of interest. Training data of interesting, areas can be fed into the network for training and more precise predictions concerning this specific area. Certain areas may possibly present continuous seismic patterns such as the aforementioned as shown by the results in the last figure. Future work shall focus on main earthquakes only, grouped into ranges out seismic magnitudes, requesting by the deep learning neural network to depict the seismic range of the next upcoming earthquake for a particular seismic zone.

4. REFERENCES

AP Statistics, 2020. Standard Normal Distribution. https://stattrek.com/probability-distributions/standard-normal.aspx (accessed on 01 October 2020).

Axaridou, A., I. Chrysakis, C. Georgis, M. Theodoridou, M. Doerr, A. Konstantaras, E. Maravelakis, 2014. 3DSYSTEK: Recording and exploiting the production workflow of 3D-models in cultural heritage. In Proceedings of the 5th International Conference on Information, Intelligence, Systems & Applications (IISA2014), Chania, Greece, 7–9 July 2014: 51–56.

Chollet, F., 2017. Xception: Deep Learning with Depthwise Separable Convolutions. IEEE Conference on Computer Vision and Pattern Recognition (CVPR), Honolulu, HI, 2017: 1800-1807.

GI-NOA: Geodynamics Institute-National Observatory of Athens. Available online: http:// www.gein.noa.gr/en (accessed on 01 October 2020).

Heaton Research, 2017. The Number of Hidden Layers. https:// www.heatonresearch.com/2017/06/01/hidden-layers.html (accessed on 01 October 2020).

Keras, 2020. Keras, Simple, Flexible, Powerful. https://keras.io (accessed on 01 October 2020).

Konstantaras, A., M.R. Varley, F. Vallianatos, G. Collins, P. Holifield, 2006. Neuro-fuzzy prediction-based adaptive filtering applied to severely distorted magnetic field recordings. IEEE Geosci. Remote Sens. Lett., 3: 439–441.

Konstantaras, A.; M.R. Varley, F. Vallianatos, J.P. Makris, G. Collins, P. Holifield, 2007. Detection of weak seismo-electric signals upon the recordings of the electrotelluric field by means of neuro-fuzzy technology. IEEE Geosci. Remote Sens. Lett. 4: 161–165.

Konstantaras, A., F. Vallianatos, M.R. Varley, J.P. Makris, 2008. Soft-computing modelling of seismicity in the southern Hellenic Arc. IEEE Geosci. Remote Sens. Lett., 5: 323–327.

Konstantaras, A., E. Katsifarakis, E. Maravelakis, E. Skounakis, E. Kokkinos, E. Karapidakis, 2012. Intelligent spatial-clustering of seismicity in the vicinity of the Hellenic seismic arc. Earth Sci. Res., 1: 1–10.

Konstantaras, A., 2013. Classification of distinct seismic regions and regional temporal modelling of seismicity in the vicinity of the Hellenic seismic arc. IEEE J. Sel. Top. Appl. Earth Obs. Remote Sens., 6: 1857–1863.

Konstantaras, A., 2016. Expert knowledge-based algorithm for the dynamic discrimination of interactive natural clusters. Earth Science Informatics, 9: 95–100.

Konstantaras, A., 2020. Deep Learning and Parallel Processing Spatio-Temporal Clustering Unveil New Ionian Distinct Seismic Zone. Informatics, 7 (4), 39: 1-10, doi: https://doi.org/10.3390/informatics7040039.

Maravelakis, E., N. Bilalis, I. Mantzorou, A. Konstantaras, A. Antoniadis, 2012. 3D modelling of the oldest olive tree of the world. International Journal of Computational Engineering Research, 2 (2): 340-347.

Maravelakis, E., A. Konstantaras, K. Kabassi, I. Chrysakis, C. Georgis, A. Axaridou, 2014. 3DSYSTEK webbased point cloud viewer. In Proceedings of the 5th International Conference on Information, Intelligence, Systems & Applications (IISA 2014), Chania, Greece, 7–9 July 2014: 262-266.

Tensorflow, 2020. An end-to-end open source machine learning platform. https://www.tensorflow.org (accessed on 01 October 2020).

Winter, A.I., 2016. A Concise History of Neural Networks. https://towardsdatascience.com/a-concise-history-of-neural-networks-2070655d3fec (accessed on 01 October 2020).

SELF ORGANISED FUTURES MAPS NEURAL NETS AND HUBRIDS TO JORDAN ELMAN NETWORKS IN PORTFOLIO SELECTION

N. Loukeris[1,2], G. Polychronopoulos[2], A. Giovanis[2], E. Kokkinos[3]

[1]Athens University of Economics and Business, Dept. Accounting & Finance, Patision 76, Athens, Greece
[2]University of West Attica, Dept. Business Administration, Ralli 252, Athens, Greece
[3]Hellenic Mediterranean University, Dept. Electronic Engineers, Romanou 3, Chania, Greece
*Corresponding Author: nloukeris@uom.edu.gr,

1. INTRODUCTION

The optimization of portfolio selection follows a two phase process: firstly the evaluated portfolios form the feasible set, secondly the efficient portfolios are ranked in a utility function minimizing the risk –in terms of variance Markowitz (1952), further expanded to more detailed aspects of risk, Loukeris and Eleftheriadis (2017). This research examines the first step of the problem that supports the solution on the second step. We investigate extensively the models, of neural or neuro-genetic hybrids: 20 the Jordan Elmans in 10 neural nets and 10 hybrid neuro-genetic JEs, 20 different Self Organized Feature Maps nets in 10 neural nets and 10 hybrid neuro-genetic SOFM models as well, to detect the efficiency of the systems concluding to the optimal classifier of portfolio selection.

2. SELF ORGANIZED FEATURES MAPS

The Self Organized Features Maps-SOFM neural network, Kohonen (1982), optimises clustering, and data examination problems. The SOFM learning is unsupervised creating a 2-dimensional map, the input surface is discretised on training data minimizing the dimensionality. The SOFMs implement competitive learning, in contrast to the other neural nets. The 16 fundamental indices we elaborate have an unknown impact in SOFMs, thus we incorporate Genetic Algorithms-GA, Holland (1975/1992), to define it. The models are trained under numerous repetitions to conclude in the level of lowest error. The GAs are used in different hybrids both for the JEs and SOFMs of the inputs layer only, in different topologies. The Batch learning adjusts the weights of hybrid SOFM.

3. PARTIALLY RECURRENT NEURAL NETWORKS

The Partially Recurrent Networks PRN), Loukeris et al (2015), Loukeris et al. (2014a,b) are MLPs where a few recurrent connections are introduced. The inputs of PRN has 2 different forms of neurons: inputs neurons that receive external signals, and the neurons of state that remember past actions and take output values from one of the layers delayed by one step. The Partial Recurrent Networks are i) the Jordan network, ii) the Elman network and iii) the Multi –Step Recurrent network.

4. THE JORDAN NETWORK

In the Jordan neural networks, Jordan (1986a, 1986), the context neurons receive a copy from the output neurons forming themselves, and many of them become the outputs. The recurrent connections from the output layer to the context neurons have an associated parameter of constant value: m ϵ (0, 1).

5. THE ELMAN NETWORK

In the Elman networks, Elman (1990), the context neurons receive a copy of the networks' hidden neurons, that don't need to associate any parameter. Thus the number of the context neurons is identical to the number of hidden neurons into the network. The remaining activations are calculated similarly as in a Multi Layer Perceptron, considering the sequence of external inputs and context neurons as the vector input to the network.

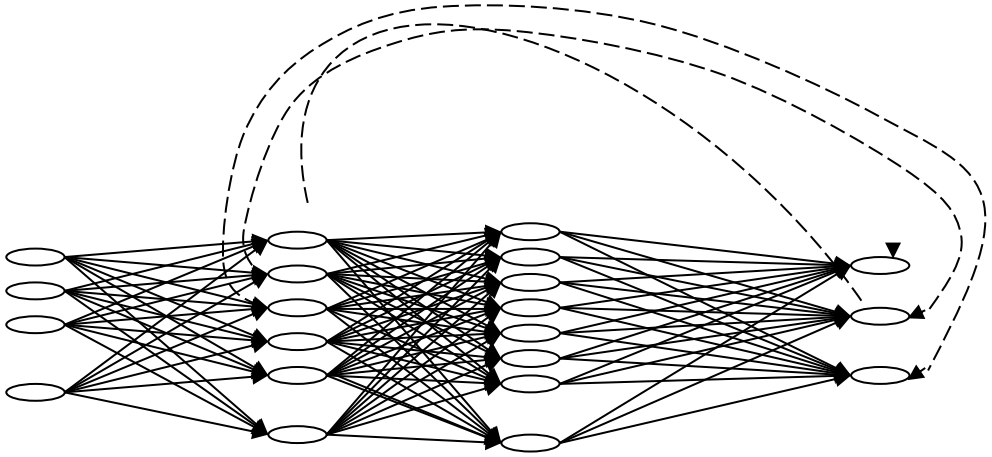

Figure 1. The Elman Network of multiple layers

6. THE MULTI-STEP RECURRENT NETWORK

In the Multi-Step recurrent network, Galvan and Isasi (2001), the feedback connections are directed from the output neuron to input layer. The context neurons memorise previous outputs of the network. The number of input and context neurons is replaced in every sampling time by other neurons in cases of prediction.

7. THE JORDAN ELMAN NETWORKS

The Jordan and Elman networks Loukeris et al (2015), Loukeris et al. (2014a,b) extend the MLP implementing neurons that remember past activity, the context units. These context units offer to the JE models the ability of extracting temporal information from the data. There are available 4 essential topologies that alter by the layers that feed the context units. The topology I provides the context units with the inputs, and builds a robust past substratum of the input by its memory traces.
The context neuron memorizes the past of its inputs in the recency gradient, that uses oblivion in an exponential decay. Thus the memory of recent data is better than the memory of those in a more distant past. The neurons of the context unit manages the forgetting factor in the Time constant that takes values among 0 and 1. In case of the 0 only the present time of data considered indicating that there is no self-recurrent connection, whilst for a value of 1 all of the past is factored in. The closer the value is to 1, the longer the memory depth and the slower the forgetting factor.
The number of neurons in the context layer is defined by the number of neurons in the layer that feeds the context layer (i.e., the network will assign one context unit per input connection). As with the other neural models, the number of Hidden Layers must be defined. The configuration of all the Jordan Elman nets in the current research is selected to feed the context units with the input samples, providing an integrated past of the input. The context unit remembers the past of its inputs using a recency gradient, forgetting the past with an exponential decay, and controls the forgetting factor through the Time constant that here is selected to be the IntegratorAxon function of 0.8 s time –of a longer memory depth and a slower forgetting factor. There were standard 4 neurons per hidden layer using as the transfer function the TanhAxon, the learning rule was the Momentum function, on a value of 0.7 as a momentum and changing step size per hidden layer in a scale of 0.1.

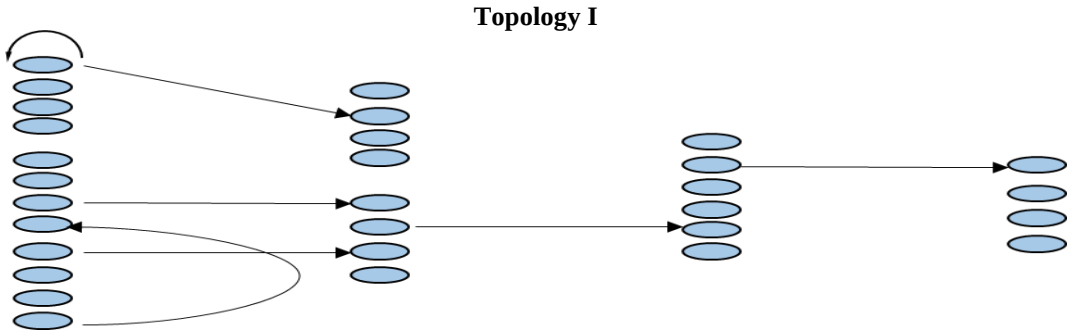

Figure 2. The processing in Jordan and Elman networks throughout topology I

7.1 The Genetic Algorithms in the Jordan-Elman Hybrids

The significance on each one of the 16 financial inputs in all the Jordan Elman networks is calculated through the Genetic Algorithms, on the Hybrid models only. These models are trained multiple times to detect the inputs combination that produces the lowest error. The Genetic Algorithms are elaborated in a hybrid model on the inputs layer only topology. The Batch learning was preferred to update the weights of hybrid neuro-genetic JE, after the presentation of the entire training set. The Genetic Algorithms also resolved the problem of optimal values in all the hidden layers and the output in: a) the Step Size and b) the Momentum Rate. JE nets require multiple training to achieve the lowest error.

8. DATA OF NEURAL COMPUTATION

Data came by 1411 companies from the loan department of a Greek commercial bank, with the following 16 financial indices: 1) EBIT/Total Assets, 2) Net Income/Net Worth, 3) Sales/Total Assets, 4) Gross Profit/Total Assets, 5) Net Income/Working Capital, 6) Net Worth/Total Liabilities, 7) Total Liabilities/Total assets, 8) Long Term Liabilities /(Long Term Liabilities + Net Worth), 9) Quick Assets/Current Liabilities, 10) (Quick Assets-Inventories)/Current Liabilities, 11) Floating Assets/Current Liabilities, 12) Current Liabilities/Net Worth, 13) Cash Flow/Total Assets, 14) Total Liabilities/Working Capital, 15) Working Capital/Total Assets, 16) Inventories/Quick Assets, and a 17th index with initial classification, by bank experts Courtis (1978). The test set was 50% of overall data, and the training 50%. The 1411 companies are unique, the observation has discrete frequency in 3 different annual values and the average is implemented, Courtis (1978), the dependent value ε_τ is binary, in 0 for the healthy, and 1 for the distressed companies. The classification process of the MLP and SOFM models is advanced by the appropriate classifier, Kohonen (1982).

Table I. Optimal SOFM model out of the 20 variations

Models	**Performance**											
	Layers	**0→0**	**0→1**	**1→0**	**1→1**	**MSE**	**NMSE**	**r**	**%error**	**AIC**	**MDL**	**Time**
SOFM NN	8	50	50	50	50	0.785	1.857	0.082	45.13	1174.37	2036.72	57''
SOFM NN	5	50	50	50	50	0.999	1.929	0.073	44.36	1042.53	1828.12	2' 00''
Hybrid SOFM Inp. GA	8	50	50	50	50	0.454	1.219	0.016	27.1	250.52	767.56	6h 03' 27''

Table II. Optimal Jordan Elman models, 20 cases

	Layers	**0→0**	**0→1**	**1→0**	**1→1**	**MSE**	**NMSE**	**r**	**%error**	**AIC**	**MDL**	**Time**
Jordan Elman NN	1	99.91	0.08	3.20	96.78	0.022	0.053	0.972	37.603	-2407.8	-2212.1	4''
J Elman GA inputs	1	100	0	8.25	91.74	0.027	0.065	0.966	40.46	-2352.8	-2226.1	20' 01''
Jordan Elman NN	2	99.91	0.08	4.12	95.86	0.035	0.084	0.960	45.335	-2006.4	-1785.1	5''

9. Results and Problem Definition

The performance of the SOFM networks was very poor in terms of performance with very low r, classification, but fast times only for the neural nets. Specifically the SOFM NN with 8 layers had the best performance at 0.082 which is very disappointing, the classification of companies was at 50% for all cases, the errors very high, and the partiality also very strong. On the other hand the Jordan Elmans excelled in terms of fitness to the model on the data in r reaching almost 1, very high classification evaluations, as the healthy companies ranking almost agreed to the rankings of human experts, so did the distressed companies as well; very high performance with least error low to medium partiality , and very low times for the JE NN and medium for the hybrid. Specifically the best performance was observed on the JE NN of 1 layer as the classification was almost excellent providing a fine performance at 99.91% for the healthy companies and 96.78% for the distressed as well, the fitness of the model to the data was extremely high at 0.972, the error was very low at 0.022, the NMSE was also very low 0.053 and the proportional error 37.60%, a high impartiality as the Akaike was -2407.8 in a very fast computing time 4 seconds. Second was ranked the hybrid JE of 1 layers Genetic Algorithms on the input layers, the classification was also excellent in a perfect 100% performance for the healthy companies and 91.74% on the distressed, the r was extremely high at 0.966 as well, the error very low at 0.027, the NMSE also very low 0.065 and the proportional error 40.46%, a high impartiality as the Akaike was -2352.8 in a fast computing time of 20minutes and 1 second. The third rank of the JEs was given to the JE NN of 2 layers, as the classification was almost excellent at 99.91% for the healthy companies and for the distressed at 95.86%, the model's fitness to the data at 0.96, the error very low at 0.035, the NMSE was high at 0.084 and the proportional error 45.33%, and impartial of an Akaike at -1785.1, in very fast time of 5 seconds.

10. Concluding Remarks

Overall the optimal models were the Jordan Elman neural networks of 1 hidden layer with excellent classification, almost perfect fitness of the data to the model, and least error. Second was ranked the Hybrid Jordan Elman of I hidden layer with fine classification and fitness to the model and equivalent low error. On the third rank was the Jordan Elman neural network of 2 layers with superior classification, slightly lower than the previous models.

The SOFMs underperformed characteristically and cannot be considered as reliable classifiers for portfolio selection.

Table III. Optimal models among the 40 SOFM and Jordan Elman models

	Layers	0→0	0→1	1→0	1→1	MSE	NMSE	r	%error	AIC	MDL	Time
Jordan Elman NN	1	99.91	0.08	3.20	96.78	0.022	0.053	0.972	37.603	-2407.8	-2212.1	4''
J Elman GA inputs	1	100	0	8.25	91.74	0.027	0.065	0.966	40.46	-2352.8	-2226.1	20' 01'''
Jordan Elman NN	2	99.91	0.08	4.12	95.86	0.035	0.084	0.960	45.335	-2006.4	-1785.1	5''
SOFM NN	8	50	50	50	50	0.785	1.857	0.082	45.13	1174.37	2036.72	57''
SOFM NN	5	50	50	50	50	0.999	1.929	0.073	44.36	1042.535	1828.12	2' 00''
Hybrid SOFM Inp. GA	8	50	50	50	50	0.454	1.219	0.016	27.1	250.52	767.56	6h 03' 27''

11. References

Courtis J., (1978), Modelling a Financial Ratios Categoric Framework, Journal of Business Finance & Accounting, 5, 371 – 386,

Holland, J. H., (1975/1992), Adaptation in Natural and Artificial Systems. Cambridge, MA, *MIT Press*, Second edition (1992). (First edition, University of Michigan Press)

Kohonen, T., (1982), Self-Organized Formation of Topologically Correct Feature Maps, Biological Cybernetics, 43 (1): 59–69,

Loukeris N., (2008), Comparative Evaluation of Multi Layer Perceptrons to hybrid MLPs with Multicriteria Hierarchical Discrimination and Logistic Regression in Corporate Financial

Analysis, *11th International Conference on Computers CSCC*, Elounda Agios Nikolaos, Crete, Greece 26-28 July

Loukeris, N., D. Donelly, A. Khuman, Y. Peng, (2009), A numerical evaluation of meta-heuristic techniques in Portfolio Optimisation, *Operational Research*, Volume 9 (1), ed. Springer,

Loukeris N., and I.Eleftheriadis, (2012a), Bankruptcy Prediction into Hybrids of Time Lag Recurrent Networks with Genetic optimisation, Multi Layer Perceptrons Neural Nets, and Bayesian Logistic Regression, Proc. *Int.Summer Conference* of the *International Academy of Business and Public Administration Disciplines (IABPAD),* Honolulu, Hawaii, USA (August 1- 5) - *Research Paper Award*

Loukeris N., Eleftheriadis I., and S. Livanis (2014a) Optimal Asset Allocation in Radial Basis Functions Networks, and hybrid neuro-genetic RBFNs to TLRNs, MLPs and Bayesian Logistic Regression, *World Finance Conference*, July 2-4, Venice, Italy

Loukeris N., Eleftheriadis I. and E. Livanis (2014b), Portfolio Selection into Radial Basis Functions Networks and neuro-genetic RBFN Hybrids, *IEEE 5th Int.Conference IISA*, July 7-9, Chania Greece,

Loukeris N. and I. Eleftheriadis, (2015b), Further Higher Moments in Portfolio Selection and A-priori Detection of Bankruptcy, under Multi Layer Perceptron Neural Networks, Hybrid Neuro-Genetic MLPs, and the Voted Perceptron, International Journal of Finance and Economics, 20(4), October, ed. Wiley co,

Loukeris N., I. Eleftheriadis, (2017), Control of Corporate Ownership in the Evolutional Portfolio Intelligent Complex Optimization (EPICO) model, *Corporate Ownership and Control 14(4-1), 271-285*,

Loukeris N., Chalamandaris G., Eleftheriadis I. (2019), Self Organized Features Maps SOFM and hybrid neuro-genetic SOFMs in optimal portfolio management, *IEEE 2019 International Conference on Computational Science and Computational Intelligence, CSCI 2019*, Symposium on Artificial Intelligence (CSCI-ISAI) 5-7, December, Las Vegas, Nevada, USA

Loukeris N., and I.Eleftheriadis, (2012a), Bankruptcy Prediction into Hybrids of Time Lag Recurrent Networks with Genetic optimisation, Multi Layer Perceptrons Neural Nets, and Bayesian Logistic Regression, Proc. *Int.Summer Conference* of the *International Academy of Business and Public Administration Disciplines (IABPAD),* Honolulu, Hawaii, USA (August 1- 5) - *Research Paper Award*

Loukeris N., Eleftheriadis I., and S. Livanis (2014a) Optimal Asset Allocation in Radial Basis Functions Networks, and hybrid neuro-genetic RBFNs to TLRNs, MLPs and Bayesian Logistic Regression, *World Finance Conference*, July 2-4, Venice, Italy

Loukeris N., Eleftheriadis I. and E. Livanis (2014b), Portfolio Selection into Radial Basis Functions Networks and neuro-genetic RBFN Hybrids, *IEEE 5th Int.Conference IISA*, July 7-9, Chania Greece,

Loukeris N. and I. Eleftheriadis, (2015b), Further Higher Moments in Portfolio Selection and A-priori Detection of Bankruptcy, under Multi Layer Perceptron Neural Networks, Hybrid Neuro-Genetic MLPs, and the Voted Perceptron, International Journal of Finance and Economics, 20(4), October, ed. Wiley co,

Loukeris N., I. Eleftheriadis, (2017), Control of Corporate Ownership in the Evolutional Portfolio Intelligent Complex Optimization (EPICO) model, *Corporate Ownership and Control 14(4-1), 271-285*,

Loukeris N., Chalamandaris G., Eleftheriadis I. (2019), Self Organized Features Maps SOFM and hybrid neuro-genetic SOFMs in optimal portfolio management, *IEEE 2019 International Conference on Computational Science and Computational Intelligence, CSCI 2019*, Symposium on Artificial Intelligence (CSCI-ISAI) 5-7, December, Las Vegas, Nevada, USA

THE OVERVIEW OF MACHINE LEARNING APPLICATIONS FOR AGRICULTURE BASED ON HYPERSPECTRAL DATA

Ruszczak, Bogdan[1, 2], and Kawalec, Zbigniew[2]

[1]Department of Computer Science, Opole University of Technology
Prószkowska 76 Street, 45-758 Opole, Poland
b.ruszczak@po.edu.pl

[2]R&D Department, QZSolutions
Ozimska 72A Street, 45-310 Opole, Poland

1. INTRODUCTION

Today's large-scale agriculture is a rapidly developing and innovative industry. In order to improve the efficiency of its processes, many advanced control and monitoring systems are being implemented. On the side, vast amounts of data are collected, that are related to those processes but also linked to its environment. The stored data of various types, like sensors readouts, field measurements, imagery, and orthophoto maps, reflects the progress of the vegetation process and accompanying events.

Often, to improve the overall efficiency of the process the changes need to be issued to the small, indistinct, hard to spot details, not obvious patterns, or outwardly not related information. Though to study the collected data it is essential to utilize the set of methods that enable us to distinguish such internal data relations. The current state of the art for such datasets analysis is the machine learning application. The paper provides an overview of several machine learning applications supplied with hyperspectral data to provide compelling results for agricultural processes.

2. UTILISATION OF IMAGERY AND HYPERSPECTRAL DATA FOR AGRICULTURE

In the last few years, there have been few new hyperspectral devices presented. There are both spectrophotometers, that let one perform high accuracy point material reflectance measurements, and hyperspectral cameras.

Both types of devices improved a lot in terms of the quality of the collected data. Its development resulted in increased both spatial and spectral resolution, but also miniaturization of devices. Increasingly smaller cameras allow us to perform remote hyperspectral data acquisition (using such devices as Zebra X1 - www.kplabs.pl/en/zebra-x1 or Headwall's New Nano-Hyperspec) assemble to a UAV, and that was possible before only using costly airplanes. It is worth to mention on the upcoming satellite missions (i. e. Italian Space Agency hyperspectral mission Prisma – www.prisma-i.it, or German hyperspectral satellite mission EnMAP - The Environmental Mapping and Analysis Program - www.enmap.org/), that are targeted to provide hyperspectral imagery (HSI) as well.

So far there are many solutions based on multispectral imagery, like for instance the most popular, that utilizes the near infrared-based NDVI index for nitrogen fertilization aid, or some other multispectral indices *Słapek et al. (2019).* The increasing accessibility of hyperspectral imagery, should provide enough data for wide areas, and let to use it for the need of precision farming, that requires information for whole fields.

3. MACHINE LEARNING

The HIS is a valuable data source, especially for agriculture, and allows us to extract otherwise unobtainable information. However, there are some challenges related to HIS processing. The data collected using hyperspectral sensors grows quickly and often goes in large volumes of several gigabytes or more. The other thing is that the needed information could be not apparent and require advanced extraction.

Therefore the use of appropriate methods is advisable. With the development and continuation of classic image processing techniques, the machine learning methodology comes into play. In particular, to discover advanced patterns hidden in between channels, or channels combinations, or the individual patterns on component images, deep learning methods could be needed *Michalski et al*. (2018)

4. AN OVERVIEW OF MACHINE LEARNING APLICATIONS FOR AGRICULTURE

Hyperspectral data is useful for many studies of natural phenomena like habitat mapping, flood detection and monitoring, environmental degradation and hazards, gas emissions from ground sources, evapotranspiration, soil erosion and land degradation. It could be very effective while researching soil mineral composition, carbon storage in soils, surface contamination, soil pollution or soil contamination. There are also many marine-related applications like the detection of oil spills, marine litter, coastal erosion or coastal vulnerability.

There are many operative applications for precision agriculture that benefit from HIS, the main are:

- vegetation species identification,
- biomass estimation, yield assessment and forecast,
- crop health and damage (i.e. nutrient stress), plant diseases detection, crop water estimation,
- water resources management (water stress, droughts),
- invasive species detection (i. e. weeds),
- digital soil mapping (mapping and characterization of soil properties)
- nutrient cycles.

Those applications are usually dedicated to the specific crop as they are image-based, and the appearance of crops differs. Some of the methods are also limited to the specific conditions, and could be applied for specific: climate, soil, or location related conditions. Therefore the HSI utilization for agriculture is subject to many studies to boost its wider use for precision agriculture.

Figure 1. The fragment of hyperspectral orthophoto map from experimental potato fields (image build of 3 channels selected from the total of 150 channels)

4.1 Potato water stress modeling

The observation of plants' water stress is possible with the use of HSI. Some of the spectral channels allow one to distinguish the stress level. In Figure 1. the image from the experimental potato fields is presented (it contains 150 channels but only 3 of them could be visualized). As each set of fields has been treated differently they show different spectral characteristics (3 samples

presented in Figure 2.). The HSI images and precise soil moisture and leaf measurements became later the dataset for the machine learning model of that phenomenon.

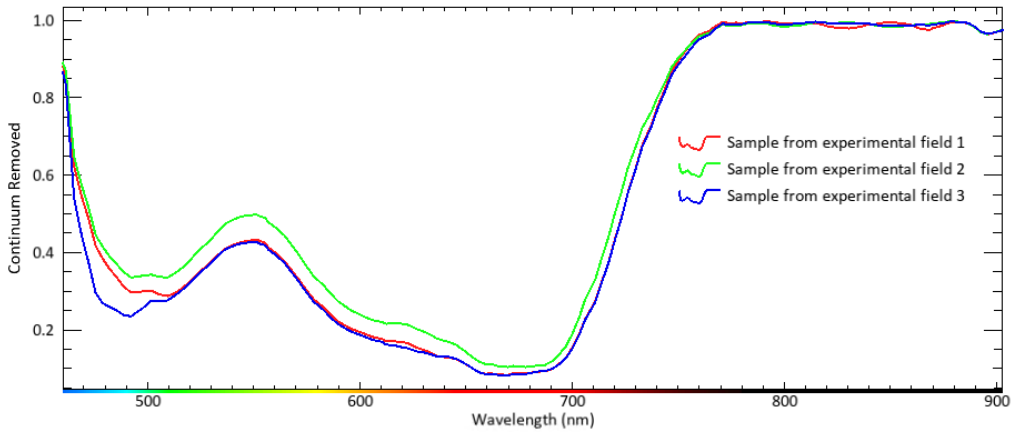

Figure 2. The spectral characteristic of 3 different samples from experimental fields. Each sample refers to the potato leaves exhibiting different water stress level

4.2 Potato pathogen detection

Another example of hyperspectral data application is the identification of plant diseases. For some particularly valuable crops, it could be required to prepare a tool that could help to detect the disease before it shows any easily distinguishable symptoms. As the study reviled, it is possible for instance for potatoes *Smykała et al. (2020)*. The high effectiveness was reached for the *Alternaria solani* pathogen that is frequently occurring on tomatoes. For final model training, the dataset of hyperspectral measurements of tomatoes was used with the the implementation of ensemble learning method. After subsequent iterations of the training process and adjustment of hyperparameters, satisfactory accuracy results, equal to 0.987 for the random forest, were obtained Pathogens Ruszczak et al. (2020).

5. CONCLUSION

The usage of machine learning methods and hyperspectral imagery should result in the increasing efficiency of many agriculture processes and will help to make many farmers' decisions. The provided orthophoto maps would let aid the crop irrigation and fertilization or pathogen detection.

Although many of the described agriculture applications are still in the research phase, the rapid development of machine learning methods and the growing accessibility of hyperspectral data will result in many new agricultural projects benefiting from those. In the following years, there will be many new utilizations for that methodology.

The important impulse for those projects should be the start of the following satellite missions that are scheduled, such as the German Spaceborne Imaging Spectrometer Mission EnMAP, or similar missions run by Chinese, Indian, US, or Italian agencies. With every vegetation season and every following year, the agricultural datasets will grow and will significantly boost the precision of the developed applications.

6. ACKNOWLEDGMENT

The author would like to express appreciation for The National Centre of Research and Development of Poland that supported this work under the project: POIR.04.01.04-00-0009/19-00.

7. REFERENCES

Michalski P., Ruszczak B., Tomaszewski M.: Convolutional Neural Networks Implementations for Computer Vision, Advances in Intelligent Systems and Computing, vol. 720, Springer, 2018, doi: 10.1007/978-3-319-75025-5_10

Ruszczak B., Smykała K., Dziubański K.: The detection of Alternaria solani infection on tomatoes using ensemble learning, Journal of Ambient Intelligence and Smart Environments, vol. 12, no. 5, pp. 407-418, 2020, doi: 10.3233/AIS-200573

Słapek M., Smykała K., Ruszczak B.: Brassica Napus Florescence Modeling Based on Modified Vegetation Index Using Sentinel-2 Imagery, Lecture Notes in Computer Science, vol. 11509, in: Artificial Intelligence and Soft Computing, 2019, doi: 10.1007/978-3-030-20915-5_8

Smykała K., Ruszczak B., Dziubański K.: Application of Ensemble Learning to Detect Alternaria Solani Infection on Tomatoes Cultivated Under Foil Tunnels, 16th International Conference on Intelligent Environments: Madrid, 2020, IOS Press, Ambient Intelligence and Smart Environments, Vol. 28, pp. 127-132, Intelligent Environments 2020, doi: 10.3233/AISE200033

PAVING THE WAY FOR REALISTIC MODELING OF RIS-ENABLED COMMUNICATIONS

Liodakis, G.[1], and Vardiambasis, I.O.[1]

[1] Laboratory of Telecommunications & Electromagnetic Applications, Department of Electronic Engineering, Hellenic Mediterranean University
Chania, Crete, Greece
gsl@hmu.gr

1. INTRODUCTION

Reconfigurable Intelligent Surfaces (RISs) are recently considered as one of the promising technology enablers for the next generation wireless networks, such as 6G cellular networks. RISs have the capability to modify the radio waves of signals impinging upon them in ways that can be programmed and controlled by using external stimuli, Renzo et al. (2020). Actually, RISs may become the paradigm shift for implementing the so-called smart radio environment. In such a case, the uncertain and formerly uncontrollable wireless environment is considered as an optimization variable which, along with transmitters and receivers, may allow a joint treatment of them for various optimization tasks.

Moreover, it is anticipated that future wireless networks will be characterized by a much greater complexity in comparison to past and current networks, due to network architectural issues, the heterogeneity of demanded services, etc. As a consequence, the typical modeling approach through the derivation of mathematical models with the associated trade-offs between their accuracy and tractability is not adequate anymore. Machine learning techniques may enhance the overall modeling approach for various tasks (network design and deployment, optimization procedures, performance evaluation, network operation, etc.), as depicted in Figure 1.

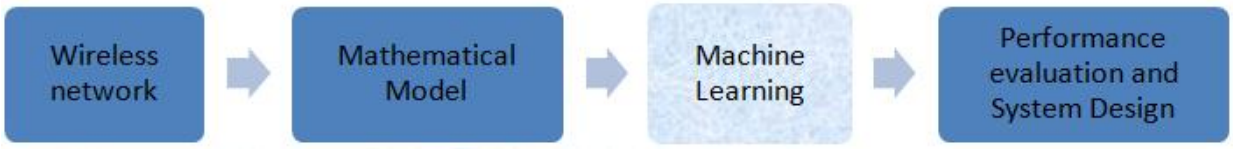

Figure 1. Modeling wireless networks with/without machine learning techniques.

Research for exploiting the concept of RISs towards the smart radio environment realization is relatively limited, especially as it concerns modeling efforts for the subsequent network performance evaluation. More specifically, early major research efforts include Renzo and Song (2019), Hou et al. (2019), Kishk and Alouini (2020), Zhu et al. (2020), and Ntontin et al. (2020). Two mathematical tools for modeling wireless networks have a prominent role in these early research works: stochastic geometry theory and random shape theory. Thus, in this paper, we pave the way for meaningful performance evaluation of RIS-enabled communications by identifying basic network modeling choices related to the Mobile Stations (MSs), the Base Stations (BSs), the communication blockages and the RIS-equipped blockages in various deployment scenarios. Prior to these modeling choices (Section 3), Section 2 provides some background information about the RIS-enabled communication environment, whereas Section 4 concludes the paper.

2. BACKGROUND ON RIS-ENABLED COMMUNICATIONS

RISs constitute a physical-layer technology that alters the wavefront (e.g., the phase, amplitude, frequency, polarization) of the impinging signals on appropriately man-made structures. More specifically, these structures (internal walls, front facades or entire buildings, etc) are being

transformed to electromagnetically active surfaces by realizing elementary electromagnetic-based functions (reflection, refraction, absorption, splitting, collimation, focusing/beamforming, etc.), Yang and Rahmat-Samii (2019). In practice, RISs are implemented either by smart surfaces made of discrete tiny antenna elements, or by smart metasurfaces usually made of some reconfigurable material.

RISs may be employed for a variety of application scenarios envisaged in 6G cellular networks, such as facing signal coverage issues, ensuring signal secrecy at eavesdroppers, improving localization accuracy, etc. For example, as shown in Figure 2, due to the non-existence of direct Line-of-sight (LoS) links between the BS and users u_1 and u_2, the RIS-equipped blockage R_1 can provide indirect Line-of-sight (LoS) links to the corresponding MSs. The R_1 may consist of a 2D array of reflective units that alter the impinging radio waves and are controlled by a microcontroller, whereas the reconfigurability is achieved by low power tunable electronic circuits with electromagnetic functions.

From a smart radio environment point of view, we should notice that the use of RISs may result in a move of functions usually implemented at the radio end-points to the communications environment itself (e.g., beamforming). All in all, however, the appropriate exploitation of RISs requires a careful examination and dimensioning for the overall communication chain and is amenable to realistic modeling assumptions.

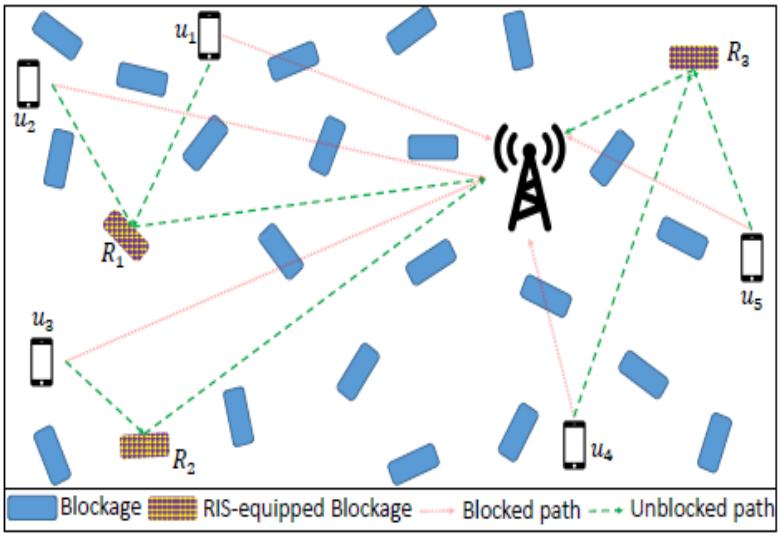

Figure 2. RIS-enabled communication environment, Kishk and Alouini (2020).

3. TOWARDS REALISTIC MODELING

The evolution of future wireless networks, such as 6G cellular communication networks, will pose new demanding challenges on performance evaluation issues. In particular, a shift from spatial to volumetric performance metrics is envisaged. For instance, current approaches for spectral and energy efficiency should be elaborated in 3D. Thus, a move from bps/Hz/km^2 (4G) and bps/Hz/km^2/Joules (5G) to bps/Hz/km^3/Joules for 6G, should be strived for performance evaluation purposes. The same, also, holds for the basic performance metrics (e.g. the direct and indirect LoS probabilities between a BS and a MS, the reflection probability of RISs, the probability of associations through an RIS) of the overall analytical framework for realistic modeling purposes.

Other major modeling assumptions are related to the exploitation of multiple frequency bands (below 6 GHz, mmWave, THz). In particular, a scenario specific modeling is required for the realization of mobile mmWave networking and for the introduction of "tiny cells" with a radius of a few tens of meters (in case of THz communication). As a consequence, the incorporation of new high-frequency mobility management techniques and user-association algorithms should be taken into account for meaningful performance evaluation.

Modeling the spatial deployment of BSs and MSs for current network implementations is dominated by the use of tools from stochastic geometry (spatial distribution models, random tesselations for coverage studies, random graphs for connectivity issues). However, the great majority of research works adopt 2D models, mostly due to the use cases under examination. More specifically, the 2D Homogeneous Poisson Point Process (HPPP) spatial distribution model is the most widely adopted model for analytical tractability reasons. This PPP model (upper part of Figure 3) is used to denote the complete spatial randomness of both BSs and MSs by the consideration of two independent spatial stochastic processes with only the aid of the density parameter λ (e.g., λ_{BS} for each set of BSs, λ_{MS} for the MSs). However, the 2D HPPP model cannot capture use cases with clustered users (lower part of Figure 3) or the use cases envisaged for 6G (e.g., in the presence of UAVs). In other words, along with the appropriate spatial distribution model for each of the communicating entities and the 3D communication requirements of future networking scenarios, a compromise between analytical tractability and realistic modeling is required.

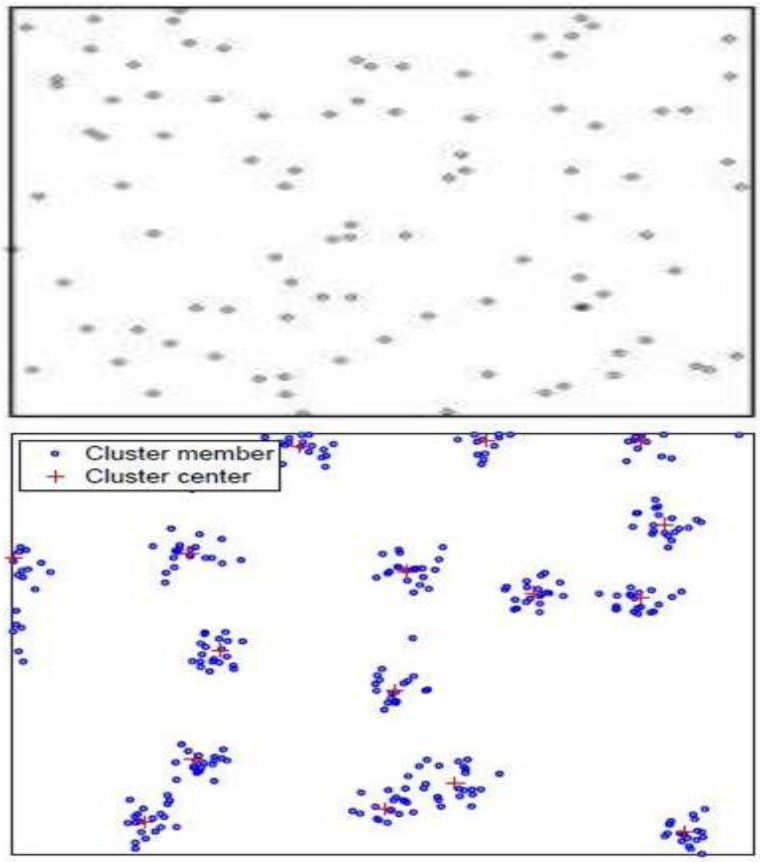

Figure 3. HPPP and cluster spatial distribution models.

Another branch of applied mathematics, i.e., the Random Shape Theory, has been recently applied to analyze the blockage effects on system performance. In particular, the authors of Bai et al. (2014) used the line Boolean model for the blockages. According to this model, the midpoints of the blockages are modeled as an HPPP with spatial density λ_b, while the length and orientation of the blockages are assumed to follow a specific probability distribution function (e.g., uniform distribution). However, in case of RIS-enabled communications, some blockages may act as an RIS. Therefore, an additional spatial density $\lambda_{RIS} = \alpha \lambda_b$ as a fraction of λ_b, should be defined for the surfaces that are composed of a number of reflective elements. Moreover, this number of reflective elements should be defined also as either a fixed number for each RIS or a random variable with a specific probability mass fumction. Other possible modeling approaches beyond the line Boolean model include the line segments with height and the rectangle with height models, in order to be inline with the 3D communication setup under examination.

In essence, practical considerations and restrictions may lead to other options for modeling the incorporation of RISs in each use case. Thus, one should discriminate between indoor and outdoor scenarios, between RIS random deployment as described above and RIS planned deployment at strategic locations, as well as between the inclusion of one or more sides of a building to be covered with RISs. Finally, there is the need to model the hardware imperfections of the tranceivers (non-linearities, in-phase and quadrature imbalance, phase noise, etc.) in a RIS-enabled communication system, as such imperfections significantly limit the wireless system performance, Boulogeoorgos and Alexiou (2020).

4. CONCLUSION

Various modelling paths striving for realistic models of RIS-enabled communication and based mainly on the exploitation of stochastic geometry and random shape theories were examined in this paper. Such a realistic modelling will promote the seamless integration of RISs to the future more spectral and energy efficient wireless networks and will facilitate a greater synergy with other state-of-the-art and emerging technologies (small cells, massive MIMO, use of mmWave and THz frequencies, energy harvesting, etc.). The achievement of realistic modelling will be, also, of great benefit for mobile network operators. More specifically, it will provide them a greater flexibility due to the exploitation of a smart radio environment and will facilitate a more reliable techno-economic analysis, thus contributing to the viability of future deployments (e.g., beyond 5G and 6G networks).

5. REFERENCES

Bai, T., R. Vaze, and R.W. Heath. 2014. Analysis of blockage effects on urban cellular netweorks. IEEE Transactions on Wireless Communications, 13: 5070-5083.

Boulogeorgos, A.A., and A. Alexiou. 2020. How much do hardware imperfections affect the performance of reconfigurable intelligent surface-assisted systems? IEEE Open Journal of the Communications Society, 1: 1185-1195.

Di Renzo, M., and J. Song. 2019. Reflection probability in wireless networks with metasurface-coated environmental objects: An approach based on random spatial processes. EURASIP Journal on Wireless Communications and Networking, Article 99.

Di Renzo, M., A. Zappone, M. Debbah, M.S. Alouini, C. Yuen, J.D. Rosny, and S. Tretyakov. 2020. Smart radio environments empowered by reconfigurable intelligent surfaces: How it works, state of research, and road ahead. IEEE Journal on Selected Areas in Communications, 38: 2450-2525.

Hou, T., Y. Liu, Z. Song, X. Sun, Y. Gehen, and L. Hanzo. MIMO assisted networks relying on large intelligent surfaces: A stochastic geometry model. 2019. arXiv:1910.00959.

Kishk, M.A., and M.S. Alouini. 2020. Exploiting randomly-located blockages for large-scale deployment of intelligent surfaces. IEEE Journal on Selected Areas in Communications, doi: 10.1109/JSAC.2020.3018808.

Ntontin, K., M.D. Renzo, and F. Lazarakis. 2020. On the rate and energy efficiency comparison of reconfigurable intelligent services with relays. 21st IEEE International Workshop on Signal Processing Advances in Wireless Communications (SPAWC): 1-5.

Yang, F., and Y. Rahmat-Samii. 2019. Surface electromagnetics: with applications in antenna, microwave, and optical engineering. Cambridge University Press.

Zhu, Y., G. Zheng, and K.K. Wong. 2020. Stochastic geometry analysis of large intelligent surface-assisted millimeter wave networks. IEEE Journal on Selected Areas in Communications, 38: 1749-1762.

IMPLICATIONS ON ELF ELECTRIC FIELD DISTRIBUTION DUE TO SPACECRAFT CONDUCTIVE BOUNDARIES

Baklezos, A.T. *, Vardiambasis, I.O., Kapetanakis, T.N., Fragiadakis, N., and Nikolopoulos C.D.

Laboratory of Telecommunications & Electromagnetic Applications, Department of Electronic Engineering, Hellenic Mediterranean University
Chania, Crete, Greece
* abaklezos@hmu.gr

1. INTRODUCTION

A common process in early design stages of a space mission is the measurement of the candidate equipment at a unit-level test campaign. Using the results, EMC engineers try to develop a robust design of the platform at system-level taking into consideration the strict electromagnetic cleanliness requirements as discussed in Brown et al. (2019), Matsushima et al. (2010), Madhusudan et al. (2006), Narvaez et al. (2004), and Pudney et al. (2019). A possible route is to assemble the platform pseudo-randomly based solely on best approaches and measure the platform again as a system. In case of failure to meet the cleanliness requirements the system behavior cannot easily be redeemed and the task is expensive. Another, better, route is to model the behavior of the units as e.g. in Mehlem et al. (2012), or Dumond et al. (2012), or Baklezos et al. (2019), and simulate the system behavior as discussed e.g. in Junge et al. (2012), or Koutantos et al. (2017). This way, a number of suboptimal setups is disregarded, leading to better design as well as reducing the cost of the design phase.

Regarding space missions with scientific goals in the DC or the extremely low frequency spectrum like Turbulence Heating ObserveR, Solar Orbiter, Juice, etc., the practice is to measure and model the units in this frequency range. This range corresponds to large wavelengths (over 1 km) which are much greater than all system related lengths. For this reason, a quasi-static modelling approach as presented in Baklezos et al. (2019), Koutantos et al. (2017), and Nikolopoulos et al. (2020) is well-justified resulting in dipole models for each unit. According to the methodology each unit has a distinct dipole model for each frequency. Having the quasi-static models of the units enables the simulation of the behavior of the system with the summation of the electric (or magnetic) fields of all units at a specific location inside or outside of the spacecraft, where sensitive equipment or sensor is to be placed. The ideal unit placement would be the one that produces zero field at the victim unit (sensor) location.

This work employs this quasi-static unit level electric signature characterization and through a heuristic approach, produces an optimal equipment placement that yields a minimization of the system-level electromagnetic field in a selected volume of interest. Also, the methodology takes into consideration the size of the equipment units as well as the possible angles of rotation for each unit in order to avoid overlaps as well as collisions with the spacecraft walls providing only feasible placements. It is clear that the factor separating a particular placement from the rest in the feasible set is the electric field distribution inside the spacecraft and specifically in the volume of interest, where the victim unit is to be placed (sensor).

In case the victim unit is in the interior of the spacecraft, the spacecraft structure itself is used only to define the space that the units will be placed in, attempting to minimize the electric field at the victim volume. However, in this work, authors demonstrate that in the aforementioned scenario, the conductive boundaries of the spacecraft actively alter significantly the electric field distribution inside the spacecraft and so their effect must be included in the methodology for the optimal unit placement.

2. PROBLEM DESCRIPTION & CONSIDERATIONS

Multiple units or Devices Under Test (DUTs) are on board of a mission platform as it is comprised of many different devices and instruments. While the exact electromagnetic environment is synthesized by the total of these devices, usually only a few have the greatest contribution and define the behavior of the system. So, in this work, the contribution of two DUTs at a single frequency is considered. The models of actual DUTs have been extracted according to Koutantos et al. (2017) and Baklezos et al. (2019), based on measurements in line with the methodology presented in Nikolopoulos et al. (2018). These models provide the electric moments for the artificial DUTs employed in this work in order to highlight the practical implications.

The near field approximation of the electric field of a single oscillating dipole is expressed as:

$$\vec{\mathrm{E}}(\vec{\mathrm{n}},\mathrm{t}) = \frac{\mathrm{e}^{-\mathrm{i}\omega\mathrm{t}}}{4\pi\varepsilon_0}\{3\vec{\mathrm{n}}(\vec{\mathrm{n}}\cdot\vec{\mathrm{p}}) - \vec{\mathrm{p}}\}\,\frac{1}{\mathrm{r}^3} \qquad [1]$$

where $\vec{r} = \overrightarrow{R}_{obs} - \overrightarrow{R}_{dipole}$, $r = |\vec{r}|$, $\vec{n} = \frac{\vec{r}}{r}$, $\overrightarrow{R}_{dipole}(x,y,z)$, and $\vec{p}$ (p_x, p_y, p_z) are the spatial coordinates and the moment vectors of the source (dipole), and $\vec{R}_{obs}$ $(x_{obs}, y_{obs}, z_{obs})$ is the position vector of an observation point M. The total electric field amplitude of N dipoles at the observation point is:

$$\left|\vec{E}_{total}\right|_N = \left|\sum_{i=1}^{N}\vec{\mathrm{E}}_i\right| \qquad [2]$$

The exact configuration of moments that is assigned to the dipoles (DUTs) is tabulated in Table 1 and placed arbitrarily inside the container volume representing the spacecraft boundaries. Of course, the methodology is also applicable in the case of multiple electric dipoles per DUT.

Table 1. Dipole's electric moments.

Dipole/DUT	p_x $(fC \cdot m)$	p_y $(fC \cdot m)$	p_z $(fC \cdot m)$
1	3	12	4
2	8	-9	25

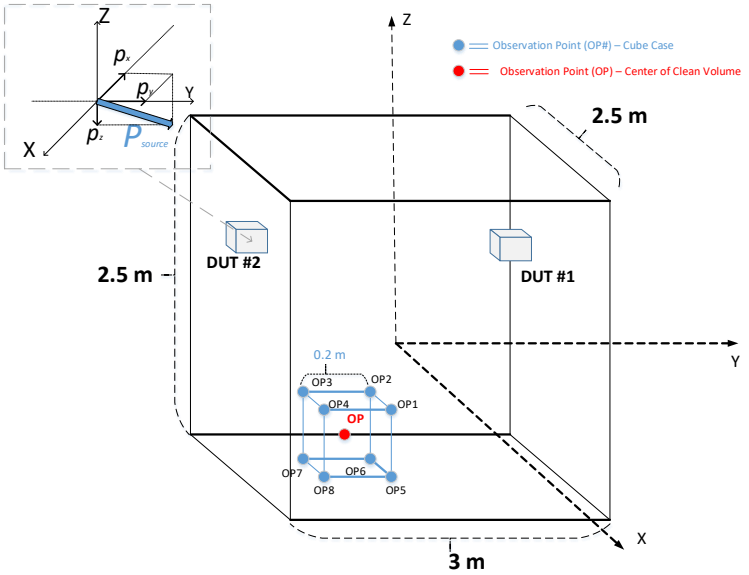

Figure 1. Observation point(s) location inside a cubic spacecraft.

The position where the victim device (measurement sensor) can be placed, assuming the cuboid spacecraft structure (e.g. Solar Orbiter's case), is the observation volume (cubic area) where electromagnetic cleanliness is required. Of course, the shape of the observation volume can be altered to accommodate different cases.

The observation cubic volume referred to by its center with coordinates (0.1,-0.1,-1.1) of the SCS, with an edge 0.2 m. The various DUTs are allowed to rotate freely only in z-axis ($0 \leq \varphi \leq 360^0$) while the other angles are discretized ($\omega, \theta: 0^0, 90^0, 180^0, 270^0$) in order to be placed in a horizontal plane regarding spacecraft's azimuth (one DUT's face shall be parallel to the spacecraft's bottom surface).

Table 2. Dipoles optimized parameters (center position and moment orientation).

Dipole/DUT	X(m)	Y(m)	Z(m)	Ω (^{0} deg)	Θ (^{0}deg)	Φ(^{0} deg)
1	-0.5241	1.0773	0.4844	90	90	297.6525
2	-1.0303	1.1902	0.9759	270	0	13.6313

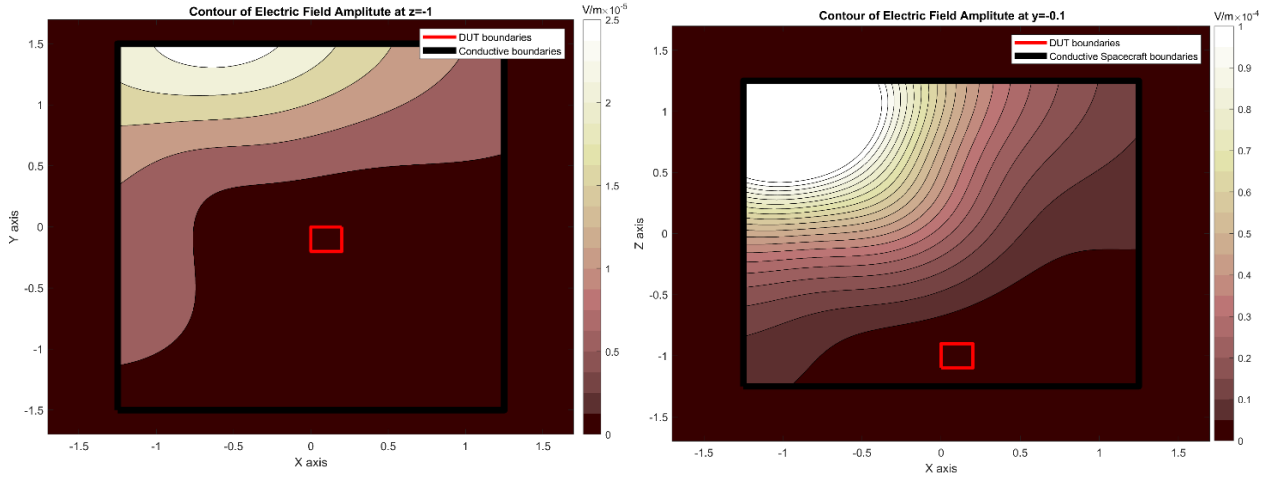

Figure 2. E-field amplitude contours (field distribution) at XY-plane for Z=-1, XZ-plane for Y=-0.1 with spacecraft and sensor boundaries.

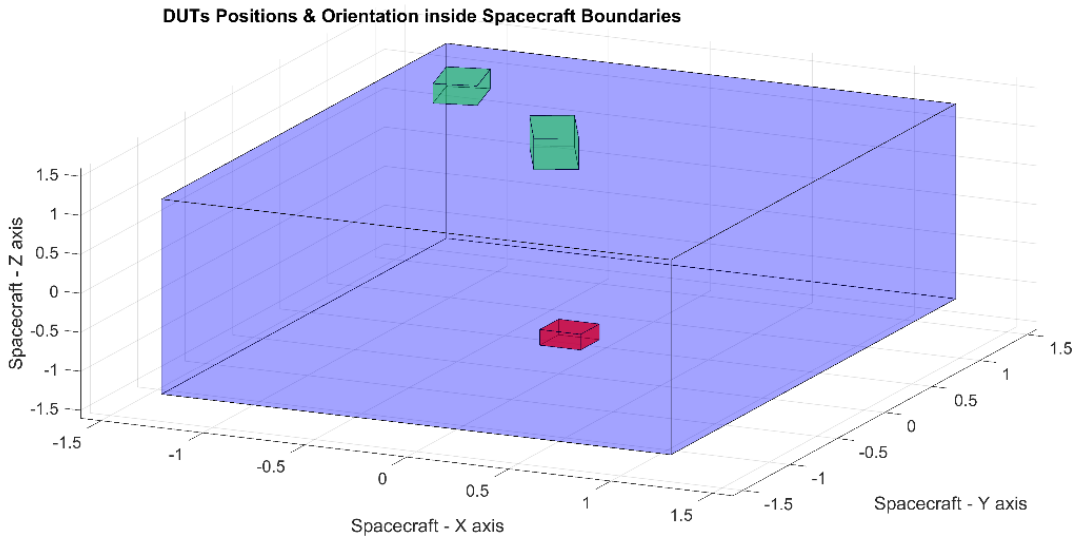

Figure 3. DUTs (green) placement and orientation for minimum electric field emissions at the selected location of the victim volume (red) inside the spacecraft.

The relative placement of the DUTs to the observation point as well as the orientation can severely alter the electric field at the observation point for a given set of sources (electric moments) so it is important to find the optimal combination of those variables in order to minimize the field in the victim volume.

For this reason, the algorithm presented in Nikolopoulos et al. (2020) is employed in order to extract the optimal placement of the units. Results are tabulated in Table 2, and the field value at the center of the observation volume is $1.6941 \times 10^{-22} V/m$.

Indicatively, the contours of the electric field amplitude at the XY-plane, Z=-1m and at the XZ plane, Y=-0.1m are depicted in Figure 2, showcasing the electric emissions distribution of the platform. Specifically, the white and yellow area of the contour indicates the areas with highest levels of emissions.

The sensitive equipment area is bounded with the red rectangle. It is apparent from Figure 2 that the allocation of payload units as tabulated in Table 2 yields the minimum field values inside the victim area (red rectangle). Figure 3 depicts the position and orientation of the DUTs for minimum electric field emissions.

3. EFFECT OF SPACECRAFT CONDUCTIVE BOUNDARIES ON THE FIELD DISTRIBUTION

The presence of the spacecraft conductive boundaries alters significantly the overall electric field distribution inside its volume. This effect can be accounted for with the introduction of a number of dipole images per source and per conductive surface as it is depicted in Figure 4.

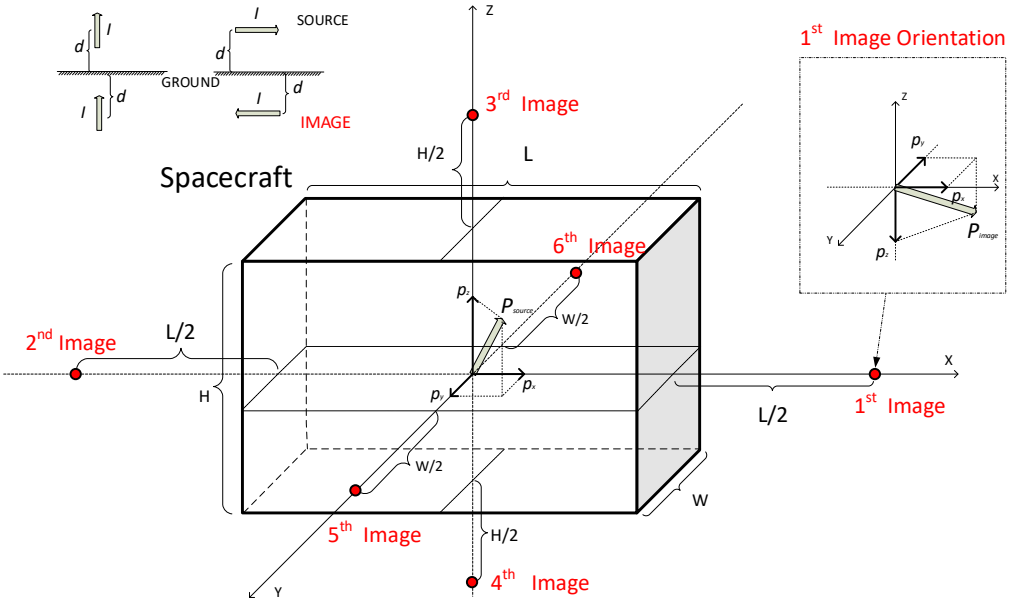

Figure 4. Image Dipole position and orientation from the spacecraft's conductive surfaces.

It should be noted that only first order images are included in this consideration. Thus, the total electric field inside the spacecraft is the sum of the electric field of each dipole and the electric field of the six images. This is true only in the internal volume of the spacecraft. Although a simplification regarding the spacecraft shape has been made in Figure 4, this treatment is valid for more complex structures with higher order images.

In order to assess the effect on the field distribution, the six images of each DUT's dipole source are included in the total field calculation along with the original source. The original source is each dipole parameters as transformed according to Table 2. With the inclusion of image sources, the field distribution is altered and the total electric field at the center of victim area (red rectangle) is $3.1812 \times 10^{-5} V/m$.

Indicatively this effect is showcased for the XY and XZ planes in Figure 5. As it is apparent the red rectangle falls outside the minimum electric field area.

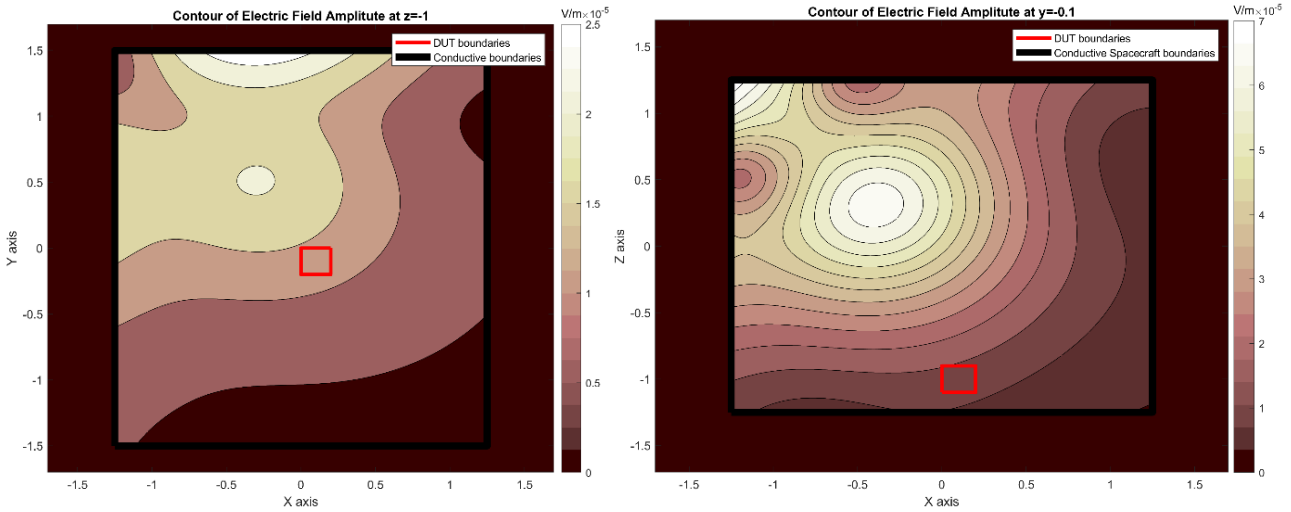

Figure 5. E-field amplitude contours (field distribution) at XY-plane for Z=-1, XZ-plane for Y=-0,1 with spacecraft and sensor boundaries with spacecraft conductive boundaries contribution.

This fact indicates the significance of the image sources contribution and necessitates the update of the placement optimization algorithm in order to account for the conductive boundaries effect.

4. CONCLUSION

In this work, the authors discuss the effect of the spacecraft's conductive boundaries on the electric field in the interior of a spacecraft and the necessary modification to the heuristic methodology capable to provide an optimal placement (position and orientation) for DUT's in a spacecraft. The scope of this study is the minimization of the total electric field at any arbitrary volume inside the spacecraft boundaries considering its conductive boundaries. Future work could include the update of the algorithm in order to account for complex structure geometries as well as a measurement campaign to validate it. Additionally, it could include the application of the proposed methodology to an actual spacecraft environment and the expansion of the methodology to include ELF electric sources for achieving electric cleanliness in different regions based on frequency requirements.

5. REFERENCES

Baklezos, A.T., C.D. Nikolopoulos, S.T. Spantideas, E.G. Chatzineofytou, M. Nicoletto, I. Marziali, D. Boschetti, and C.N. Capsalis. 2019. Steady state emissions modeling of low frequency magnetic and electric fields generated by GOCE CDMU. 2019 ESA Workshop on Aerospace EMC, Budapest, Hungary: 1-5.

Brown, P., U. Auster, J.E.S. Bergman, J. Fredriksson, Y. Kasaba, M. Mansour, A. Pollinger, R. Baughen, M. Berglund, D. Hercik, H. Misawa, A. Retino, M. Bendyk, W. Magnes, B. Cecconi, M.K. Dougherty, and G. Fischer. 2019. Meeting the magnetic EMC challenges for the in-situ field measurements on the JUICE mission. 2019 ESA Workshop on Aerospace EMC, Budapest, Hungary: 1-6.

Dumond, O., and R. Berge. 2012. Determination of the magnetic moment with spherical measurements and spherical harmonics modelling. 2012 ESA Workshop on Aerospace EMC, Venice, Italy: 1-5.

Junge, A., and F. Marliani. 2012. Verification of DC magnetic model predictions at spacecraft level. 2012 ESA Workshop on Aerospace EMC, Venice, Italy: 1-4.

Koutantos, G.I., C.D. Nikolopoulos, A.T. Baklezos, and C.N. Capsalis. 2017. On the modeling of ELF electric fields for space mission equipment. IEEE Transactions on Electromagnetic Compatibility, 59 (5): 1457-1464.

Madhusudan, Y.L., H.R. Nagendra, and T.S. Nanjundaswamy. 2006. Design techniques and methodologies for effective electromagnetic cleanliness in spacecraft power system. 2006 9th International Conference on Electromagnetic Interference and Compatibility (INCEMIC 2006), Bangalore, India: 258-269.

Matsushima, M., H. Tsunakawa, Y.-I. Iijima, S. Nakazawa, A. Matsuoka, S. Ikegami, T. Ishikawa, H. Shibuya, H. Shimizu, and F. Takahashi. 2010. Magnetic cleanliness program under control of electromagnetic compatibility for the SELENE (Kaguya) spacecraft. Space Science Reviews, 154 (1-4): 253-264.

Mehlem, K., A. Wiegand, and S. Weickert. 2012. New developments in magnetostatic cleanliness modeling. 2012 ESA Workshop on Aerospace EMC, Venice, Italy: 1-6.

Narvaez, P. 2004. The magnetostatic cleanliness program for the Cassini spacecraft. In The Cassini-Huygens Mission. Springer, Dordrecht. 385-394.

Nikolopoulos, C.D., A.T. Baklezos, and C.N. Capsalis. 2018. Measuring transient and steady state electric field emissions of space equipment for EMC and cleanliness purposes. 2018 IEEE International Conference on High Voltage Engineering and Application (ICHVE), Athens, Greece: 1-4.

Nikolopoulos, C.D., A.T. Baklezos, and C.N. Capsalis. 2020. On achieving spacecraft level magnetic cleanliness with proper equipment ordinance of DC and ELF magnetic sources. IEEE Transactions on Electromagnetic Compatibility, 62 (6): 2714-2724.

Pudney, M., S. King, T. Horbury, M. Maksimovic, C.J. Owen, and P. Laget. 2019. Solar orbiter strategies for EMC control and verification. 2019 ESA Workshop on Aerospace EMC, Budapest, Hungary: 1-6.

ESTIMATION OF RADIATED EMISSIONS OF SPACEWIRE LINK VIA HEURISTIC APPROACH FOR EMC ASSESSMENT

Nikolopoulos, C.D.*, Baklezos, A.T., Kapetanakis, T.N., Fragiadakis, N., and Vardiambasis, I.O.

Laboratory of Telecommunications & Electromagnetic Applications, Department of Electronic Engineering, Hellenic Mediterranean University
Chania, Crete, Greece
* cnikolo@hmu.gr

1. INTRODUCTION

Previous work of Nikolopoulos et al. (2019a-b) claimed that any cable that is shielded can be modeled as a travelling wave antenna and all contributing parameters (e.g. cable's topology, propagation medium, CM current in the shield, ground plane dielectric properties, etc.) have been decomposed in order to investigate its impact on the cable's electromagnetic radiated emissions. This method has been validated with monochromatic excitation over different ground schemes and heights of a coaxial cable. In this work, authors expand this previously established methodology in more complex structures and for more complex signals; exploring the case of SpaceWire cable over an aluminum ground fed with Low Voltage Differential Signal (LVDS). This specific setup is studied due to its crucial role in current ESA's or NASA's Space missions (e.g. GAIA, ExoMars, Lunar Reconnaissance Orbiter, SWIFT, BepiColombo) and applications, as it is the standard for harness and grounding design. SpaceWire is a space-application focused cable with four shielded twisted pairs employing LVDS signaling, a geometry requiring rather cumbersome calculations in order to analytically extract the radiated emissions. Authors claim that this issue can be bypassed based on the aforementioned methodology identifying the current distribution on the shield responsible for the radiation with the aid of the Differential Evolution algorithm. Results showcase that the extracted model can accurately describe the phenomenon.

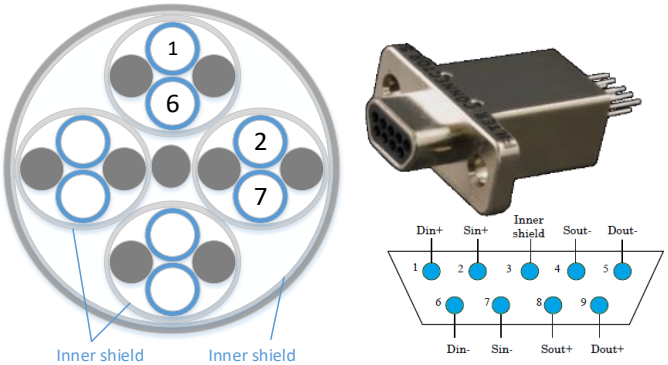

Figure 1. SpaceWire cable transverse cut and signal wiring topology, Nikolopoulos et al. (2019b).

The main idea of the method described in Nikolopoulos et al. (2019a-b) is the representation of the cable by its shielding, which is then treated as a travelling wave antenna. Consequently, the radiated emissions are attributed to the current flowing on the shield. In order to calculate the current distribution from the measured electric field, a stochastic process is selected for solving the inverse electromagnetic problem. The estimation of this current on the cable shield is achieved through a single standard EMI/EMC measurement as described in the work of Nikolopoulos et al. (2019a-b) across a frequency range of interest. The present paper, instead of trying to assign one value to the current magnitude for every measured frequency bin (monochromatic treatment) represents the current with a more realistic composition of pulses since the LVDS signal fed is a

pulse train. Moreover, the major step forward in the proposed modelling is the solving approach, where the whole spectrum is considered, as opposed to the bin by bin approach in Nikolopoulos et al. (2019a-b). This way a single inverse problem is solved instead of numerous (depending on the frequency bins / frequency resolution). This single inverse problem is solved with the Differential Evolution (DE) algorithm. Differential Evolution (DE) algorithm, first introduced from Storn & Price (1995), is a powerful and well-known optimization tool which has been used in many scientific problems over different fields while it is still employed in engineering and aerospace domains for various purposes. Authors in this work add the variations of Dawar & Ludwig (2014) and Kumar &Pant (2012) regarding mutation strategies and techniques of the DE algorithm for a more robust and accurate solution for predicting the current distribution.

2. PROBLEM FORMULATION AND ALGORITHM DESCRIPTION

The current distribution $I(\omega)$ is calculated using Eq. [1], from the standard EMI/EMC measurement. Summarizing the above and according to the flowchart depicted in Figure 2, the first step in this methodology is to measure the radiated emissions of the cable on a fixed height above a standard aluminum ground plane according to MIL standard. From these experimental results, the current distribution is extracted and the implemented algorithm (DE) attempts to find an optimal model to match this trend, which comprises of the optimum values for the current distribution $I(\omega)$ capable to produce the same electric field emissions. Given the current distribution that have been calculated in the previous step, radiated emissions of the same system can be estimated, from Eq. [2], above any other ground (with known dielectric properties), placed at any height (optimized parameters of the extracted model) at any selected point.

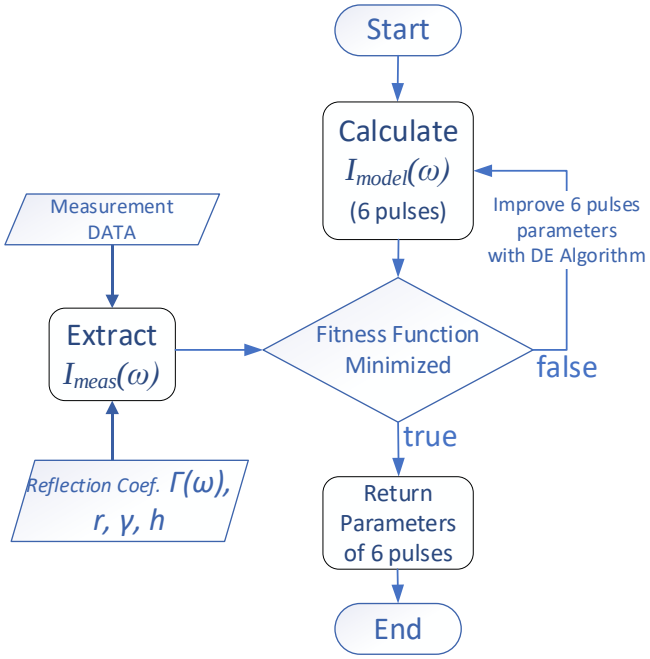

Figure 2. Flowchart of the proposed methodology employing the DE algorithm.

The iterative process across the whole frequency range of interest used in this methodology enables the prediction of electromagnetic emissions in any relative position and over any ground without any previous knowledge of the cable's characteristics. The proposed model provides a safe estimation for the maximum emission levels over a wide frequency span, Baklezos et al. (2016).

In Section 2, authors consider the current distribution which flows on the outer shield of the cable as a superposition of four pulses, one for each signal pair. A trapezoidal pulse can be fully

described by its amplitude A, pulse width τ, rise time τ_r, fall time τ_f and occurrence time t_p. The mathematical expression to describe the spectrum behavior of a trapezoidal pulse is:

$$I(\omega)_{multipletrap} = \sum_{i=1}^{N} A_i \frac{\tau_i}{T} \frac{sin\left(\frac{1}{2}n\omega_0\tau_i\right)}{\frac{1}{2}n\omega_0\tau_i} \cdot \frac{sin\left(\frac{1}{2}n\omega_0\tau_{r_i}\right)}{\frac{1}{2}n\omega_0\tau_{r_i}} \cdot e^{-jn\omega_0(\tau_i+\tau_{r_i})/2} \cdot e^{-j2\pi f t_{p_i}} \quad [1]$$

where $n = f \cdot T$ and $\omega_0 = 2\pi/T$, T is the period of the pulse in sec, and f is the frequency in Hz. In the case study of this work it is assumed that the pulse rise time equals the fall time $\tau_r = \tau_f$. Hence each of the six pulses can be described by 5 variables: the amplitude A, the pulse width τ, the rise time τ_r, the fall time τ_f and the occurrence time. Also, the TIA/EIA-644 (2012) standard defines the minimum acceptable value of output rise/fall time for all supported bitrates as equal to $0.26\ ns$.

$$\boldsymbol{E_\gamma = \left[sin\gamma \frac{1-e^{-jkL(1-cos\gamma)}}{jk(1-cos\gamma)} + sin\gamma \frac{e^{jkL(1+cos\gamma)}-1}{jk(1+cos\gamma)}\right] I(\omega) \frac{j\omega\mu e^{-jkr}}{4\pi r} \left[e^{jkhcos\theta} + \left(\frac{\sin\psi - \sqrt{\varepsilon_r - j\frac{\sigma}{\omega\varepsilon_0} - cos^2(\psi)}}{\sin\psi + \sqrt{\varepsilon_r - j\frac{\sigma}{\omega\varepsilon_0} - cos^2(\psi)}}\right) e^{-jkhcos\theta}\right]} \quad [2]$$

In the proposed scheme, for the whole frequency spectrum, a stochastic process is used (Differential Evolution) in order to match the extracted (Eq. [2]) current distribution with the modelled one, minimizing the fitness (objective) function of the Eq. [3]:

$$\boldsymbol{f_{fitness} = \sum_{f_i=1}^{f_n} (I_{model} - I_{measured})^2} \quad [3]$$

3. MEASUREMENTS &MODELING RESULTS

All measurements were conducted in the anechoic chamber of National Technical University of Athens. In order to perform SpW radiated emissions measurements, an arbitrary function generator has been used to provide pulse signal to the SpW/ LVDS driver and an EMI receiver with a bilog-antenna have been used for the electric field amplitude acquisition in the range of 30 MHz – 600 MHz.

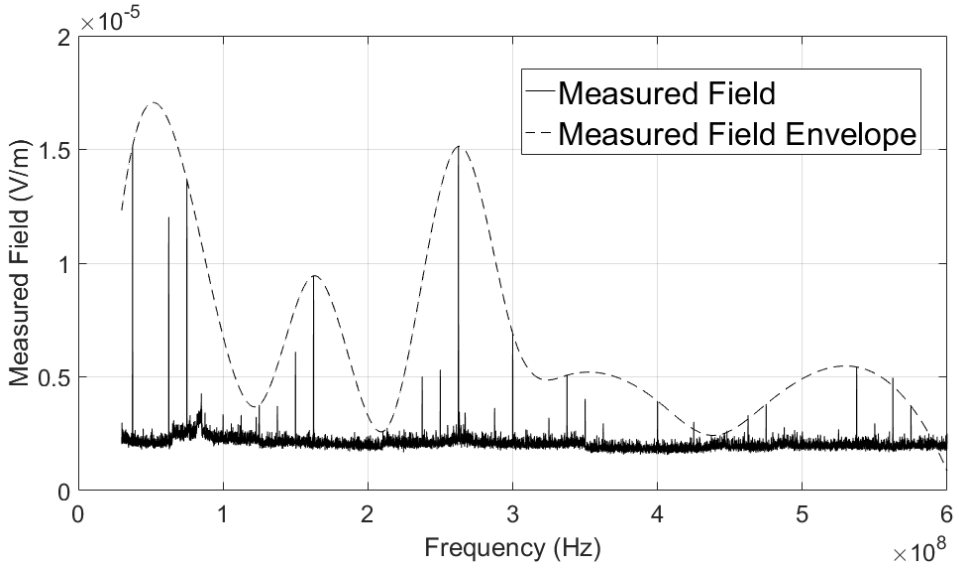

Figure 3. Measured cable's electric field emissions and the corresponding measured field envelope.

Figure 3 depicts the measured radiated electric field amplitude in V/m. In order to simplify the overall process and establish a worst-case scenario, instead of trying to model the actual measurements, authors opted to use the envelope of the measurements as the input to the algorithm. This envelope is also depicted in Figure 3.

With the aid of Eq. [1] the current is calculated for both cases, one for the measurement data and one for their envelope. Next, the current envelope distribution is fed to the algorithm. According to the previous analysis, the modified DE algorithm attempts to find the parameters of the 6 pulses which can reconstruct the current distribution with good agreement. This agreement is expressed by the minimization of the fitness function value (Eq. [3]). After evolving for 1200 generations a model is extracted with a cost function of $3.18 \times 10^{-10} \left(\frac{V}{m}\right)^2$ and a comparative figure with the modeled and measured electric field emissions is depicted in Figure 4.

Table 1. Pulses solution parameters – Extracted model.

# Pulse	Duration (s)	T-rise (s)	T-fall (s)	DC Amplitude (A)	Occurrence Time (s)
1	2.73e-8	7.53e-9	5.32e-9	0.2	5e-6
2	0	1.22e-7	1.63e-7	0.21	4.9e-6
3	9.97e-22	2.5e-6	7.3e-8	0.57	5e-6
4	4.35e-11	4.17e-9	9,44e-9	0,47	4,9e-06
5	6,2e-8	2,56e-9	2,03e-8	0,097	5e-6
6	1,06e-9	5,41e-9	9,02e-9	0,59	4,97e-6

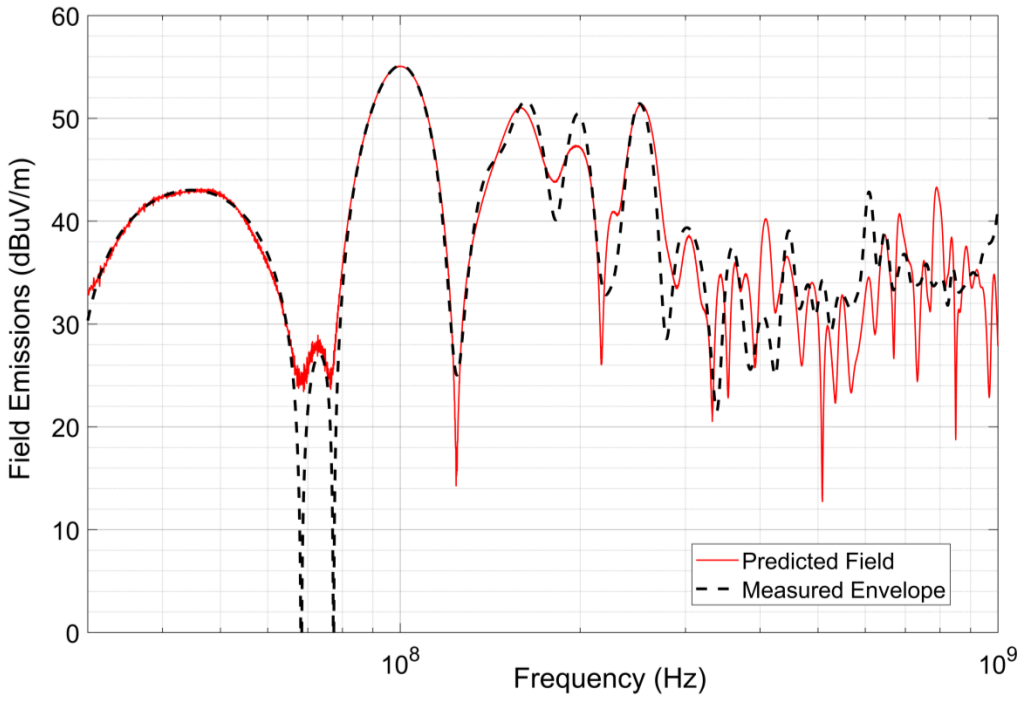

Figure 4. Estimated electric field using the modeled current compared to the measured field envelope.

4. CONCLUSION

In this work, authors applied and expanded a previously established methodology in the complex case of SpaceWire / LVDS digital system link. Said methodology claims that any shielded cable can be treated as a travelling wave antenna while the contributing phenomena can be decomposed in order to evaluate its impact on the cable's electromagnetic radiated emissions. In

this complex cable structure, authors express the current distribution flowing on the outer shield as a superposition of four pulses, each representing one of the four signal pairs. The expanded methodology differentiates from the previous work of the authors in the way the current distribution is described and in the way the spectrum is considered; instead of a bin by bin approach, a single model is extracted for the whole measured spectrum. This way a single inverse problem is solved, instead of numerous, employing Differential Evolution (MRL-DE) algorithm. Results showcase that the extracted model can accurately describe the phenomenon and provide safe estimation of the cable's radiated emissions. Future work may include the validation of this methodology with measurement from the TELETEL's iSHAFT simulator and include pulses occurrence time in the complete current distribution model. Moreover additional fitness functions shall be evaluated.

5. REFERENCES

Baklezos, A.T., C.D. Nikolopoulos, A. Katsouris, G. Koutantos, and C.N. Capsalis. 2016. Electromagnetic emission modeling in case of shielded cabling with respect to the ground dielectric properties. IEEE Transactions on Electromagnetic Compatibility, 58 (6): 1694–1700.

Dawar, D., and S.A. Ludwig. 2014. Differential evolution with dither and annealed scale factor. 2014 IEEE Symposium on Differential Evolution (SDE), Orlando, FL:1-8.

Kumar, P., and M. Pant. 2012. Enhanced mutation strategy for differential evolution. 2012 IEEE Congress on Evolutionary Computation, Brisbane, QLD: 1-6.

Nikolopoulos, C.D., A.T. Baklezos, and C.N. Capsalis. 2019a. A novel approach to radiated emissions modeling of low voltage differential signal on space wire cable employing differential evolution. 2019 Photonics & Electromagnetics Research Symposium - Spring (PIERS-Spring), Rome, Italy: 1929-1936, doi: 10.1109/PIERS-Spring46901.2019.9017308.

Nikolopoulos, C.D., A.T. Baklezos, S. Tsatalas, and C.N. Capsalis. 2019b. Verification of radiated emissions modeling for SpaceWire/LVDS links routed on CFRP ground. IEEE Transactions on Aerospace and Electronic Systems, doi: 10.1109/TAES.2019.2914540.

Storn, R., and K. Price. 1995. Differential evolution - a simple and efficient adaptive scheme for global optimization over continuous spaces. Berkley. TR-95-012.

TIA/EIA 644:2001 (R2012). 2012. Electrical characteristics of low voltage differential signaling (LVDS) interface circuits.

WEARABLE ANTENNA DESIGN FOR BODY-CENTRIC COMMUNICATIONS

Kapetanakis, T.N.[1], Nikolopoulos, C.D.[1], Petridis, K.[1], and Vardiambasis, I.O.[1] *

[1] Department of Electronic Engineering, Hellenic Mediterranean University
Chania, Crete, Greece

* ivardia@hmu.gr

1. INTRODUCTION

All communications within, upon, or around the human body, defined as body-centric communications, have assembled strong research interest and growing development over the last years, due to their vast newly developed applications, Hall and Hao (2006), Moradi et al. (2014), and Sun et al. (2020). Biomedical, healthcare, entertainment, sportive, identification, commercial as well as military systems and applications are continuously rising.

Antenna wearability, or in other words antenna flexibility, conformability, and stretchability in order to suit curvilinear surfaces and endure dynamic motions, consists a necessity for modern body-centric wireless communications, Kirtania et al. (2020). The development of flexible materials has opened the horizon for new antenna designs and innovative applications that were not possible with the old rigid structures. Thus, wearable antennas are rapidly becoming integrable parts of flexible electronic devices and sensors, smart watches, smart cards, future mobile phones, laptop and palmtop computers, telemedicine and healthcare systems, health-monitoring and clinic therapeutic devices, medical microwave radiometers, radio frequency identification tags, vehicular navigation systems, and the whole internet of things (IoT) industry, in order to seamlessly and invisibly communicate and exchange information and data between machines, technology and humans, Kirtania et al. (2020) and Sun et al. (2020).

Textile antennas are flexible, thin, robust, inexpensive, low profile, light weight, resistant to daily usage, durable to washing, and easily interconnected. They may be easily embedded into everyday everybody's clothing, serving all kind of body-centric, medical, military and commercial applications in the most promising way, as ideal smart interfaces for interaction between humans and technology, Los et al. (2016). Thus, the design and fabrication of wearable textile antennas is challenging, due to all previously mentioned advantages, along with their full capability to integrate and interconnect with microwave devices and radio frequency circuits, accomplishing very good results, Salvado et al. (2012) and Pavec et al. (2020).

The 2.45 GHz frequency, besides the UHF band, is extensively used for wearable Industrial Scientific & Medical (ISM) applications, according to several papers in the vast literature. For example, Wang et al. (2019) have proposed a wearable textile logo antenna for military applications, while Yadav et al. (2020), Ahmed et al. (2018), Bharadwaj et al. (2017), Singh et al. (2017), and Gao et al. (2011) have designed several flexible antennas for various on-body applications.

Various geometries and configurations of wearable and textile antennas have been introduced and implemented by many researchers in recent years. The relative literature is vast. To name a few, Ziai and Batchelor (2011) have proposed an RFID embroidered metamaterial antenna, Kiourti and Volakis (2015) have presented logo-shaped colorful textile antennas, Liu et al. (2016) have realized in textile technology a folded rectangular half-mode substrate-integrated cavity antenna, Hong et al. (2016) have implemented a textile antenna consisting of a circular ring slot on a substrate integrated waveguide cavity-feed structure, Amendola et al. (2016) have constructed a mixed embroidered-woven textile integrated waveguide antenna, Islam et al. (2018) have reported a dipole antenna on the Kapton polyimide substrate for flexible display devices, Maleky et al. (2018) have fabricated a

slotted patch antenna on e-textile created with sewed copper tape, Moradi et al. (2020) have fabricated an embroidered meander ring dipole antenna, Streemathy et al. (2020) have introduced cotton or denim substrates to slit loaded textile antennas, and Pavec et al. (2018), Pavec et al. (2020) have embroidered a fractal bowtie antenna.

Microstrip patch antennas, due to their compact size, light weight, low profile, planar configuration, easy fabrication, convenient modularization, high reliability, simple integrability with solid state devices, and low cost, are important in both theoretical research and engineering applications and widely used as transmitting antennas, despite their limited usable frequency bandwidth and low gain, Ansari et al. (2009) and Abdelgwad (2018).

In this work we present textile rectangular and triangular probe-fed microstrip patch antennas, designed for operation in the free 2.4 - 2.5 GHz ISM band, which are proposed to use as smart sensors or communication interfaces between interacting nodes and the wireless network for body-centric, IoT, RFID, or military applications. Their performance is investigated through measurements and simulations, while the effect of bending on their operation is examined and the specific absorption rate (SAR) values produced on a human chest model are related to the International Standards limits. Our prototypes exhibit attractive behavior, remarkable stability for different bending conditions, and extremely low SAR.

2. PATCH ANTENNA DESIGN

2.1. Rectangular patch

The geometry of the wearable under study antenna is shown in Figure 1, where a probe fed rectangular microstrip patch is illustrated as a structure consisting of 3 layers: 1) the upper-layer radiator which is a conductive rectangular patch of length L, width W and thickness t, 2) the middle-layer dielectric substrate of length $2L$, width $2W$ and thickness h, and 3) the bottom-layer ground plane of length $2L$, width $2W$ and thickness t.

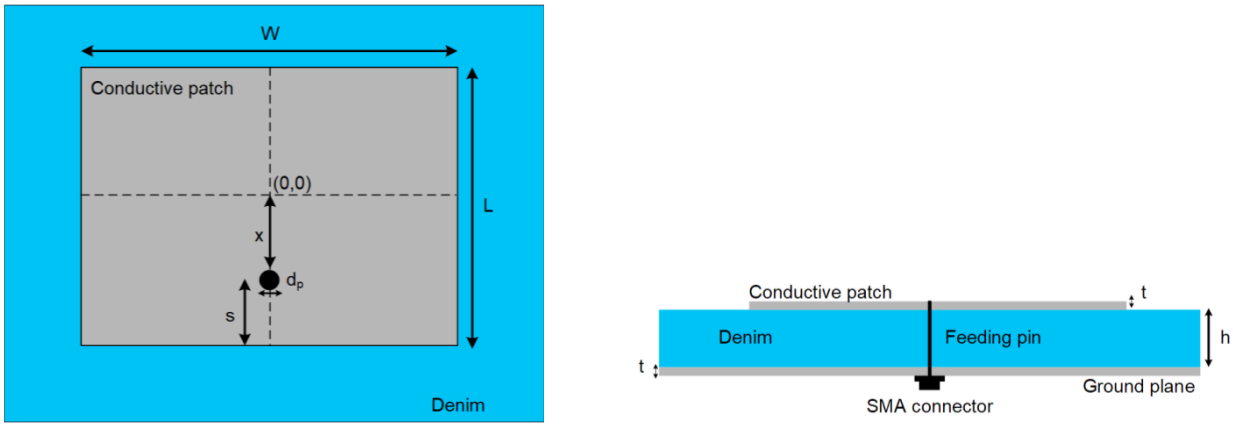

(a) **(b)**

Figure 1. Geometry of the probe fed rectangular microstrip patch antenna. (a) Top and (b) side view.

When the substrate and radiator materials are known, the design of textile patch antennas of rectangular shape for the 2.4-2.5 GHz ISM band is performed in the following 2 stages: (1) at the initialization stage, we use the transmission-line model, Balanis (2016), to determine the approximate dimensions W and L of the microstrip resonating at 2.45 GHz, and (2) at the optimization stage, we use a genetic algorithm to evolve the initial dimensions to their exact optimal values.

A practical patch width leading to good radiation efficiency is given by Eq. [1], Balanis (2016):

$$W = \frac{1}{2 f_r \sqrt{\mu_0 \varepsilon_0}} \sqrt{\frac{2}{\varepsilon_r + 1}} \qquad [1]$$

where ε_r is the dielectric constant of the substrate, f_r is the resonant frequency, and (ε_0, μ_0) are the dielectric permittivity and magnetic permeability of free space.

On the other hand, the actual patch length is given by Eq. [2], Balanis (2016):

$$L = \frac{1}{2 f_r \sqrt{\varepsilon_{reff}} \sqrt{\mu_0 \varepsilon_0}} - 2\Delta L \qquad [2]$$

where ε_{reff} is the effective dielectric constant of the microstrip antenna given by Eq. [3], ΔL is the extension of the length on each side of the patch given by Eq. [4], and h is the height of the substrate, Balanis (2016):

$$\varepsilon_{reff} = \frac{\varepsilon_r + 1}{2} + \frac{\varepsilon_r - 1}{2}\left[1 + 12\frac{h}{W}\right]^{-1/2} \qquad [3]$$

$$\frac{\Delta L}{h} = 0.412 \frac{(\varepsilon_{reff} + 0.3)\left(\frac{W}{h} + 0.264\right)}{(\varepsilon_{reff} - 0.258)\left(\frac{W}{h} + 0.8\right)} \qquad [4]$$

2.2. Triangular patch

The geometry of another wearable under study antenna is shown in Figure 2, where a probe fed triangular microstrip patch is illustrated as a structure consisting of 3 layers: 1) the upper-layer radiator which is a conductive isosceles triangular patch of height L, base length W and thickness t, 2) the middle-layer dielectric substrate of length $2L$, width $2W$ and thickness h, and 3) the bottom-layer ground plane of length $2L$, width $2W$ and thickness t.

In this case, at the initialization stage, we apply again the transmission-line model of the corresponding rectangular patch resonating at 2.45 GHz, to determine the approximate base length and height of the triangular microstrip as *W* and *L*, respectively. Then, at the optimization stage, we use a genetic algorithm to evolve the initial dimensions to their exact optimal values.

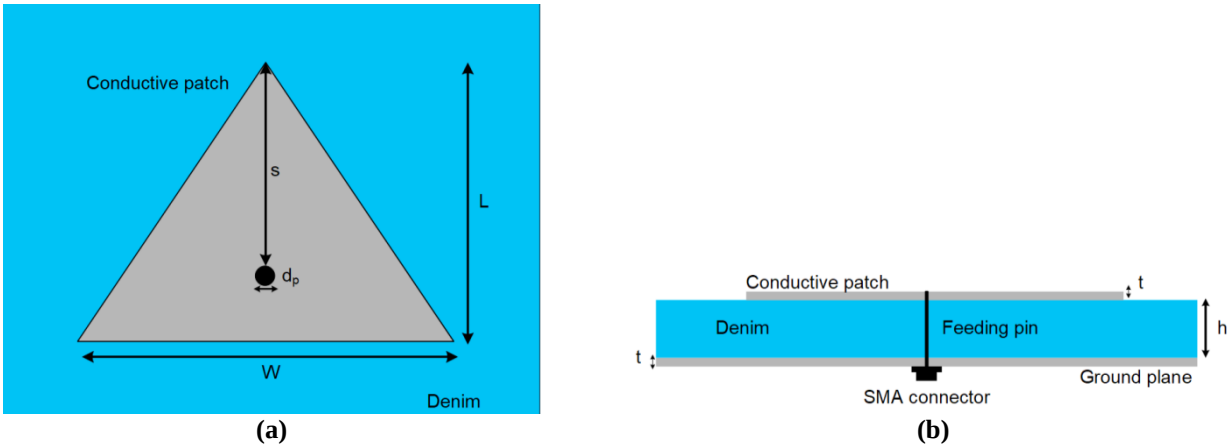

(a) **(b)**

Figure 2. Geometry of the probe fed triangular microstrip patch antenna. (a) Top and (b) side view.

2.3. Antenna feeding

The microstrip is fed by a coaxial line from underneath, as shown in Figures 1 and 2. The resonant frequency is not significantly affected by the feed location, but the input impedance is.

The distance x of the feed location from the rectangular microstrip center, affecting the antenna impedance, is approximately given by Eq. [5], Milligan (2005):

$$x = \frac{L}{2} - s = \frac{L}{\pi} \sin^{-1} \sqrt{\frac{R_{in}}{R_{ed}}} \qquad [5]$$

where R_{in} is the input resistance and R_{ed} is the input resistance at the edge. The impedance varies from 0 at the center to R_{ed} at the edge, so the feed location should be carefully determined.

In our case the feed-point is positioned in order to achieve the desirable input impedance $Z_{in} = 50 + j0\ \Omega$.

The microstrip can be fed by bringing the center conductor of a coaxial cable through a hole in the ground plane and substrate, and connecting it electrically to the designed patch feed-point.

In order to take into account the effect of the connector of Figure 3b to the overall performance of the antenna, a three-layered cylindrical structure is added to the simulation model as shown in Figure 3a, where regions (1), (2) and (3) correspond to the connector male pin, the dielectric spacing, and the outer conductor, respectively. Great care is taken during fabrication, because the antenna is very sensitive in terms of its feeding location, and a small deviation of the feeding point may result to mismatch.

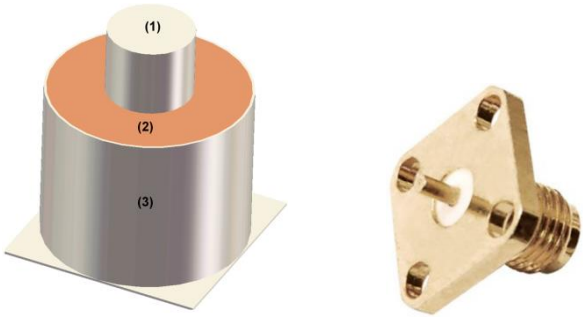

(a) **(b)**

Figure 3. The antenna feeding structure: (a) the simulation model and (b) the SMA connector.

2.4. Antenna optimization and fabrication

TABLE 1. GEOMETRICAL AND FABRICATION CHARACTERISTICS OF THE ANTENNA PROTOTYPES.

Patch Antenna	Approximate Prototypes	Optimized Prototype 1	Fabricated Prototype 1	Optimized Prototype 2	Fabricated Prototype 2
Microstrip Shape	Rectangular	Rectangular	Rectangular	Triangular	Triangular
Radiating Microstrip Material	Aaronia X-Dream+ Copper-Polyester Compound	Aaronia X-Dream+ Copper-Polyester Compound	Aaronia X-Dream+ Copper-Polyester Compound	Aaronia X-Dream+ Copper-Polyester Compound	Aaronia X-Dream+ Copper-Polyester Compound
Microstrip Thickness t (mm)	0.5	0.5	0.5	0.5	0.5
Damping (dB)	95	95	95	95	95
Microstrip Surface Resistivity (Ω/m^2)	$\leq 7.534 \times 10^{-3}$	$\leq 7.534 \times 10^{-3}$	$\leq 7.534 \times 10^{-3}$	$\leq 7.534 \times 10^{-3}$	$\leq 7.534 \times 10^{-3}$
Substrate Material	Denim	Denim	Denim	Denim	Denim
Substrate Thickness h (mm)	0.5	0.5	0.5	0.5	0.5
Substrate Dielectric Constant ε_r	1.578	1.578	1.578	1.578	1.578
Substrate Dielectric Losses $\tan\delta$	0.0231	0.0231	0.0231	0.0231	0.0231
Rectangular Length or Triangular Height L (mm)	48.42	46.68	47.0	54.17	55.1
Rectangular Width or Triangular Base Length W (mm)	53.52	50.00	49.5	59.51	59.0
Feeding point s (mm)	7.31	5.00	6.0	25.26	26.1
Ground Plane Length (mm)	96.84	93.36	155.0	108.33	168.0

Ground Plane Width (mm)	107.04	100.00	165.0	119.02	155.0

Giving the approximate values resulting from the previous equations, as initial estimations, to the optimization genetic algorithm of a commercial software package, we obtain for each under study antenna the final optimized geometrical characteristics, which we will use for simulation and fabrication.

The exact material characteristics of both patch prototypes, along with the corresponding approximate and optimized fabrication and geometrical characteristics, are given in Table 1. The parameters listed in the second, third and fifth columns of Table 1 are used for different simulations of our patch antennas, while the parameters of the third and fifth columns are used for the fabrication prototypes. The conductive fabric (Aaronia X-Dream+ copper-polyester compound) and the substrate (denim) were cut to the optimized dimensions using paper cutter. The strong and electrically conductive bond between the SMA connector and the prototype antenna was established by a two-part silver nanoparticles conductive epoxy adhesive (0.75mΩ/cm, @25°C) from BotFactory Inc.

Pictures of the fabricated prototypes, named as "Prototype 1" and "2" in Table 1, are presented in Figures 4 and 5. Because of the handmade fabrication of both patch prototypes, their dimensions (shown in the fourth and sixth columns of Table 1) are slightly different from their corresponding optimal values (shown in the third and fifth columns of Table 1). Consequently, in the following Section, we expect some justified differences between the measured and the simulated values of the microwave network and radiation antenna characteristics.

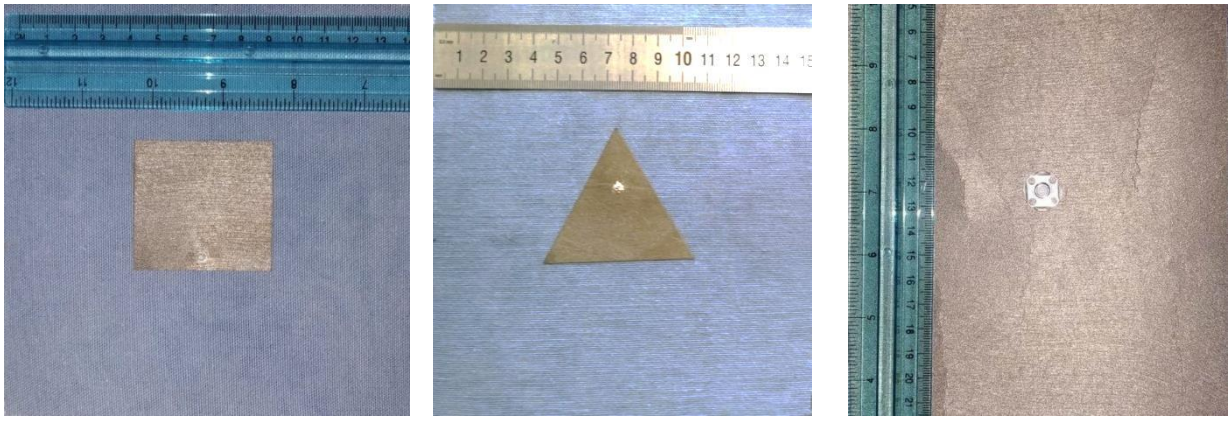

(a) **(b)** **(c)**

Figure 4. Pictures of the fabricated probe fed microstrip antenna prototypes. (a) Front view of the rectangular patch, (b) front view of the triangular patch, and (b) backside view (ground plane) of the antennas.

3. SIMULATIONS AND MEASUREMENTS

Several experimental and simulation tests have been performed in order to evaluate the performance of the antennas. Measurements were conducted by using an HP 8714ET analyzer, whereas simulations were performed by using commercial software packages.

3.1. Experimental and simulation results

The magnitude of the scattering network parameter S_{11}, corresponding to the reflection coefficient, is plotted in Figure 5. The rectangular prototype "1" and the triangular prototype "2" of Table 1, are considered in Figures 5a and 5b, respectively. Figure 5a presents three plots of S_{11} versus frequency for the rectangular patch: (i) simulated values in case of approximate patch dimensions given by the transmission-line method (TLM) (dotted line), (ii) simulated values in case of optimal patch dimensions given by the genetic algorithm (solid line), and (iii) measured values for the fabricated antenna operating in free space under the usual indoor environmental conditions temperature 21ºC and humidity 46% (bulleted line). Similarly, Figure 5b presents two plots of S_{11}

versus frequency for the triangular patch: (i) simulated values in case of optimal patch dimensions given by the genetic algorithm (solid line), and (ii) measured values for the fabricated antenna in free space under the usual indoor environmental conditions (bulleted line).

TABLE 2. SIMULATED AND MEASURED CHARACTERISTICS OF THE ANTENNA PROTOTYPES.

Antenna prototype	Approximate Rectangular Prototype Simulated	Optimized Rectangular Prototype Simulated	Fabricated Rectangular Prototype 1 Measured	Optimized Triangular Prototype Simulated	Fabricated Triangular Prototype 2 Measured
f_c (GHz)	2.326	2.449	2.426	2.448	2.430
S_{11} (dB) @ f_c	-25.54	-24.91	-14.96	-30.87	-14.28
VSWR @ f_c	1.111	1.120	1.435	1.059	1.478
f_1 (GHz)	2.321	2.424	2.387	2.425	2.370
f_2 (GHz)	2.331	2.474	2.466	2.474	2.490
-10 dB BW (MHz)	10	50	79	49	120

The measured bandwidth (when $S_{11} \le -10dB$) from Figure 5a is 79 MHz (=2.466-2.387 GHz), when the rectangular prototype is in free space, whereas it is only 50 MHz (=2.474-2.424 GHz) for the simulated optimized patch (solid curve). The -10dB bandwidth is further decreased to just 10 MHz in case of the simulated TLM patch (dotted curve). Although the measured and simulated bandwidth values for the rectangular prototype are remarkably different, the unlicensed 2.4-2.5 GHz ISM band is covered in both cases.

From Figure 5b, where the magnitude of S_{11} for the triangular patch is presented, the measured -10 dB bandwidth is 120 MHz (= 2.370-2.490 GHz), which is significantly greater compared to the bandwidths of all other prototypes of Table 1. Furthermore, both Figures 5a and 5b indicate a close agreement between measured and simulated results, especially regarding the operation frequency range.

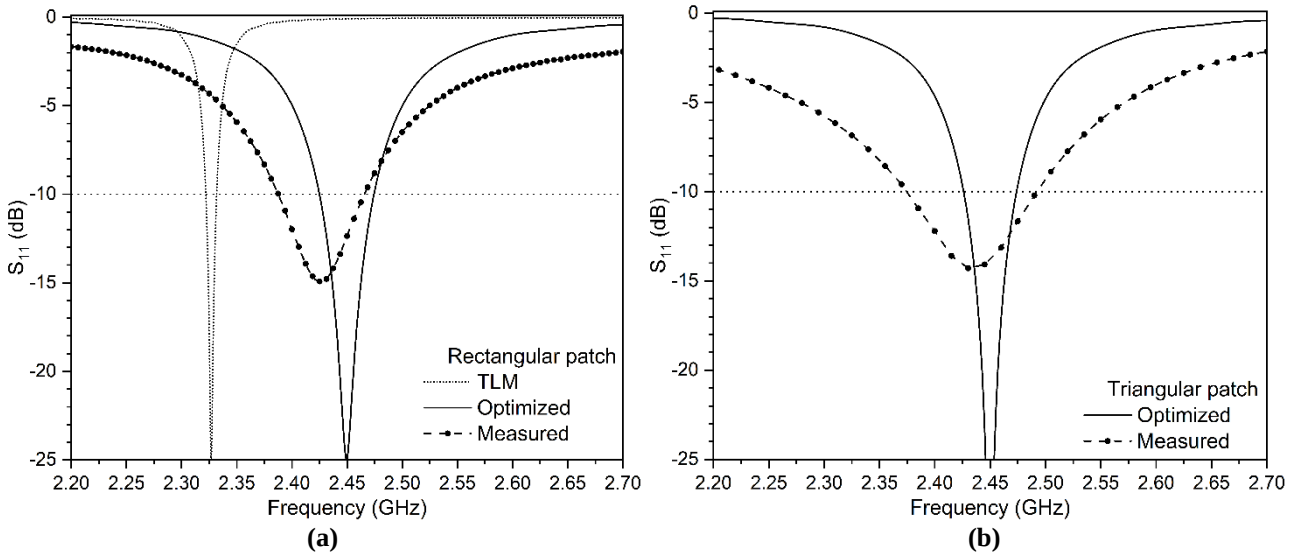

(a) **(b)**

Figure 5. Simulated and measured values of the S_{11} versus frequency, for the approximate and optimized prototypes in free space. (a) Rectangular patch and (b) triangular patch.

Tables 2 and 3 summarize the performance of the antennas presented in Table 1 and the bent antennas, respectively. The resonant frequency f_c, the magnitude of S_{11}, the voltage standing wave ratio (VSWR) at f_c, the -10 dB bandwidth, the lower and upper bandwidth limits (where

$S_{11} = -10dB$) f_1 and f_2 are listed in consecutive lines. All measurements have been conducted in free space when the prototypes are planar oriented.

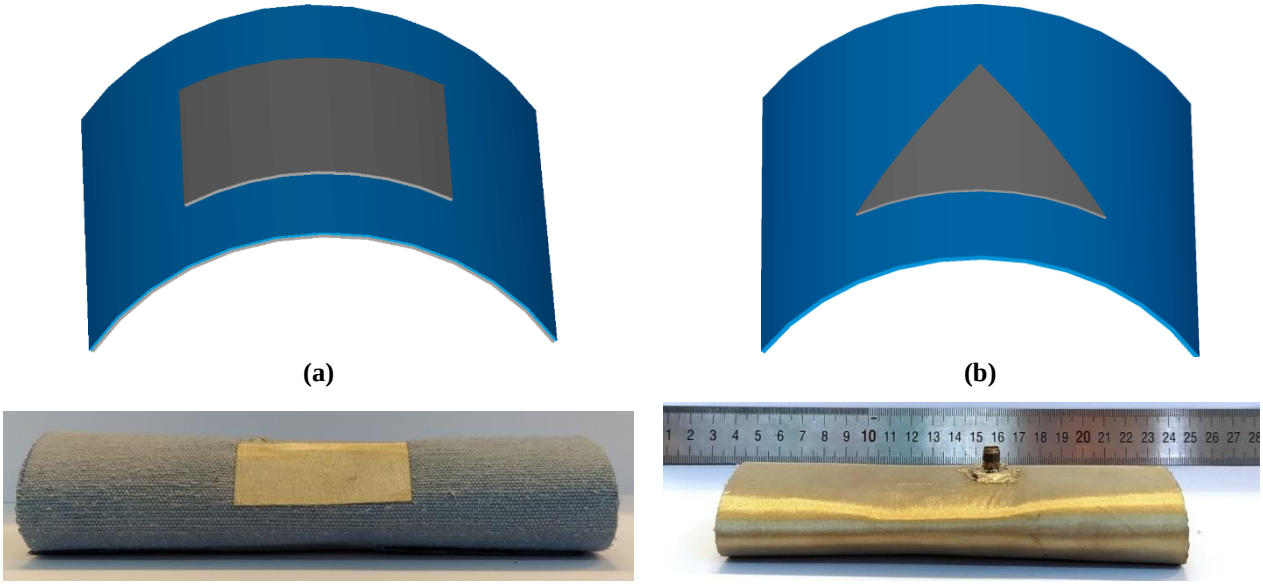

(a) (b) (c) (d)

Figure 6. Geometry and pictures of the bent prototypes, when the antenna is mounted on a dielectric cylindrical tube. (a) Geometrical sketch of the rectangular patch, (b) geometrical sketch of the triangular patch, (c)-(d) pictures of the bent rectangular structure.

Additionally, the antenna behavior has been investigated under bending conditions, as shown in Figure 6. The antenna was mounted on a cylindrical non-conductive dielectric tube with diameter $d = 70, 90, 100, 130\,\text{mm}$. The magnitude of S_{11} is plotted in Figure 7, when the antenna is bent. The bulleted curves are included for reference, as they are identical to the corresponding curves of Figure 5, depicting the measured results for S_{11} (dB) when the planar (not bent) antenna is in free space.

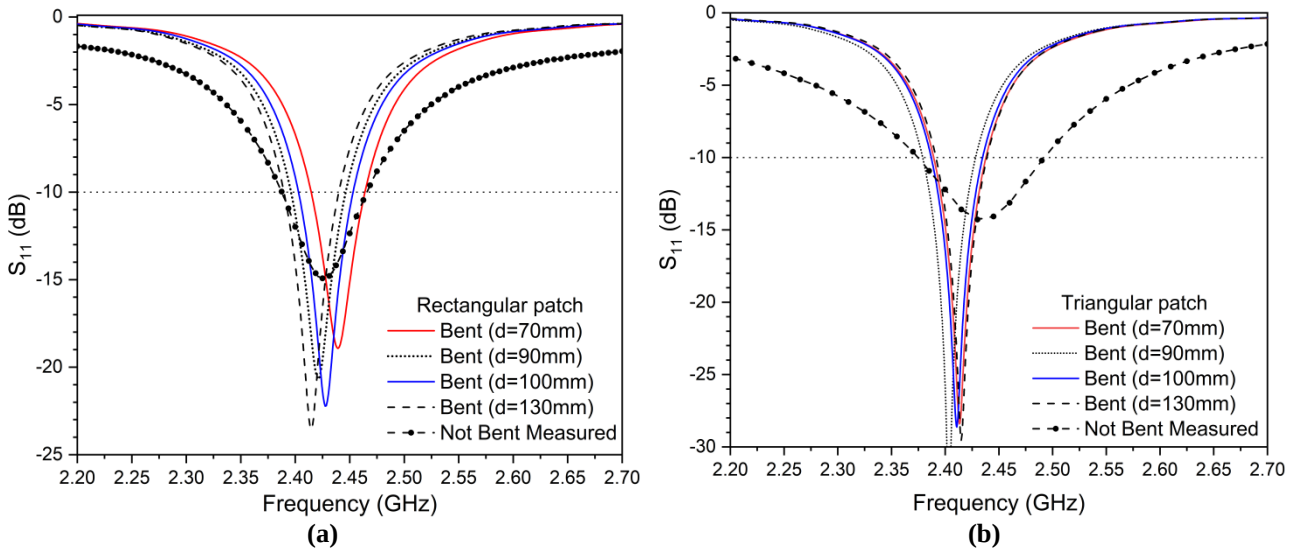

(a) (b)

Figure 7. Simulated and measured values of the S_{11} versus frequency, for the prototypes under different bending conditions, as shown in Figure 3. (a) Rectangular patch and (b) triangular patch.

According to Figures 7a and 7b, the resonant frequency f_c of the bent antennas is shifted in comparison to the planar ones, but the bandwidth is remarkably stable in all bending conditions. Regardless the tube diameter, the operational bandwidth is in the range 49 – 51 MHz for the rectangular patch, or in the range 47 – 50 MHz for the triangular one, as Figure 7 and Table 3

denote. However, the aforementioned shift of f_c does not affect its operation under bending, since the -10 dB antenna bandwidth falls within the unlicensed 2.4-2.5 GHz ISM band in all cases.

TABLE 3. SIMULATED AND MEASURED CHARACTERISTICS OF THE BENT ANTENNA PROTOTYPES.

	Bent Rectangular Patch Simulated				Bent Triangular Patch Simulated			
Antenna Prototype	**d=70mm**	**d=90mm**	**d=100mm**	**d=130mm**	**d=70mm**	**d=90mm**	**d=100mm**	**d=130mm**
f_c (GHz)	2.439	2.421	2.427	2.413	2.412	2.402	2.410	2.414
S_{11} (dB) @ f_c	-18.92	-20.66	-22.22	-23.43	-28.20	-33.46	-28.62	-29.54
VSWR @ f_c	1.255	1.204	1.167	1.144	1.080	1.043	1.077	1.069
f_1 (GHz)	2.413	2.397	2.402	2.389	2.389	2.378	2.386	2.391
f_2 (GHz)	2.463	2.446	2.453	2.440	2.437	2.428	2.434	2.438
-10 dB BW (MHz)	50	49	51	51	48	50	48	47

3.2. Radiation Characteristics

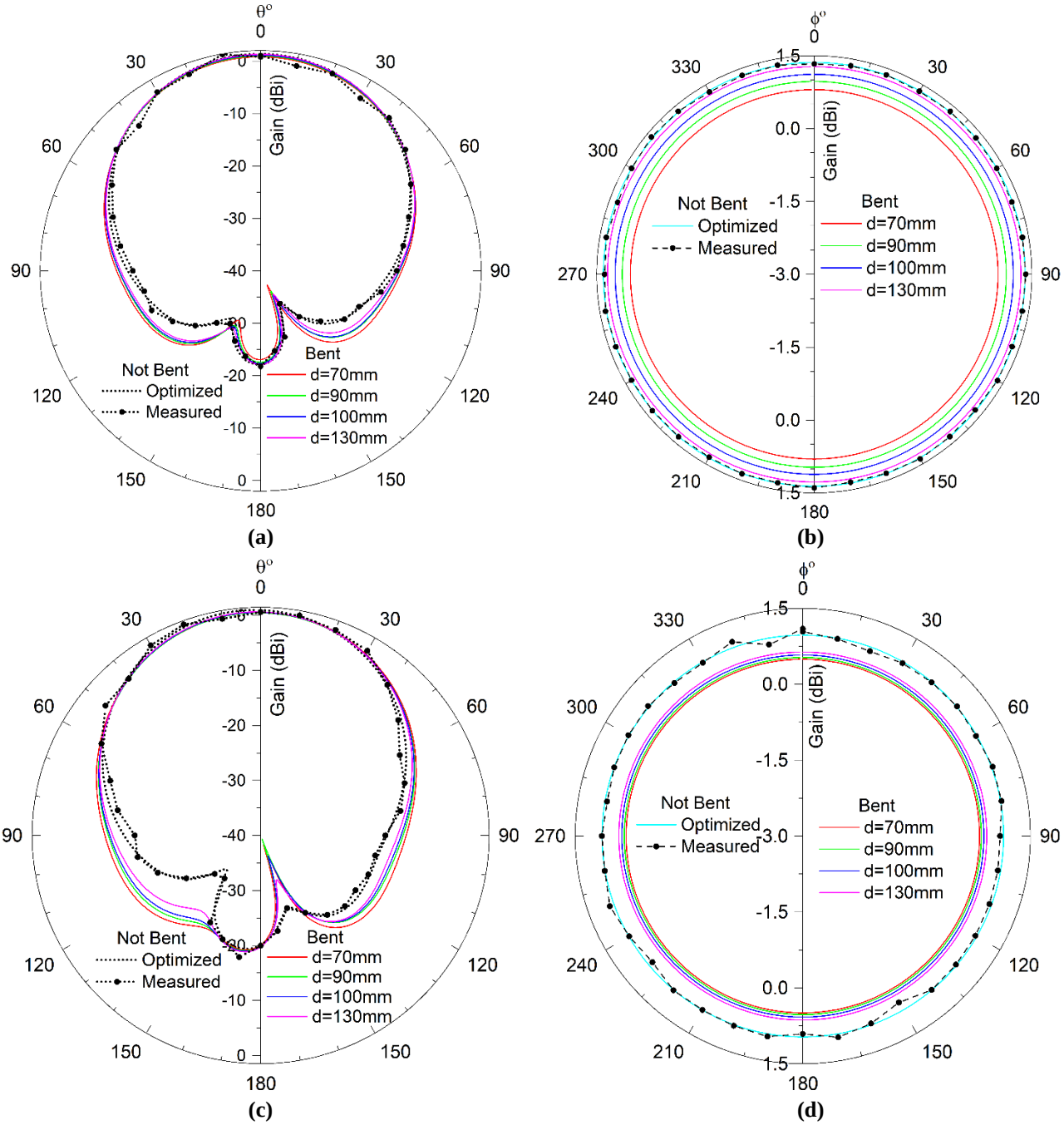

Figure 8. Simulated (solid curves) and measured (circles) free-space radiation patterns for the prototypes under different bending conditions. (a) θ-plane for the rectangular patch, (b) φ-plane for the rectangular patch, (c) for θ-plane for the triangular patch, and (d) φ-plane for the triangular patch.

Figure 8 shows the simulations and measurements of the patch radiation patterns, in order to reveal the radiation characteristics of the developed prototypes, under different bending conditions. The solid colored lines correspond to the simulated results of the bent structures, when the antenna is mounted on a dielectric cylindrical tube with diameter d=70, 90, 100 and 130 mm, while the dotted and bulleted lines depict the simulated and measured results, respectively, from the planar (not bent) patch antenna. All patterns of Fig. 8 refer to the resonant frequencies given at the first row of Tables 2 and 3. The measurements were conducted with the MegiQ RMS-0660 antenna radiation measurement system. Fig. 8 demonstrates good agreement between measured and simulated results, while the bending conditions slightly affect the prototype antennas' radiation characteristics. The φ-plane simulated and measured radiation patterns exhibit an omnidirectional dipole-like behavior, while the θ-plane simulated and measured patterns exhibit very low radiation for $\theta > 90^o$, due to the ground plane presence at $\theta = 90^o$. The gain of all rectangular antennas is in the range 0.78 – 1.56 dBi in the θ-plane and 0.80 – 1.37 dBi in the φ-plane, while the gain of all triangular antennas is in the range 0.43 – 1.03 dBi in the θ-plane and 0.50 – 1.04 dBi in the φ-plane.

3.3. SAR estimation

Finally we evaluate the SAR produced by the proposed antennas, which are intended for wearable applications. The prototypes are designed to operate in proximity to the human chest, which is modeled by a four-layer rectangular model, Anbalagan et al. (2020), as illustrated in Figure 9. The properties of the four tissue layers constituting the model are given in Table 4. Between the antenna and the human skin in Figure 9, a cotton ($\varepsilon_r = 1.6$) t-shirt of thickness 1.5 mm, and an air gap ($\varepsilon_r = 1$) of 1 mm are considered. The whole body SAR and the maximum SAR averaged over a volume of 10 g tissue have been calculated according to the respective International Standards, IEC/IEEE International Standard (2017) and IEEE-SA Standards Board (2002). The antenna was placed in contact with the cotton t-shirt, at the center of the model shown in Figure 9, and the input power to the antenna was 0.5 W (rms value) at 2.45 GHz.

TABLE 4. TISSUE PROPERTIES AND THICKNESSES AT 2.45 GHZ.

Tissue type	σ (S/m)	ε_r	Density (kg/m^3)	Thickness (mm)
Dry skin	1.460	38.0	1100	1.5
Fat	0.268	10.8	900	13
Muscle	1.740	52.7	1080	20
Cortical bone	0.394	11.4	2000	3.5

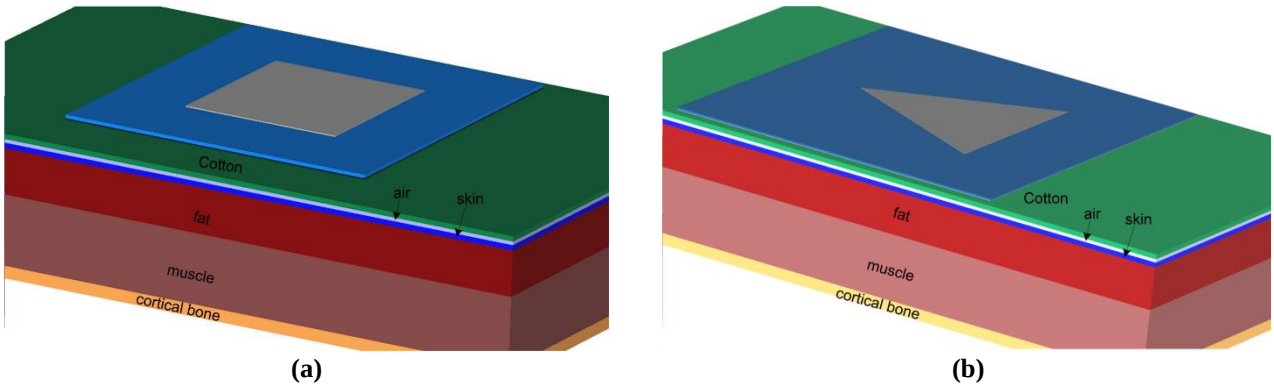

(a) **(b)**

Figure 9. Layered human's chest model with length and width equal to 200 and 120 mm, respectively. The various layers are given in Table 4.

The obtained values for the whole body SAR and the peak SAR over 10 g tissue were equal to 1.77×10^{-6} W/kg and 1.33×10^{-5} W/kg, respectively, for the rectangular patch of Figure 9a, and equal to 0.96×10^{-6} W/kg and 1.07×10^{-5} W/kg, respectively, for the triangular patch of Figure 9b, which are far below the valid International Standards limits 0.08 W/kg (whole body SAR) and 2 W/kg (max SAR over 10g). The extremely low SAR values of our prototypes are justified because of the presence of the ground plane between the antenna and the cotton t-shirt.

4. CONCLUSION

Textile microstrip patch antennas, which may be easily attached to clothing, have been presented in this paper. Two wearable patch antenna prototypes of rectangular or triangular shape have been designed and fabricated. The rectangular and triangular conducting patches have been pasted on a denim substrate by using a conductive adhesive layer.

Simulations and measurements have been conducted to evaluate the performance of the patches, which were designed to cover the unlicensed 2.4-2.5 GHz ISM band. This goal was achieved in all examined cases. Each antenna's bandwidth is extracted by S_{11} simulations and measurements. According to the results, our antennas cover with remarkable stability the unlicensed 2.45 GHz ISM band in all cases. Nevertheless the fabricated prototypes exhibit considerable enhanced -10 dB bandwidth compared to the simulated antennas. When the antennas are bent upon curved surfaces, the resonant frequency and the -10 dB bandwidth show remarkable stability, although the antenna gain is reduced with increasing surface curvature.

The radiation characteristics of the proposed antennas are slightly affected by the bending conditions, while the calculated SAR values on a human chest's rectangular layered model are thousands of times below the International Standards limits.

5. ACKNOWLEDGEMENT

This research is co-financed by Greece and the European Union (European Social Fund - ESF) through the Operational Program "Human Resources Development, Education and Lifelong Learning 2014-2020" in the context of the project "Smart microwave nanomaterial structures with applications in bodycentric communications and the Internet of Things (MIS 5048187)".

6. REFERENCES

Abdelgwad, A.H. 2018. Microstrip patch antenna enhancement techniques. International Journal of Electronics and Communication Engineering, 12 (10): 703-710.

Ahmed, M.I., M.F. Ahmed, and A.-E.H. Shaalan. 2018. SAR calculations of novel textile dual-layer UWB lotus antenna for astronauts spacesuit. Progress In Electromagnetic Research C, 82: 135–144.

Amendola, S., G. Bovesecchi, A. Palombi, P. Coppa, and G. Marrocco. 2016. Design, calibration and experimentation of an epidermal RFID sensor for remote temperature monitoring. IEEE Sensors Journal, 16: 7250–7257.

Anbalagan, A., E.F. Sundarsingh, and V.S. Ramalingam. 2020. Design and experimental evaluation of a novel on-body textile antenna for unicat applications. Microwave and Optical Technology Letters, 62: 789-799.

Ansari, J.A., P. Singh, and N.P. Yadav. 2009. Analysis of wideband multilayer patch antenna with two parasitic elements. Microwave and Optical Technology Letters, 51 (6): 1397-1401.

Balanis, C.A. 2016. Antenna Theory: Analysis and Design, 4th Edition. New Jersey, USA: Wiley.

Bharadwaj, R., S. Swaisaenyakorn, C.G. Parini, J.C. Batchelor, and A. Alomainy. 2017. Impulse radio ultra-wideband communications for localization and tracking of human body and limbs

movement for healthcare applications. IEEE Transactions on Antennas and Propagation, 65: 7298-7309.

Corchia, L., G. Monti, and L. Tarricone. 2019. Wearable antennas: Nontextile versus fully textile solutions. IEEE Antennas & Propagation Magazine, 61: 71–83.

Gao, Y., Y. Zheng, Y., S. Diao, W.-D. Toh, C.-W. Ang, M. Je, and C.-H. Heng. 2011. Low-power ultrawideband wireless telemetry transceiver for medical sensor applications. IEEE Transactions on Biomedical Engineering, 58: 768–772.

Hall, P. and Y. Hao. 2006. Antennas and Radio Propagation for Body-Centric Wireless Communications. London, U.K.: Artech House.

Hong, Y., J. Tak, and J. Choi. 2016. An all-textile SIW cavity-backed circular ring-slot antenna for WBAN applications. IEEE Antennas & Wireless Propagation Letters, 15: 1995-1999.

IEC/IEEE International Standard. 2017. Determining the peak spatial-average specific absorption rate (SAR) in the human body from wireless communications devices, 30 MHz to 6 GHz - Part 1: General requirements for using the finite-difference time-domain (FDTD) method for SAR calculations. *IEC/IEEE 62704-1/2017*: 1-86.

IEEE-SA Standards Board. 2002. IEEE recommended practice for measurements and computations of radio frequency electromagnetic fields with respect to human exposure to such fields, 100 kHz 300 GHz. IEEE Std C95.3-2002 (Revision of IEEE Std C95.3-1991), 4: 1-126.

Islam, M., T. Alam, I. Yahya, and M. Cho. 2018. Flexible radio-frequency identification (RFID) tag antenna for sensor applications. Sensors, 18, 4212: 1-9.

Kiourti, A. and J.L. Volakis. 2015. Colorful textile antennas integrated into embroidered logos. Journal of Sensor and Actuator Networks, 4: 371-377.

Kirtania, S.G., A.W. Elger, R. Hasan, A. Wisniewska, K. Sekhar, T. Karacolak, and P.K. Sekhar. 2020. Flexible antennas: A review. Micromachines, 11, 847: 1–43.

Liu, F.X., Z. Xu, D.C. Ranasinghe, and C. Fumeaux. 2016. Textile folded half-mode substrate-integrated cavity antenna. IEEE Antennas & Wireless Propagation Lettters, 15: 1693-1697.

Loss, C., R. Goncalves, C. Lopes, P. Pinho, and R. Salvado. 2016. Smart coat with a fully-embedded textile antenna for IoT applications. Sensors, 16: 938.

Maleky, O.E., F.B. Abdelouahab, M. Essaaidi, and M. Ali Ennasar. 2018. Design of simple printed dipole antenna on flexible substrate for UHF band. Procedia Manufacturing, 22: 428–435.

Milligan, T.A. 2005. Modern Antenna Design, 2nd Edition. New Jersey, USA: Wiley.

Moradi, B., R. Fernandez-Garcia, and I. Gil. 2020. Wearable high-performance meander ring dipole antenna for electronic-textile applications. The Journal of the Textile Institute, 111: 178-182.

Moradi, E., K. Koski, T. Bjorninen, L. Sydanheimo, J.M. Rabaey, J.M. Carmena, Y. Rahmat-Samii, and L. Ukkonen. 2014. Miniature implantable and wearable on-body antennas: Towards the new era of wireless body-centric systems. IEEE Antennas and Propagation Magazine, 56 (1): 271-291.

Pavec, M., J. Navratil, R. Soukup, and A. Hamacek. 2018. A bowtie antenna prepared by aerosol jet and embroidering technology. 41st International Spring Seminar on Electronics Technology (ISSE), Zlatibor: 1-4.

Pavec, M., T.N. Kapetanakis, M.P. Ioannidou, C.D. Nikolopoulos, A.T. Baklezos, R. Soukup, T. Blecha, A. Hamacek, and I.O. Vardiambasis. 2020. Implementation of an all-textile bow-tie antenna for the 868 MHz ISM band. 2020 International Symposium on Electromagnetic Compatibility (EMC Europe 2020), Rome, Italy: 1-3.

Salvado, R., C. Loss, R. Concalves, and P. Pinho. 2012. Textile materials for the design of wearable antennas: A survey. Sensors, 12: 15841-15857.

Singh, V.K., S. Dhupkariya, and N. Bangari. 2017. Wearable ultra wide dual band flexible textile antenna for WiMax/WLAN application. Wireless Personal Communications, 95: 1075-1086.

Sreemathy, R., S. Hake, S. Sulakhe, and S. Behera. 2020. Slit loaded textile microstrip antennas. IETE Journal of Research.

Sun, H., Y. Hu, R. Ren, L. Zhao, and F. Li. 2020. Design of pattern-reconfigurable wearable antennas for body-centric communications. IEEE Antennas and Wireless Propagation Letters, 19 (8): 1385-1389.

Tsolis, A., W.G. Whittow, A.A. Alexandridis, and J.C. Vardaxoglou. 2014. Embroidery and related manufacturing techniques for wearable antennas: Challenges and opportunities. Electronics, 3: 314-338.

Wang, W., C. Ma, X. Zhang, J. Shen, N. Hanagata, J. Huangfu, and M. Xu. 2019. High-performance printable 2.4 GHz graphene-based antenna using water-transferring technology. Science and technology of Advanced Materials, 20: 870–875.

Yadav, A., V. Kumar Singh, A. Kumar Bhoi, G. Marques, B. Garcia-Zapirain, and I. de la Torre Díez. 2020. Wireless body area networks: UWB wearable textile antenna for telemedicine and mobile health systems. Micromachines, 11(6), 558: 1-22.

Ziai, M.A. and J.C. Batchelor. 2011. Temporary on-skin passive UHF RFID transfer tag. IEEE Transactions on Antennas and Propagation, 59: 3565–3571.

DEVELOPMENT OF ALL-TEXTILE ANTENNAS FOR THE ISM BAND

Pavec, M.[1], Kapetanakis, T.N.[2], Nikolopoulos, C.D.[2], Baklezos, A.T.[2], Moravcova, D.[1], Soukup, R.[1], Blecha, T.[1], Hamacek, A.[1], Stratakis, D.[3], Chatzakis, J.[2], Ioannidou, M.P.[4], and Vardiambasis, I.O.[2] *

[1] Department of Technologies & Measurement, University of West Bohemia
Pilsen, Czech Republic

[2] Department of Electronic Engineering, Hellenic Mediterranean University
Chania, Crete, Greece

[3] Department of Electrical & Computer Engineering, Hellenic Mediterranean University
Heraklion, Crete, Greece

[4] Department of Information & Electronic Engineering, International Hellenic University
Thessaloniki, Greece

* ivardia@hmu.gr

1. INTRODUCTION

Wearable antennas have mustered strong interest over the last years, because of their vast applications in portable wireless communication and sensing, healthcare and telemedicine, smart watches and future mobile phones, radio frequency identification and navigation, and Internet of Things (IoT). Textile antennas, due to their low cost, light weight and flexibility, may be embedded into everyday clothing, constituting the ideal smart interface for interaction between humans and technology, Los et al. (2016) and Pavec et al. (2020). Embroidery is a modern advanced technique, which allows textile substrates to obtain conductive electrical pathways, being characterized by specific advantages, such as repeatability, mass garment production and customized designs' implementation, Tsolis et al. (2014) and Pavec et al. (2020).

It is challenging to design and fabricate wearable textile antennas, since they have to be thin, inexpensive, robust, resistant to usage and washing, easily embroidered and interconnected, and capable of integration with radio frequency circuits, in order to accomplish good results, Salvado et al. (2012) and Pavec et al. (2020).

Various configurations have been introduced by several researchers in the literature for wearable antenna implementation. Representative recent works include the logo-shaped colorful textile antennas based on automated embroidery of conductive e-threads, Kiourti and Volakis (2015), a folded rectangular half-mode substrate-integrated cavity antenna realized in textile technology using computerized embroidery, Liu et al. (2016), a textile antenna consisting of a substrate integrated waveguide cavity-feed structure and a circular ring slot, Hong et al. (2016), an embroidered meander ring dipole antenna, Moradi et al. (2020), and slit loaded textile antennas with cotton or denim substrates, Streemathy et al. (2020).

In this work we present a textile bow-tie antenna based on the Sierpinski triangle geometry. The antenna is designed for operation in the free 863-870 MHz Industrial Scientific and Medical (ISM) band and may be used for IoT applications as a smart interface for the interaction between each node and the network. It exhibits attractive characteristics such as wide bandwidth (BW) and relatively stable radiation patterns for different bending conditions.

2. ANTENNA DESIGN AND FABRICATION

The antenna presented herein has a geometry based on the Sierpinski triangle, which is a triangulate fractal shape, constructed by subtracting a central inverted equilateral triangle from an

equilateral main triangular shape and by repeating the same procedure on the remaining triangles, Pavec et al. (2020) and Baliarda et al. (1998). The area removed in each iteration is given by $A_N = \frac{1}{3}\sum_{i=1}^{N}(3/4)^i$, as in Chowdary et al. (2015), where N stands for the number of iterations.

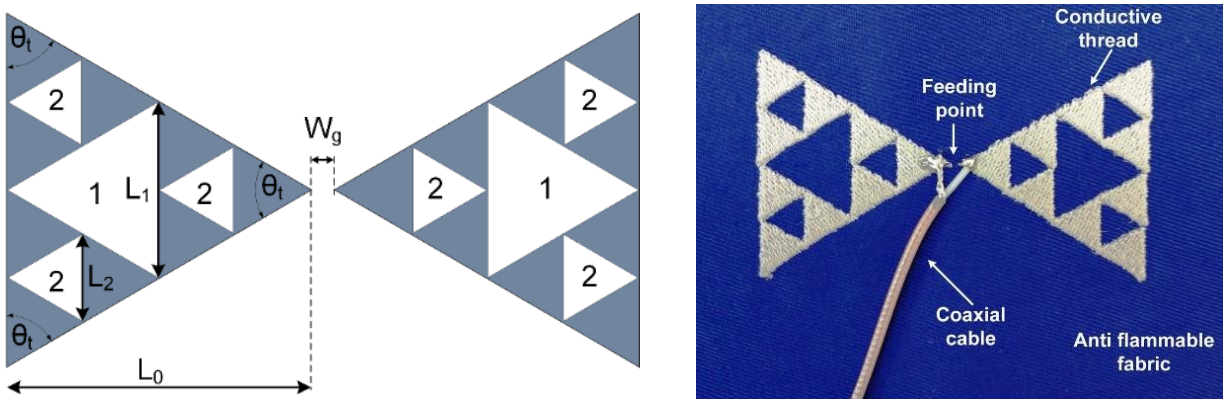

(a) **(b)**

Figure 1. (a) Geometric configuration of the bow-tie antenna. (b) Bow-tie antenna prototype, Pavec et al. (2020).

Figure 1 depicts the geometry of the bow-tie antenna implemented in this paper. It consists of two back to back equilateral triangles fed at the center point between the two triangular arms. Two iterations have been applied and the parameters that appear in Figure 1 are as follows: the half-length of the structure is $L_0 = 5\,\text{cm}$, the side of each triangle after the first and the second iteration is $L_1 = 2.3\,\text{cm}$ and $L_2 = 1\,\text{cm}$, respectively, and the gap between the two triangular arms is $W_g = 2.1$ mm, while all triangles are equilateral ($\theta_t = 60^\circ$).

The pattern of Figure 1 was embroidered on a Dupont Nomex meta-aramid fabric, which is a flame-resistant textile commonly used for petro-chemical protective suits, Pavec et al. (2018). It is composed of 93% Nomex, 5% Kevlar and 2% carbon. The electrical properties of this special substrate are: relative dielectric constant $\varepsilon_r = 2.5$, surface resistivity per square 10^{12} Ω and loss tangent $\tan\delta = 0.006$. The silver hybrid conductive sewing thread (Clevertex), used for the embroidery, is composed of polyester (PES) multifilament and four Ag plated Cu microwires. The linear resistance of the thread is 6.5 Ω/m (nominal value @ 20°C). The sewing machine Bernina QE750, equipped with a special module for embroidering, was used for the fabrication of the bow-tie antenna prototype shown in Figure 1.

3. MEASUREMENTS AND PERFORMANCE EVALUATION

The fabricated bow-tie antenna has been tested experimentally. As a first step, the measured Return Loss (RL) $|S_{11}|$, is plotted in Figure 2. Three cases are considered in Figure 2: (i) with solid curve for the antenna in free space under usual indoor environmental conditions (temperature 19°C, humidity 67%), (ii) with dashed curve for the antenna mounted on human's chest with a thin t-shirt in between, and (iii) with dotted curve for the antenna mounted on a planar conductive (copper foil) substrate. Figure 2 suggests that the measured RL, with the antenna in free space, is below -10dB in the range 844-1006 MHz, i.e., the -10dB RL bandwidth is 162 MHz and covers the unlicensed 863-870 MHz ISM band. The main bandwidth around the aforementioned ISM band is increased to 180 MHz when the antenna is body mounted, whereas it is further increased to 330 MHz for the antenna mounted on a copper foil. Moreover, Figure 3 verifies the multiband behaviour of the mounted antenna, which is a well known feature of the fractal shaped Sierpinski antenna reported by several researchers, Baliarda et al. (1998), Chowdary et al. (2015), and Kaur et al. (2011).

Figure 3 presents the measured RL, when the bow-tie antenna is bent and mounted on a dielectric, cylindrical tube. The fabric is either mounted directly on the tube (considering two different tube diameters with $d = 13$ cm and $d = 10$ cm), or attached on the tube of diameter $d = 13$ cm with a copper foil in between. Figure 3 reveals that the -10dB RL bandwidth of the bent antenna covers the unlicensed 868 MHz ISM band in all three cases considered. The narrowest bandwidth 183 MHz (in the range 769-952 MHz) is observed when the antenna is mounted directly on the dielectric cylinder with $d = 10$ cm (dashed curve). The bandwidth increases to 255 MHz when the curvature of the tube decreases (solid curve, $d = 13$ cm), and reaches the value of 385 MHz when a copper foil is in between the fabric and the dielectric tube (dotted curve).

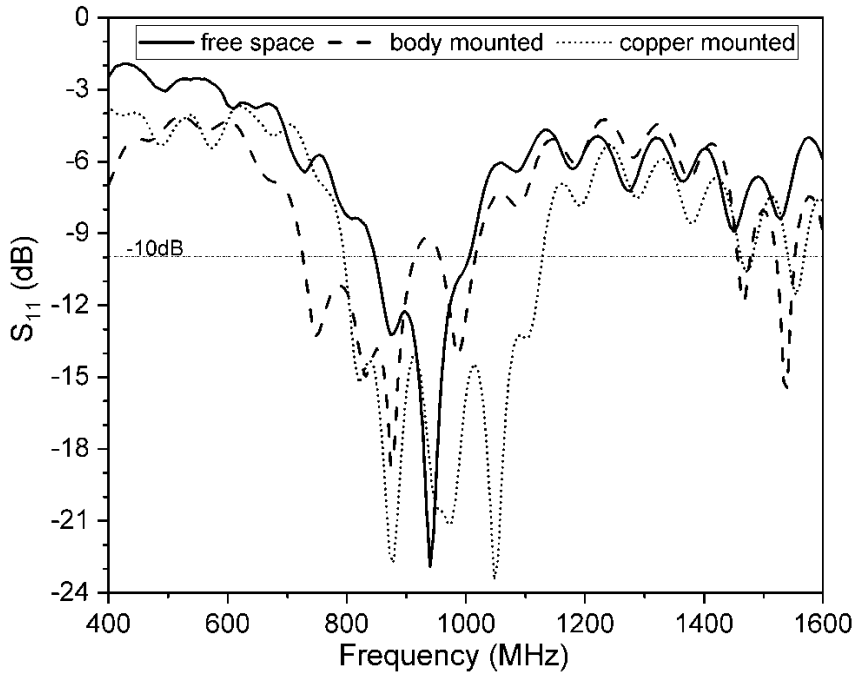

Figure 2. S_{11} versus frequency for the fabricated bow-tie antenna, Pavec et al. (2020).

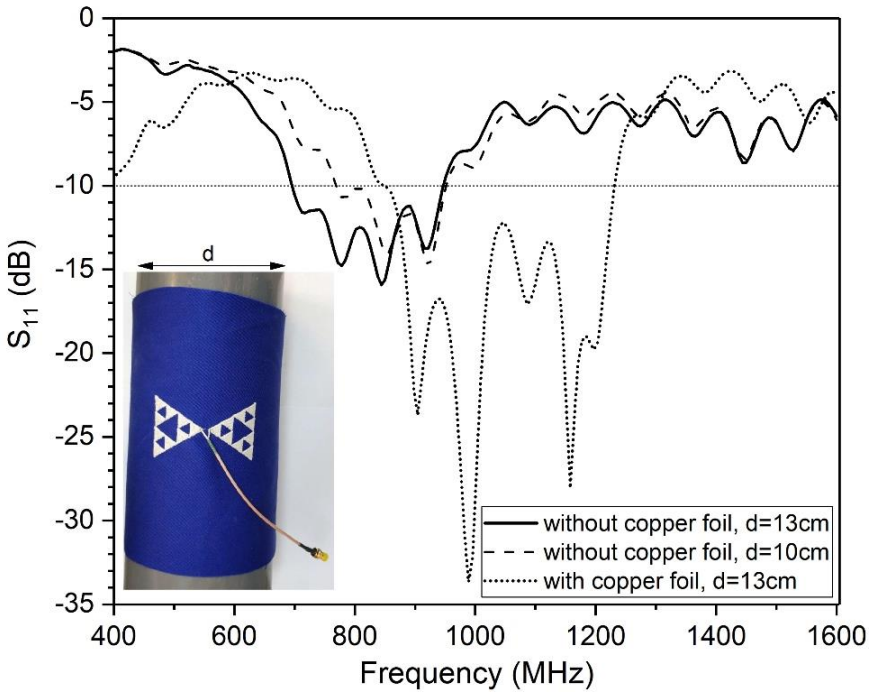

Figure 3. S_{11} versus frequency for the fabricated inset bent antenna, which is mounted on a cylindrical dielectric rod, Pavec et al. (2020).

Figure 4 shows three different measured radiation patterns of the developed structure. The antenna radiation measurement system MegiQ RMS-0660 was used to conduct the measurements. The θ- and φ- radiation patterns of our antenna in free space are represented with solid curves, while the θ- and φ- radiation patterns of the same antenna under different bending conditions, when it is mounted on a cylindrical dielectric rod with diameter $d = 13\,\text{cm}$ (dotted curves) or $d = 10\,\text{cm}$ (dashed curves). The radiation patterns of Figure 4 reveal that our embroidered bow-tie antenna has the same, more or less, characteristic radiation behavior with that of an equivalent electric dipole. It is worth mentioning that, in all bending conditions we have examined, our antenna radiation characteristics are not significantly affected, and its gain remains to about 4.5 dBi.

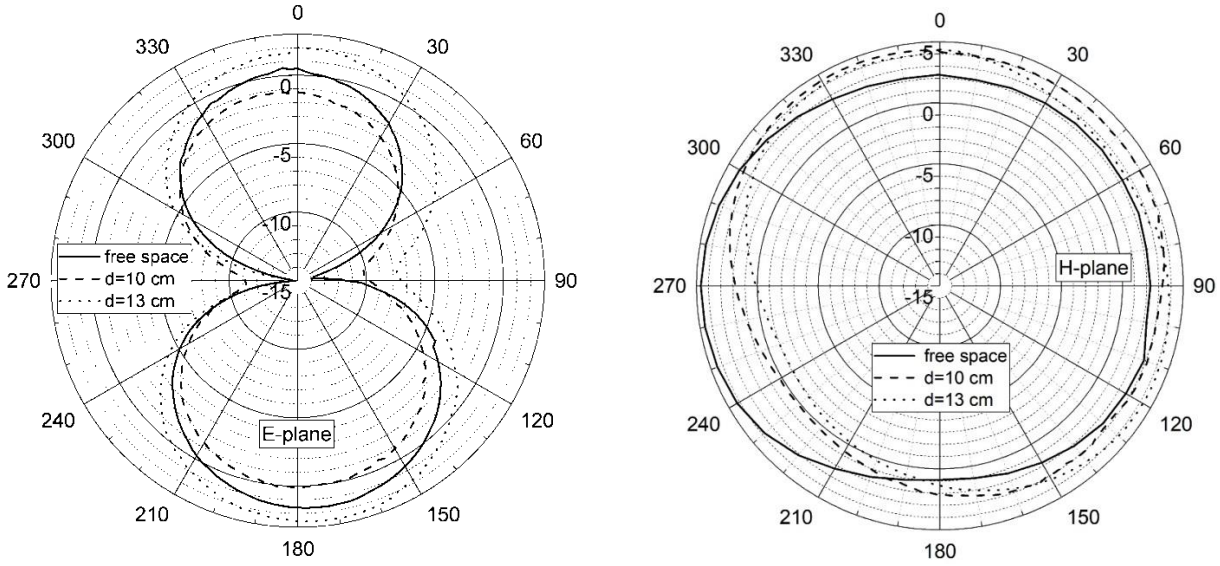

(a) **(b)**

Figure 4. (a) θ- and (b) φ- radiation patterns of the fabricated bow-tie antenna, under different bending conditions, Pavec et al. (2020).

4. CONCLUSION

A fabricated antenna that may be easily integrated into clothing, based on the fractal shape of the Sierpinski triangle, has been presented in this paper. The bow-tie shape has been embroidered on a Dupont Nomex meta-aramid fabric by using a silver hybrid conductive sewing thread.

The actual bandwidth of the antenna has been determined by measuring the S_{11} parameter. The results have shown stable coverage of the unlicensed 868 MHz ISM band in all cases considered. When the antenna is mounted on cylindrical surfaces, the smaller the curvature of the surface the greater the bandwidth. Moreover, a copper foil between the fabric and the dielectric surface may considerably increase the bandwidth. The measured radiation patterns have shown that the gain of antenna may be as much as 4.5 dB, despite the bending conditions; the latter do not seem to affect the radiation characteristics of the bow-tie antenna significantly.

5. ACKNOWLEDGEMENT

The research work of T.N. Kapetanakis, C.D. Nikolopoulos and I.O. Vardiambasis is co-financed by Greece and the European Union (European Social Fund - ESF) through the Operational Program "Human Resources Development, Education and Lifelong Learning 2014-2020" in the context of the project "Smart microwave nanomaterial structures with applications in bodycentric communications and the Internet of Things (MIS 5048187)".

6. REFERENCES

Baliarda, C.P., J. Romeu, R. Pous, and A. Cardama. 1998. On the behavior of the Sierpinski

multiband fractal antenna. IEEE Transactions on Antennas & Propagation, 46: 517–524.
Chowdary, P.S.R., A.M. Prasad, P.M. Rao, and J. Anguera. 2015. Design and performance study of Sierpinski fractal based patch antennas for multiband and miniaturization charecteristics. Wireless Personal Communications, 83: 1713-1730.
Hong, Y., J. Tak, and J. Choi, 2016. An all-textile SIW cavity-backed circular ring-slot antenna for WBAN applications. IEEE Antennas & Wireless Propagation Letters, 15: 1995-1999.
Kaur, J., S. Singh, and A. Kansal. 2011. Multiband behaviour of Sierpinski fractal antenna. Research Journal of Information Technology: 1-9.
Kiourti, A. and J.L. Volakis. 2015. Colorful textile antennas integrated into embroidered logos. Journal of Sensor and Actuator Networks, 4: 371-377.
Liu, F.X., Z. Xu, D. C. Ranasinghe, and C. Fumeaux. 2016. Textile folded half-mode substrate-integrated cavity antenna. IEEE Antennas & Wireless Propagation Lettters, 15: 1693-1697.
Loss, C., R. Goncalves, C. Lopes, P. Pinho, and R. Salvado. 2016. Smart coat with a fully-embedded textile antenna for IoT applications. Sensors, 16: 938.
Moradi, B., R. Fernandez-Garcia, and I. Gil. 2020. Wearable high-performance meander ring dipole antenna for electronic-textile applications. The Journal of the Textile Institute, 111: 178-182.
Pavec, M., J. Navratil, R. Soukup, and A. Hamacek. 2018. A bowtie antenna prepared by aerosol jet and embroidering technology. 2018 41st International Spring Seminar on Electronics Technology (ISSE), Zlatibor: 1-4.
Pavec, M., T.N. Kapetanakis, M.P. Ioannidou, C.D. Nikolopoulos, A.T. Baklezos, R. Soukup, T. Blecha, A. Hamacek, and I.O. Vardiambasis. 2020. Implementation of an all-textile bow-tie antenna for the 868 MHz ISM band. 2020 International Symposium on Electromagnetic Compatibility (EMC Europe 2020), Rome, Italy: 1-3.
Salvado, R., C. Loss, R. Concalves, and P. Pinho. 2012. Textile materials for the design of wearable antennas: A survey. Sensors, 12: 15841-15857.
Sreemathy, R., S. Hake, S. Sulakhe, and S. Behera. 2020. Slit loaded textile microstrip antennas. IETE Journal of Research.
Tsolis, A., W.G. Whittow, A.A. Alexandridis, and J.C. Vardaxoglou. 2014. Embroidery and related manufacturing techniques for wearable antennas: Challenges and opportunities. Electronics, 3: 314-338.

ABSORPTION ANALYSIS OF HIGH-BRIGHTNESS LIGHT-EMITTING DEVICES USING PHOTOCURRENT SPECTROSCOPY

Jaeger, A.[1], Meinert, H.[1]

[1]University of Applied Sciences Esslingen, Flandernstrasse 101, 73732 Esslingen, Germany
Arndt.jaeger@hs-esslingen.de (corresponding author)

1. INTRODUCTION

Development of light-emitting diodes (LED) has gained considerable attention due to their energy saving potential. They are being used in a wide range of applications using visible light such as signage, video walls, automotive and general lighting. By mixing red, green and blue LEDs very efficient white light sources have been demonstrated since luminous efficacies of both III-phosphide and III-nitride LEDs increased over the last decade. Besides research and development work on understanding physical mechanisms of light generation and improving the device characteristics the development of analytical tools for device characterization is required. Here photocurrent spectroscopy (PC) being a well-known tool for semiconductor device characterization (Tomm et al. (1997)) is tested for investigation of commercial AlGaInP LEDs (Streubel et al. (2002)).

2. EXPERIMENTAL

LEDs used in our experiments are manufactured by OSRAM and are mounted in the Golden Dragon package. The amber AlGaInP LED investigated in detail is based on the Thinfilm AlGaInP technology (OSRAM (2012)). According to datasheet provided by manufacturer the LED has a typical luminous efficacy of 75 lm/W and a peak wavelength λ_{peak} = 624 nm at operating currents of I = 0.4 A. The electroluminescence (EL) spectrum is measured utilizing an industrial setup made by Instrument Systems (Leschhorn et al. (2017)). It consists of an integrating sphere with a diameter d = 0.15 m coupled by a fiber bundle to a CAS140CT spectrometer. The light emission of the LED operated by a Keithley 2400 current source is measured by placing the LED inside the integrating sphere.

An additional setup for gaining photocurrent spectra is shown in Figure 1. A SPEX spectrometer (f = 0.22 m) is used for filtering light of a tungsten lamp. The resulting monochromatic light is focused onto the LED giving rise to a photocurrent at wavelengths where carriers are generated by impinging photons in the active region of the pin diode. A Keithley 2400 voltage source enables to apply a reverse bias to the LED and to measure sensitively the direct photocurrent.

All experiments have been performed at room temperature.

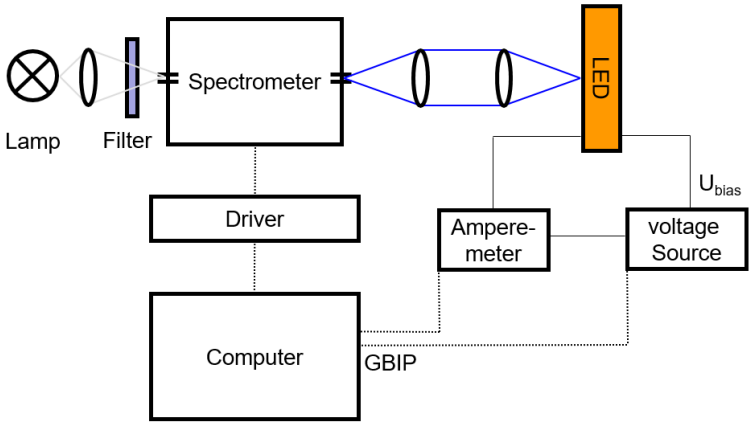

Figure 1. Schematics of photocurrent spectroscopy experiment of LED under applied bias U_{bias}.

3. RESULTS AND DISCUSSION

Figure 2 shows photocurrent spectra of an amber Thinfilm AlGaInP LED measured under different reverse biases. For comparison electroluminescence spectrum of the same device is depicted.

The narrow EL spectrum measured under forward voltage U_f = -1.8 V (I = 5 mA) has a peak wavelength λ_{peak} = 628 nm and a full width at half maximum Γ = 12.4 nm.

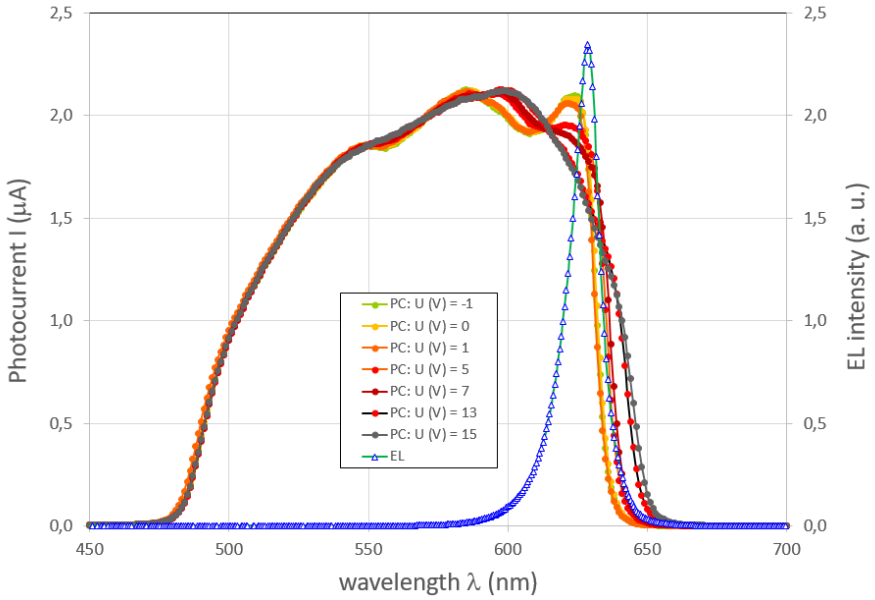

Figure 2. Photocurrent spectra (circles) of amber Thinfilm AlGaInP LED measured under different reverse biases. For comparison electroluminescence spectrum (triangles) of the same device is depicted.

The PC spectra show LED photocurrents between 480 nm and 660 nm. The steep decrease at long wavelengths close to EL peak wavelength is due to the absorption edge of the active AlGaInP pin region. At shorter wavelengths the PC signal decreases gradually since the monochromatic light is partly absorbed in the LED window layers. For wavelengths shorter than about 480 nm PC signal of the LED vanishes since the LED window is no longer transparent for the light.

It is interesting to note that increasing reverse voltages alter photocurrent LED spectra. Increasing reverse voltages result in increasing electric field in the active AlGaInP pin region. The field-induced changes of the photocurrent are most pronounced near the energy band edge at E_g = 1.99 eV. The excitonic transition of the active quantum well in the LED shifts to lower energy (i.e. longer wavelength) and becomes broader with increasing electric field. This behavior can be explained by the quantum-confined Stark effect (QCSE) and depends on the details of the quantum well (Bastard et al. (1983), Matsuura et al. (1986)).

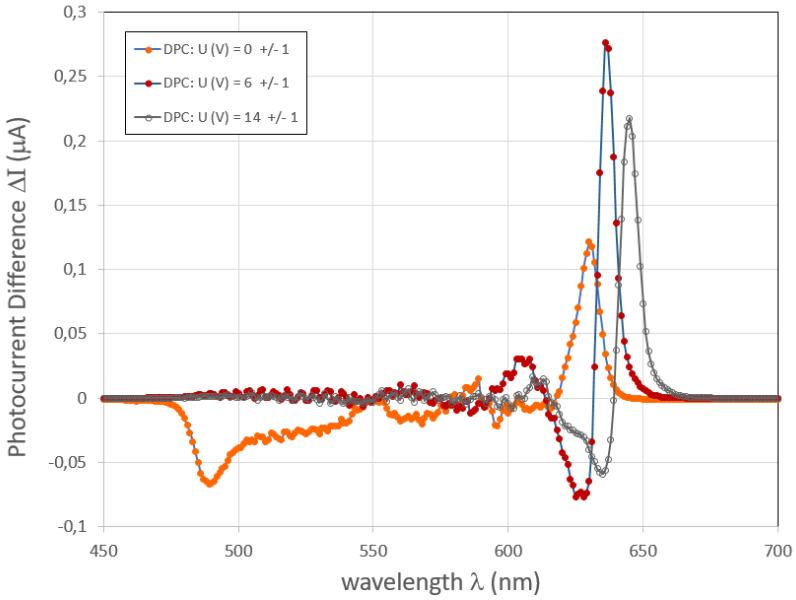

Figure 3. Photocurrent difference spectra of amber Thinfilm AlGaInP LED measured under different reverse biases. The red shift of the lowest lying transition in the quantum well with increasing reverse voltage is clearly visible.

The field-induced changes in PC spectra are better visible by plotting the PC difference spectra as shown in Figure 3. The PC difference spectrum was calculated by subtraction of two PC spectra measured at different voltages, e.g. the PC difference spectrum for U = (6 +/- 1) V in Figure 3 results from subtraction of the PC spectra measured at U_1 = 5 V and U_2 = 7 V in Figure 2. In the PC difference spectrum a strong positive peak at around 640 nm arise which shifts to longer wavelengths with increasing electric field. The lineshape of this PC difference peak is typical for a red shift of the dominating lowest lying quantum well transition. At shorter wavelengths (λ < 600 nm) the PC difference spectra exhibit only weak field-induced changes as it was already observed in the PC spectra of Figure 2.

4. CONCLUSION

Photocurrent and electroluminescence spectroscopies are utilized for analysing active region of high-brightness AlGaInP LEDs while mounted in Golden Dragon package. Under forward bias LED emits light whereas under reverse biases the absorption of the semiconductor is modified by quantum-confined Stark effect exhibiting a red shift of the lowest lying quantum well transition. The occurrence of QCSE proves the existence of quantum well in the active region of the device. Field-induced changes in PC spectra are better discernible by subtraction of field-independent contributions.

5. REFERENCES

[1] Bastard, G., Mendez, E. E., Chang, L. L., and Esaki, L., 1983, Phys. Rev. B 28, 3241-45.
[2] Leschhorn, G., and Young, R., 2017, Handbook of LED and SSL Metrology, Munich.
[3] Matsuura, M., and Kamizato, T., 1986, Phys. Rev. B 33, 8385-89.
[4] OSRAM Opto Semiconductors, Golden Dragon, LA W5AM datasheet, 2012.
[5] Streubel, K., Linder, N., Wirth, R., and Jaeger, A., 2002, IEEE Journal of Selected Topics in Quantum Electronics 8, 321-332.
[6] Tomm, J. W., Bärwolff, A., Menzel, U., Voß, M., Elsaesser, T., Daiminger, F. X., Heinemann, S. and Luft, J., 1997, J. Appl. Phys. 81, 2059-63.

CUSTOM EFFICIENT SWITCHED-MODE LED POWER SUPPLY

Dumbrava, V[1], Pagodinas, D[1], Noreika, A[2], and Kilius, S[1]

[1]Department of Electronics Engineering, Kaunas University of Technology,
Studentu str. 50-340, Kaunas, LT-51368, Lithuania
[2]VŠĮ Mokslo ir technologijų populiarinimo centras, Studentų str. 65,
Kaunas, LT-51369, Lithuania
E-mail: vytautas.dumbrava@ktu.lt

1. INTRODUCTION

Light-emitting diodes (LEDs) have solid advantages over other lighting technologies, mainly due to significant energy savings, long lifetime (often up to 50000 hours), and their design flexibility [5]. For comparison, efficiency of incandescent lamps (at 100 W) reaches (17-20) lm/W, in halogen lamps (25-30) lm/W, in linear fluorescent lamps (90-100) lm/W, and in modern LEDs >130 lm/W [4-5]. LED luminaires are typically powered by switched-mode power supplies (SMPS) because of their flexible design options, including the possibility to integrate them into a GU10 or T8 lamp base. Widely available power supply microcircuits for powering LED lights often have efficiency less than 80%.

The objective is to design and test an efficient (>90%) SMPS for LED luminaires.

2. LED POWER SUPPLY DESIGN

In the initial stage of the research, four different SMPS candidate topologies were analyzed: buck, flyback, push-pull, half-bridge [1-4;6-7]. Comparison is presented in Table 1.

Table 1. Comparison of switched-mode power supply topologies.

Type	*Typical power, W*	*Galvanic isolation*	*Coefficient of efficiency, %*	*Cost*	*Complexity of design*
Buck	0–1000	Not available	65–98	Low	Simple
Flyback	0–250	Available	60–85	Low	Simple
Push-Pull	100–1000	Available	60–90	Average	More complex
Half-Bridge	0–2000	Available	70–90	Average	More complex

The buck-type topology was selected due to its low-cost and high coefficient of efficiency of up to 98%. The actual circuit diagram is shown in Figure 1.

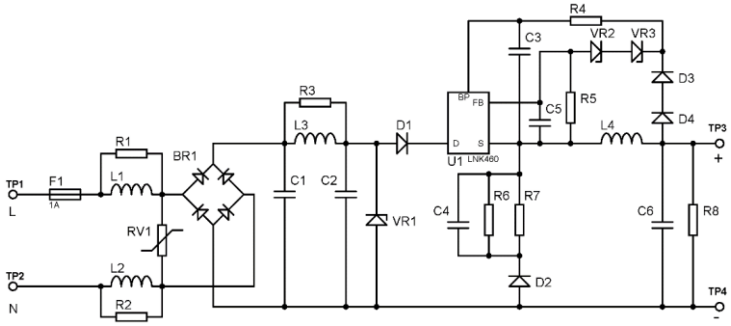

Figure 1. Circuit schematic of the 20 W switched-mode power supply

The developed prototype is a 20 W buck-type SMPS, galvanically not isolated from the electrical grid, and intended to power LED lighting devices. It was designed and manufactured based on LNK460KG microchip. The supply is compact and suitable for T8 LED lamps.

3. EXPERIMENTAL STUDY AND RESULTS

The main electrical parameters were measured according to the diagram presented in Figure 2.

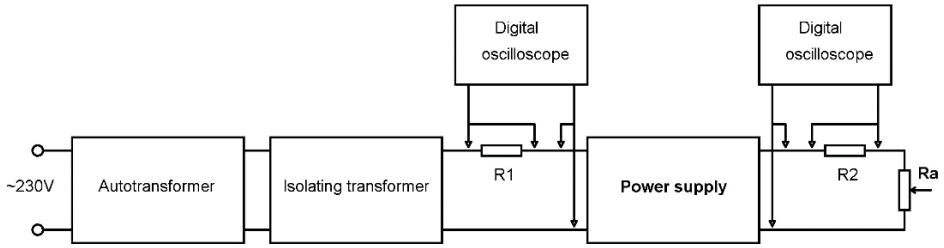

Figure 2. Measurement diagram

Autotransformer changes the magnitude of the input voltage. Isolating transformer is used for galvanic decoupling. Results of efficiency measurements are shown in Figure 3. The coefficient of efficiency is relatively high, depends on the load, and varies in the range (90-96 %). Input voltage (U_{IN}) has little effect on the efficiency.

A regulated resistive load Ra is connected to the output of the supply. Mains power consumption is measured as follows: one digital oscilloscope channel is used to measure the time-domain characteristic of the power supply input voltage, while the other channel measures the time-domain characteristic of the voltage drop across the low-ohm resistor R1 which is connected in series and shunts the input. The electrical currents flowing through the shunt resistor R1 and the test power supply are equal, and therefore the input current of the power supply can be expressed as:

$$i(t) = \frac{u_{R1}(t)}{R1} \qquad [1]$$

For alternating current, the apparent power S consists of active and reactive components P and Q:

$$P = \left(\frac{1}{T} \int_0^T \left| u(t) \cdot i(t) \right| dt \right) \cdot \cos(\phi) = U_{RMS} \cdot I_{RMS} \cdot \cos(\phi) \qquad [2]$$

$$Q = \left(\frac{1}{T} \int_0^T \left| u(t) \cdot i(t) \right| dt \right) \cdot \sin(\phi) = U_{RMS} \cdot I_{RMS} \cdot \sin(\phi) \qquad [3]$$

Then the expression for the calculation of apparent power becomes:

$$S = \sqrt{P^2 + Q^2} = \sqrt{\left(U_{RMS} \cdot I_{RMS} \cdot \cos(\phi)\right)^2 + \left(U_{RMS} \cdot I_{RMS} \cdot \cos(\phi)\right)^2} \qquad [4]$$

Knowing that $\sin^2(\phi) + \cos^2(\phi) = 1$, we can write:

$$S = U_{RMS} \cdot I_{RMS} \qquad [5]$$

The signal is discretized when it is being measured with oscilloscope, and therefore the apparent power can be expressed as:

$$S = \sqrt{\frac{1}{n}\sum_{1}^{n}(u_i \cdot i_i)^2} = \sqrt{\frac{1}{n}\sum_{1}^{n}\left(u_i \cdot \frac{u_{iR1}}{R1}\right)^2} \qquad [6]$$

here n is the number of samples.

The SMPS output power measurement is done by the same principle: one oscilloscope channel is used to measure the voltage drop across the load, and the other channel measures the voltage drop across the shunt resistor R2. Output power for a discretized signal is:

$$P_{OUT} = \sqrt{\frac{1}{n}\sum_{1}^{n}(u_i \cdot i_i)^2} = \sqrt{\frac{1}{n}\sum_{1}^{n}\left(u_i \cdot \frac{u_{iR2}}{R2}\right)^2} \qquad [7]$$

Then, the power supply efficiency coefficient is calculated as:

$$\eta = \frac{P_{OUT}}{S} \cdot 100\% \qquad]8]$$

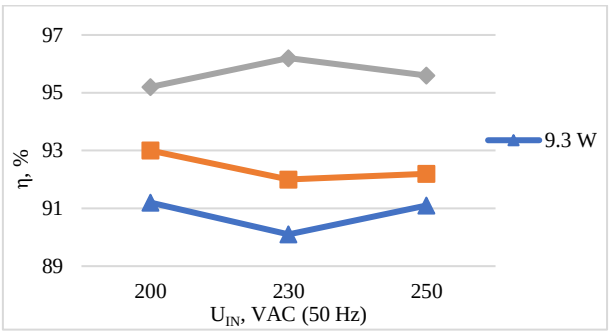

Figure 3. Dependence of efficiency on input voltage at three different load values

Thermal operation mode was evaluated from thermal images made at room temperature (25 °C), SMPS running for >30 minutes, without active cooling and housing, U_{IN} = 230 V. The integrated circuit and the energy-accumulating choke are the hottest components, as visible from Figure 4(a). The choke temperature is ~70 °C at 14.5 W; at 20.5 W temperature increases to 77 °C. Using a dedicated housing would increase the temperature of the supply even further, therefore an additional heat dissipation mechanism should be developed.

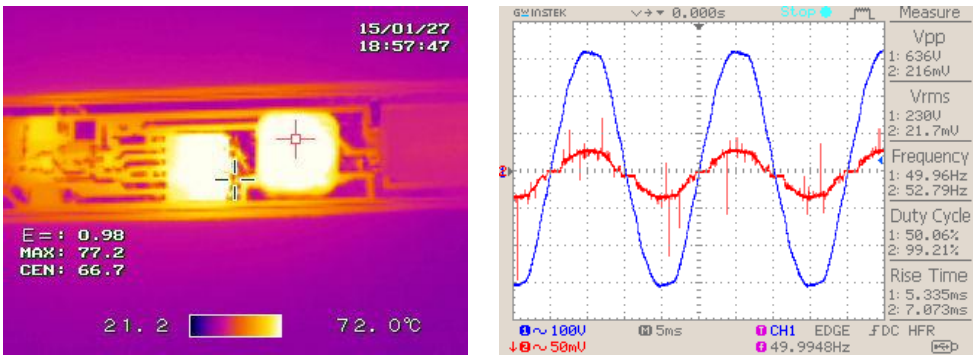

(a) (b)

Figure 4. Thermal image of the power supply with a 20.5 W load (a); input voltage (channel I) and voltage across the input shunt resistor R1 (channel II), U_{IN} = 230 V, load 17.5 W (b)

Figure 4(b) shows the input voltage (channel I) and the voltage across the input shunt resistor R1 (channel II), which is proportional to the input current. When the power supply is switched

on/off, the voltage and the current change steadily until they reach their maximum values. There are no voltage spikes: no risk to damage the load (LEDs).

EMC test was conducted according to the diagram presented in Figure 5(a) [3], based on definitions of EN55015 (CISPR 15) directive. A 20 W SMPS was tested at 230 V 50 Hz input voltage, at room temperature.

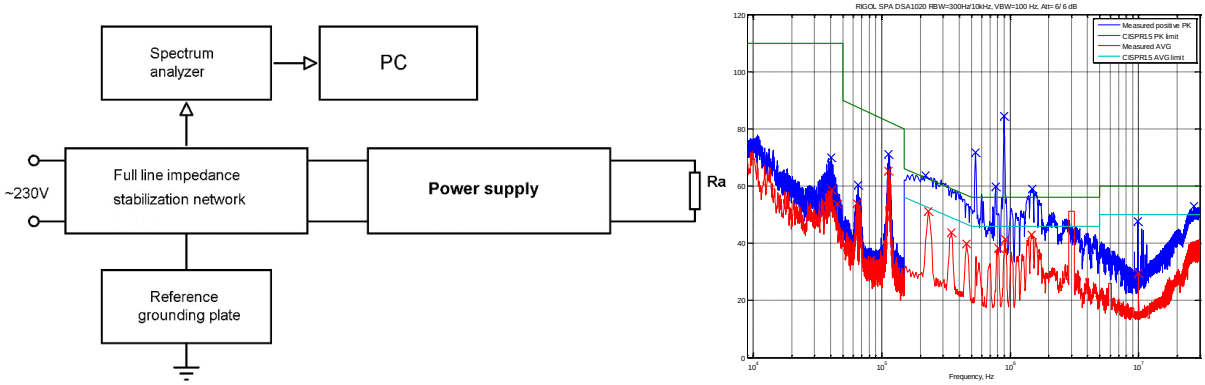

(a) (b)

Figure 5. EMC measurement setup (a); EMC test results: interference produced SMPS (b)

The plot of the EMC test results is shown in Figure 5(b), where solid lines indicate permissible limits. The prototype does not meet standard requirements due to noise components exceeding the permissible limits at some frequencies (especially at 540 kHz and 895 kHz). Different PCB layouts should be tested, and a better mains power filter should be developed.

4. CONCLUSIONS

Buck-type is a preferable topology, because SMPS of this type have high coefficient of efficiency (up to 98%). The custom-designed power supply has high efficiency (94.5 % at 20W load), high power factor, simple and compact design. The efficiency is only slightly influenced by the variation of the input voltage. Efficiency increases linearly with the increase of load.

5. REFERENCES

1. Eung-Seok Kim, Cherl-Jin Kim, Heung-Kyo Shin, Nonlinear State Feedback Controller Design for Buck-Boost Converters, (International Conference on Electrical Machines and Systems (ICEMS), (Jeju, Korea, 2018), p.p.2418-2422.
2. Jong-Woo Kim, Jung-Muk Choe, Jih-Sheng Lai. Forward-Flyback Converter for LED Driving with Reduced Number of Components, IEEE Energy Conversion Congress and Exposition (ECCE), Cincinnati, OH, USA, (2017) p.p. 3684-3687.
3. L. Svilainis, V. Dumbrava, Fleet Management Module, Electromagnetic Interference Investigation, Elektronika ir elektrotechnika, vol.19, issue 4, (2013), p.p. 53-56.
4. L.Svilainis, V. Dumbrava, A. Chaziachmetovas, Investigation of the Half Bridge and Transformer Push-Pull Pulser Topologies for Ultrasonic Transducer Excitation, Journal of Circuits, Systems and Computers, Vol. 24, No. 05, (2015).
5. N. Narendran, Y. Liu, X. Mou, D. R. Thotagamuwa, and O. V. M. Eshwarage, Projecting LED Product Life Based on Application, Fifteenth International Conference on Solid State Lighting and LED-based Illumination Systems, Vol.9954, 99540G 1-7 (2016).
6. R. M. Rubinger, E. R. da Silva, D. Z. Pinto, C. P. L.Rubinger, A. F. Oliveira, E. C. Bortoni, Optical Engineering 54, (2015) .
7. S. K. Rönnberg, M. Wahlberg and M. H. J. Bollen, Harmonic Emission before and after Changing to LED and CFL, Part II: Field Measurements for a Hotel. In IEEE conf. 2010, Bergamo, pp. 1-7.

MCR – WPT ANALYSIS AND DESIGN REVISION

Naser A. Abu-Zaid[1]

[1]An-Najah National University, Nablus, P.O.Box 7, Palestine
naserzaid@najah.edu; naserabuzaid1968@gmail.com

1. INTRODUCTION

This revision represents a short summary on magnetic coupling resonance – wireless power transfer (MCR-WPT) methodologies, analysis and design. It introduces the basic structures of MCR-WPT system and modeling methods. Such techniques are used in electric vehicle and mobile phone wireless charging. Circuit theory models are used to investigate system parameters such as transmission efficiency, impedance matching, frequency reduction, and obviously variations with coupling quality. The load matching factor and the transfer quality factor are investigated with relevance to transfer efficiency, the optimal load matching to achieve maximum transfer efficiency was included. The important cases of a constant-voltage receiver and a constant-current receiver was considered, which aids in the design of WPT systems for EVs. Finally, some simulation results were demonstrated.

2. MODELS AND METHODOLOGIES

The main methods used for WPT are classified as radiating and non-radiating, Zang and Zhao (2018). Non-radiating methods include magnetic induction, magnetic coupling resonance and capacitive induction. Radiating methods includes microwaves and lasers. To analyze and model magnetically coupled systems, techniques such as coupled mode theory, circuit theory, two-port network and bandpass filter models were used. The basic structure consists of a transmitter, transfer system and receiver. Transmitter includes energy source and power converters. Transfer system includes compensation network(s), transmitting coil and receiving coil, while receiver include loads and power converters. In this revision, circuit theory models are used to demonstrate the basic parameters and characteristics of WPT systems.

3. RESONANCE, TRANSFER QUALITY AND MATCHING FACTORS

To illustrate and discuss the characteristics of WPT systems, a simple two coil structer is designed and analyzed. The transfer efficiency of the system is given by, Zang and Zhao (2018)

$$\eta_{tr} = \left(\frac{T_Q^2}{1+L_M+T_Q^2}\right)\left(\frac{R_L}{R_2+R_L}\right) \qquad [1]$$

Where

$$T_Q = \frac{\omega_o M_{12}}{\sqrt{R_1 R_2}} \qquad [2]$$

In the above equations ω_o is the radian resonace frequency, M_{12} is the mutual coupling inductance, R_1 is the transmitter resistance, R_2 is the receiver resistance and R_L is the load resistance. The transfer quality factor T_Q measures the quality of coupling between transmitting and receiving coils and the load matching factor R_L/R_2 introduces the effect of load variation on transmission efficiency, Zang (2013) et al. Since power electronic devices performs better at lower frequency, the resonance frequency may be reduced by increasing the inductance value which will improve the coupling by a factor propotional to the square of the turns ratio and hence the transmission efficiency, Zang (2014) et al. In that respect, it is not advised to increase the

capacitance value since that would degrade the efficiency. Another factor that is noticed with strong coupling is the appearance of efficiency peaks at different frequencies,Liu (2020) et al., which means that frequncy splits at critical values of transfer quality factor.

4. SIMULATION RESULTS

To illustrate, a series-series configuration is used with single phase $120Vrms$ at $60Hz$. An optimal load resistance gives 0.93 power factor at the receiving coil. The power factor of the transmitting coil changes according to coupling coefficient starting from 0.38 for full coupling and ending at 0.004 at 10% coupling. The total efficiency versus coupling coefficient is shown in Figure1 which is measured from generator to load resistance. The Transfer path efficiency is shown in figure 1 which is measured from input of transmitting coil to output of receiving coil. Maximum transfer efficiency for a constant voltage load could be obtained when the power factor and the voltage gain satisfy certain conditions, Zang and Zhao (2018).

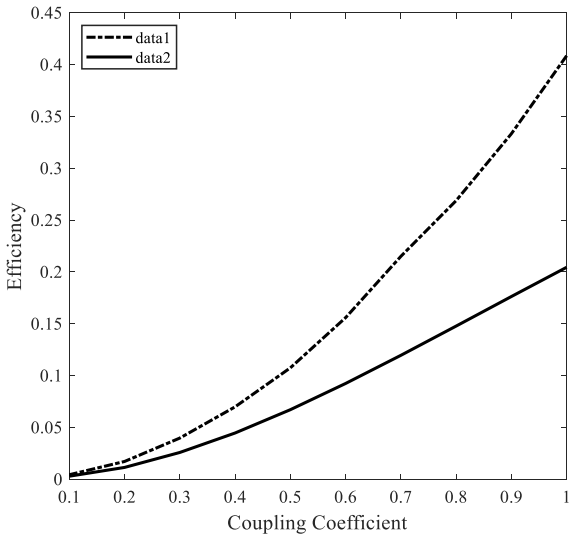

Figure 1. Total efficiency (data 2) and Transfer path efficiency (data 1)

5. CONCLUSION

The simulation results show that a larger transfer quality factor would increase the transmission efficiency. An optimal load matching factor exists for which the transfer efficiency is maximum. In order to reduce resonant frequency, the inductance increment results in higher efficiency than capacitance increment. The active load requires careful design of rectifiers and inverters depending on the nature of the battery to be charged to obtain maximum efficiency. The effect of a moving receiver with static transmitter on the coupling behaviour of the system could be carried out. Also, electromagnetic considerations of material losses, interference, and obstacles in the transmission path may be investigated. Multiple low power receivers are a promising application of WPT for IoT.

6. REFERENCES

Liu J, Wang C, Wang X and Ge W. 2020. Frequency splitting and transmission characteristics of MCR-WPT system considering Non-Linearities of compensation capacitors. Electronics. 9, 141.

Zhang Y, Zhao Z, Chen K. 2014. Frequency decrease analysis of resonant wireless power transfer. IEEE Trans Power Electron, 19:1058-1063.

Zhang Y., Zhao Z, Chen K. 2013 Load matching analysisof magnetically-coupled resonant wireless power transfer. IEEE ECCE Asia down under (ECCE Asia). 788-792.

Zhang Y, Zhao Z. 2018. Doctoral thesis accepted by Tsinghua university on key technologies for wireless power transfer. 130 pages.

NUMERICAL STUDY OF NANOSCALE HEAT TRANSFER IN MOS TRANSISTOR SYSTEM

Oussama Zobiri[1], Abdelmalek Atia[1]
[1]University of El Oued, LEVRES Laboratory, Faculty of Technology, 39000 El Oued, Algeria
E-mail: abdelmalek-atia@univ-eloued.dz

1. Introduction

From the first appearance of semiconductor electronics to today, the number of transistors integrated in a circuit has been increasing. MOSFETs or MOS transistors were influenced by this miniaturization and the MOSFET channel region has become smaller than the phonon mean free path(Arsov 2013). The characteristic length (Lc) in the MOSFET was projected to be 13 nm in 2018, however, the miniaturization of MOSFET has already reached the nano-scale, and it is expected to be less than 6 nm in 2026(Fiori *et al.* 2014) .The Boltzmann transport equation (BTE) is non-Fourier equation applied for investigate thermal transfer mechanism in structures from meso to macro-scale. Besides Joule effect (heat source), another heat source appears in the nano-MOSFET. This source stems from the phonon-wall collision in the MOS transistor interface and is expressed as temperature jump boundary condition(Ghazanfarian & Abbassi 2012). The present study has the goal to study the effect of temperature jump at the interface Si/SiO_2 in 2D nanoscale conventional MOS device using the lattice BM.

2. Lattice Boltzmann Method (LBM)

Phonons, which are quanta of lattice vibrations, are the primary thermal energy carriers in semiconductor material. To include the heat transport effect in the nano-scale devices, the transient energy Boltzmann transport equation for phonons is given by(Escobar *et al.* 2006):

$$\frac{\partial u}{\partial t} + v.\nabla u = -\frac{u - u^{eq}}{\tau} + q_v \qquad [1]$$

The discrete Boltzmann lattice equation with a heat source (Eq. (1)) can be discretized for each lattice site for the phonons in time and space:

$$u_i(\bar{x} + \Delta\bar{x}_i, t + \Delta t) - u_i(\bar{x}, t) = -\frac{\Delta t}{\tau}\left[u_i(\bar{x}, t) - u_i^{eq}(\bar{x}, t)\right] + k_i \Delta t q_v \qquad [2]$$

3. Results and Discussion

In order to validate the present model with jump condition, the numerical results of peak temperature($T-T_{ref}$) rising were compared with those of Fourier, and BTE(Yang *et al.* 2005) . The peak temperature at the centerline of the MOS transistor with elapsed time is compared in Figure 1. As clearly seen in the figure, in short times all models have the same behavior. The estimated peak temperatures at time scale of t = 30 ps are 26 K for present model L_c=5 nm and 36 K for L_c=15 nm while 28 K for BTE and 5 K for Fourier law . The possible reason for the deviation of the obtained results to those obtained by BTE, and Fourier law is due to heating sources, in which the ordinary Joule effect is the only heating source in the Fourier law. While the temperature rises in the present model are due to the Joule effect and the phonon wall-collision, in BTE the heat sources is the self-heating and the phonon emission.

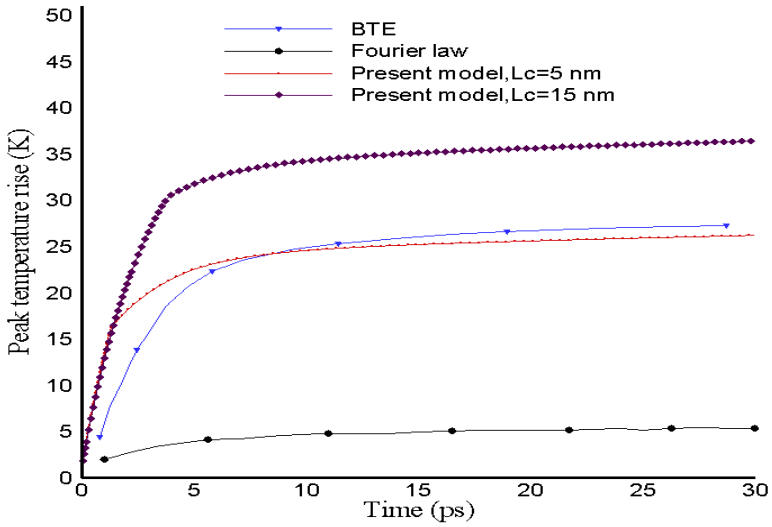

Figure 1. Comparison of the peak temperatures in the centerline of the MOSFET

References

Arsov GL (2013): Celebrating 65th anniversary of the transistor. *Electronics* **17**, 63-70.

Escobar RA, Ghai SS, Jhon MS & Amon CH (2006): Multi-length and time scale thermal transport using the lattice Boltzmann method with application to electronics cooling. *International Journal of Heat and Mass Transfer* **49**, 97-107.

Fiori G, Bonaccorso F, Iannaccone G, Palacios T, Neumaier D, Seabaugh A, Banerjee SK & Colombo L (2014): Electronics based on two-dimensional materials. *Nature nanotechnology* **9**, 768.

Ghazanfarian J & Abbassi A (2012): Investigation of 2D transient heat transfer under the effect of dual-phase-lag model in a nanoscale geometry. *International Journal of Thermophysics* **33**, 552-566.

Yang R, Chen G, Laroche M & Taur Y (2005): Simulation of nanoscale multidimensional transient heat conduction problems using ballistic-diffusive equations and phonon Boltzmann equation. *Journal of Heat Transfer* **127**, 298-306.

A TABLETOP PLASMA FOCUS NEUTRON SOURCE

I. Fitilis[1,2], A. Skoulakis[2], E.L. Clark[2], E. Kaselouris[2,3], M. Bakarezos[2,3], J. Chatzakis[1,2], V. Dimitriou[2,3], N. A. Papadogiannis[2,3] and M. Tatarakis[1,2]

[1] Department of Electronics Engineering, Hellenic Mediterranean University, Chania, Greece
[2] Institute of Plasma Physics and Lasers, Hellenic Mediterranean University, Rethymnon, Greece
[3] Department of Music Technology and Acoustics, Hellenic Mediterranean University, Rethymnon, Crete, Greece
E-mail: fitilis@hmu.gr

Abstract

A low-cost portable Mather type miniature plasma focus device of 300 Joules energy designed for neutron production is presented at this work. A series of shadowgraphy and interferometry images taken utilizing laser pulses of 150 ps duration were implemented for the characterization of the very fast plasma dynamics. The X-ray and neutron emission were also measured through PIN diodes and a photomultiplier/scintillator device respectively. The MonteCarlo simulation code FLUKA was used for the accurate calibration of the photomultiplier/scintillator device. A survey for the correlation of the neutron emission yield with the plasma formation dynamics including the development of Magnetohydrodynamic (MHD) instabilities has been attempted. The results show the evolving correlation between the neutron yield and the electrical characteristics of the device (i.e. current shape) as well as with the plasma parameters such as the plasma pinching time and the onset of the MHD instabilities.

1. Introduction

The Dense Plasma Focus (DPF) is a plasma generator device in which the plasma produced by pulsed electrical power discharge in gas is magnetically driven and compressed to high densities by the proper design of the electrodes. The DPF technology is introduced at the end of 50s by independent work from Mather (USA) (Mather 1965) and Filipov (USSR) (Filipov et al. 1962) and since then various DFP devices are constructed for research and applications. One of the most attractive application of DPF is the possibility to compress deuterium or/and Tritium gas in order to induce fusion phenomena in prospect to be used as electrical power generator. To increase emission of the high energy neutrons produced by the fusion process powerful DPF devices in median (2-10kJ) (Zakaullah et al. 1998), (Mohammadi et al. 2007), high (10-500kJ) (Czekaj et al. 1989), (Mahabadi et al. 2007) and very high (>0.5MJ) (Schmidt et al. 2002), (Brzosko et al. 1987) energy ranges are constructed, and a scaling law of neutron yield is extracted (Krompholz et al. 1981), (Lee 2008). It is founded that DPF could not be applied for commercially electrical power generation but could be efficient as a neutron source for other applications (Soto 2005), (Saw and Lee 2017). Considering the scaling law, the construction of smaller size DPF devices becomes also attractive as neutron sources for various applications in non-destructive testing of materials/components, in medical and security inspection applications, in material modifications, as well as an EUV/X-ray source for application in microelectronics lithography or surface micromachining.

In this work a table-top portable DPF device of 400J energy was developed and optimized for neutron production. It is presented the electrical and structural characteristics of the device, following the description of the diagnostics for plasma dynamics characterization, while are presented and discussed the results, and at the last section are presented and discussed the results of the neutron generation.

2. The DPF device

The miniature plasma focus device that was developed is consisted of a modified 4-way cross fitting flange where an anode rod was properly placed at one of the 4 ports while the cylindrical wall of the chamber has the role of the cathode. At figure 1 is depicted the structure details of this configuration.

Part details	Specs
ANODE	
Material	O.F.
Type	Copper
Max. radius	Tapered
Min. radius	4.75mm
Hole radius	3.50mm
Free Length	1.00mm
	12.00mm
Cathode	
Type	Plate+Wall
Material	Brass+Al
Diameter	38+39 mm
INSULATOR SLEEVE	
Material	Pyrex
Eff. length	15mm
Inner radius	5mm
Wall thickness	1mm
WORK GAS	
Type	Deuterium
Press. range	1-4 mbar

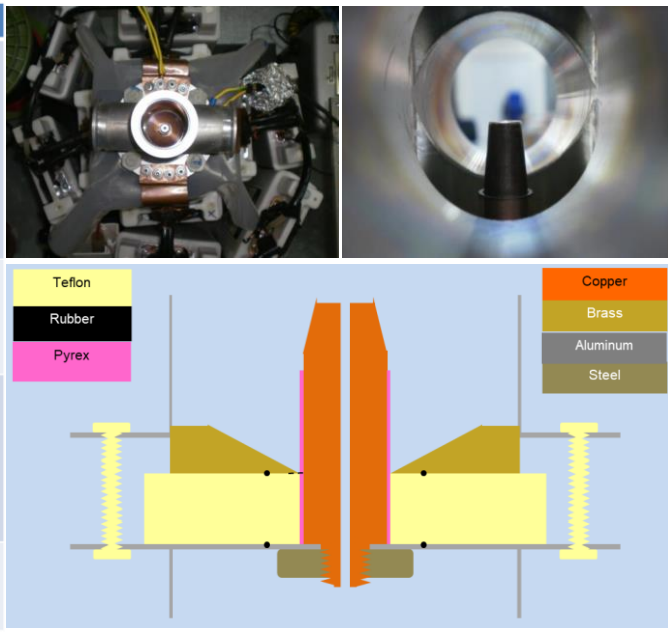

Figure 1. The miniature plasma focus structure. The table at left shows the structure details, at the top are images of the opened chamber, from top and from the side, while at the bottom is a schematic of the modified flange for the electrode's configuration.

The plasma focus chamber is connected by a spark-gap switch to an array of ten capacitors that store the electrical energy for the discharge. The electrical characteristics of the compact device are in the Table 1 as measured and correlated to an RLC simulation model.

Table 1. Electrical characteristics of the miniature Plasma Focus device.

Electrical Characteristics	Value
Max. Stored Energy	~ 400J @ 19kV
Eq. Capacitance(C)	2020nF ± 10%
Eq. Inductance(L)	38nH
Eq. Resistance(R)	87.4mΩ
Quarter time period(T/4)	436ns@Average 388ns@1st peak
Peak Current (I_{pk}) at 18.5 kV	~70 kA
Characteristic impedance (Z_o)	137.5 mΩ

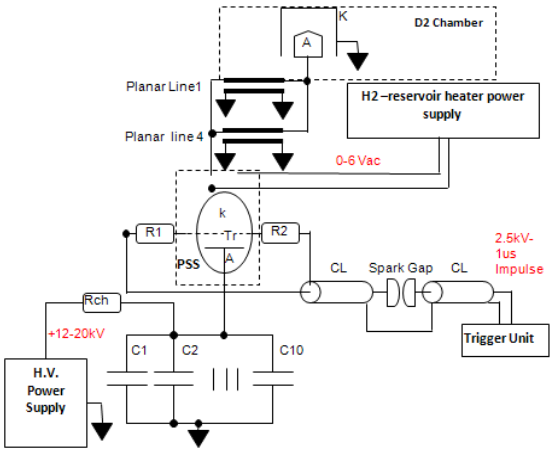

Figure 2. Electrical diagram of the PF device

3. Diagnostic of plasma dynamic

For the characterization of the plasma generated in the PF device a pulsed laser of ps duration is utilized for laser probing imaging of the fast dynamic plasma evolution. In figure 3 a schematic of the signal layout for the diagnostics experiments is depicted. The laser starts the experiment by triggering the spark gap switch and a Rogowski groove measure the current derivative while also it triggers the laser output after a defined delay to capture a snapshot of the plasma evolution. Also, an Al-filtered photodiode and a scintillator/photomultiplier tube (PMT) are used for measuring the soft x-rays photons and x-ray/neutrons emission, respectively.

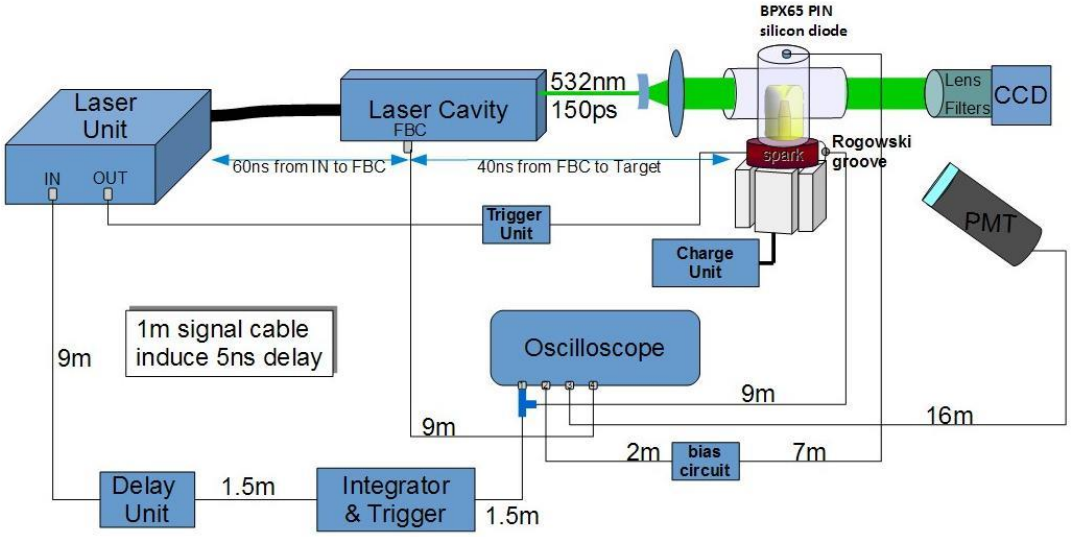

Figure 3. The signals layout of the experiment setup

The laser probe plasma diagnostics used in this work are the shadowgraphy and the interferometry imaging of the plasma. In figure 4 a schematic of the optical layout is depicted. The laser beam is expanded to cover the area of interest and a beam splitter creates the reference beam for the Mach-Zehnder interferometry configuration. The probe and reference beam are combined to produce the interference fringes while a lens images the plasma among with the fringes to a CCD camera. For the shadowgraphy a stop blocks the reference beam.

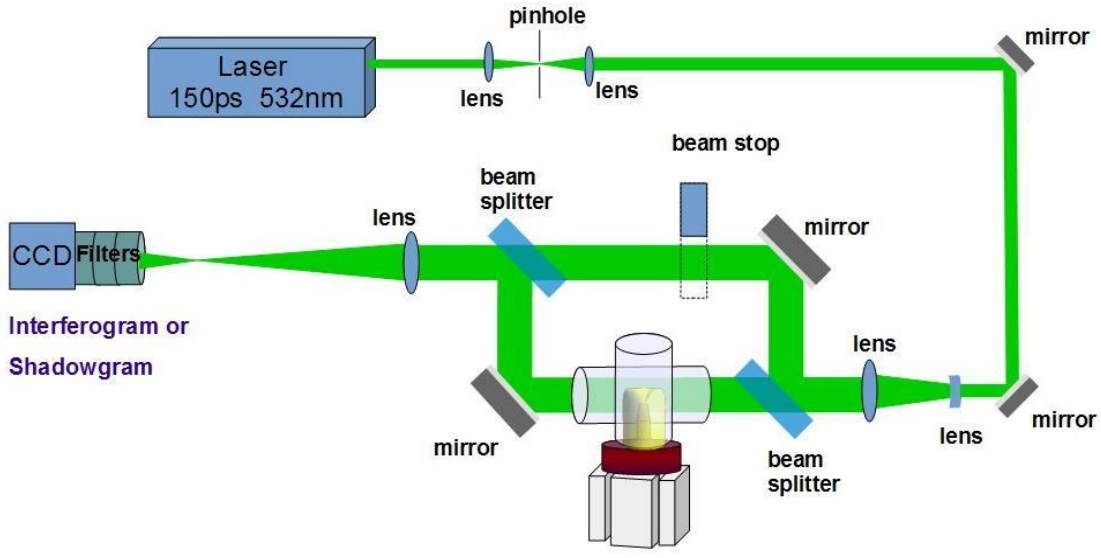

Figure 4. The optical layout of the experimental setup

Results

Indicative shadowgraphs of the plasma dynamic evolution close to the pinch time of the maximum compression (referred as zero time) are shown in figure 5 are also shown the current derivative (dI/dt) measurements. The successful radial compression exhibits a characteristic deep at the dI/dt signal, while afterward the decomposition of the dense plasma column shows plasma instabilities that are usually developed.

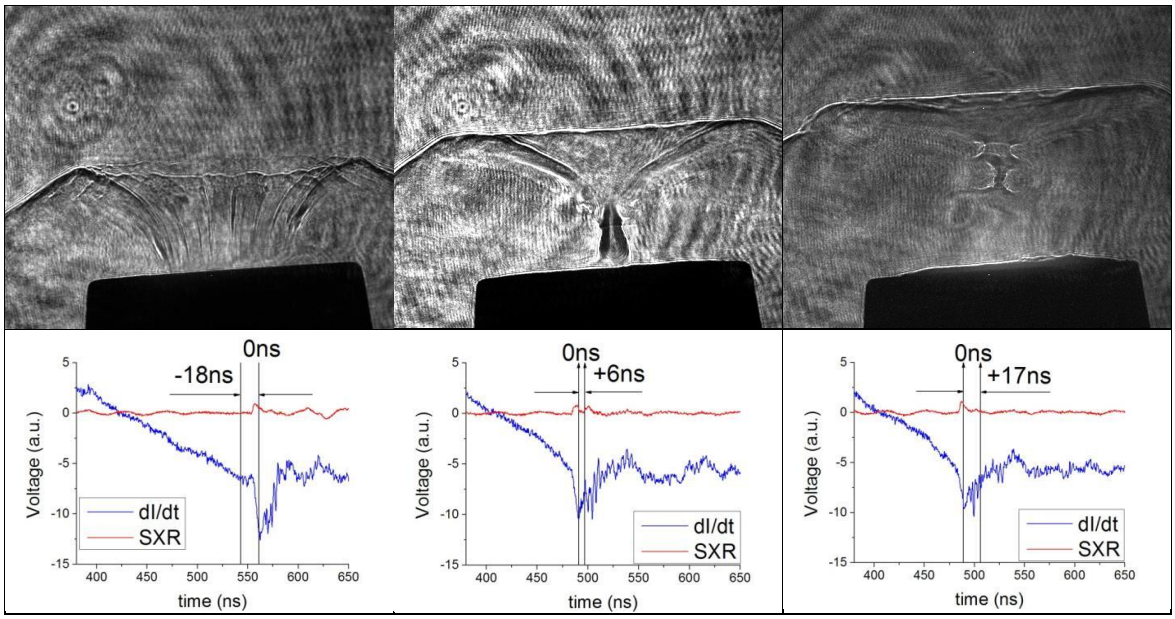

Figure 5. Indicative shadowgrams of the plasma dynamic at time instants close to the maximum compression accompanied by the current derivative and the soft X-ray measurements for each

The high compressed plasma reaches an electron density of more than $1 \cdot 10^{25}$ m^{-3} as measured by the interferograms where an indicative electron density radial distribution result is shown in figure 6.

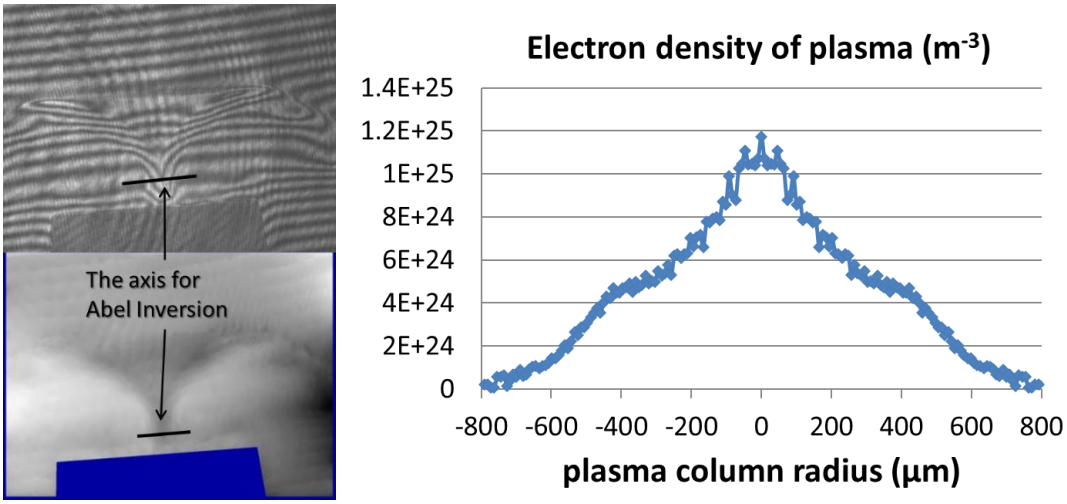

Figure 6. Indicative plasma density radial distribution measurement extracted by interferogram image using the software IDEA

4. Neutrons diagnostic

For the evaluation of the PF device as neutron source a neutron detector consisting of a plastic scintillator and a photomultiplier tube is utilized. The Time of Flight (ToF) method is used for neutrons energy evaluation by the time difference Δτ between hard X-rays (HXR) and neutrons (N) signals peak rise, both captured by the detector (Figure 7a). From the known distance between the source and the detector, the neutron energy is evaluated for each shot and the measurements from a series of shots are depicted in Figure 7b.

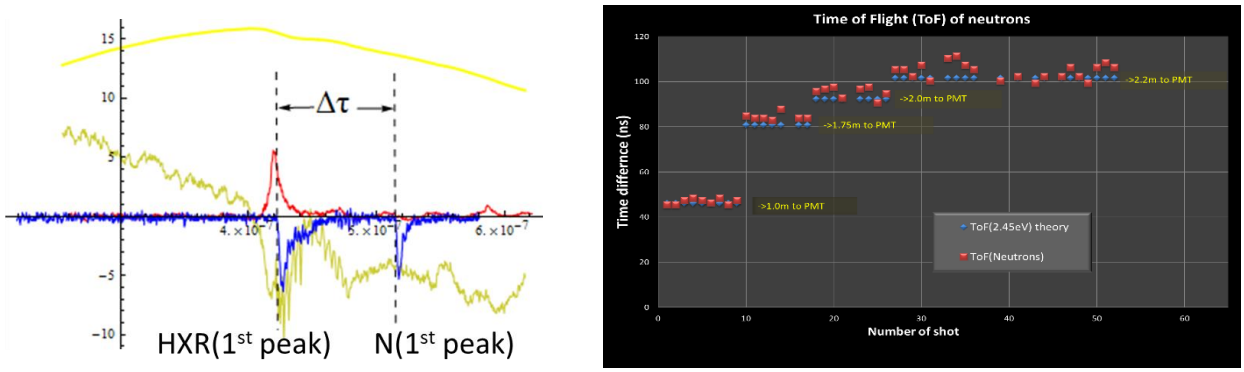

(a) (b)

Figure 7. (a) Recorded signals at fast oscillator, in blue the signal of the scintillator/Photomultipiler for the Hard X-Ray (HXR) and Neutron (N) emission captured, in red the signal of the filtered-photodiode inside chamber for the Soft X-Rays (SXR) emission, in gold color is the signal from the rogowski groove for the time derivative of the current (dI/dt), while the integration of that gives the current's waveform in yellow. The signals from different diagnostics was synchronized for time differences due to cable lengths or other delay sources, by proper calibration trial. (b) ToF measurements results for a series of shots for the evaluation of neutrons energy.

For the neutron yield evaluation, the detector was calibrated according to the minimum dose need to get a single count pulse. The dose deposited to the scintillator is proportional to the light output produced and recorded by the photomultiplier. To find the minimum dose a Cs-137 source of known activity A=1.293x10^5 Bq was used, where by 95% gives photon emission of 600keV. A rate of 76.7 pulses/sec was measured. Using the Fluka code (Ferrari et al. 2005), (Böhlen et al. 2014) we simulated the impact of the 600keV photons source to the scintillator and found that the deposited energy (per mass) is 0.05326 GeV/g/photon, so multiplying by 95%A gives 6542 GeV/g per second. Divided by the measured counts rate we found that the dose of 85.3 GeV/g must be deposited to get a single count.

The Fluka code simulation of a 2.45MeV neutron beam to the scintillator gave similarly a deposited energy of 1.28068 GeV/g/neutron. So, for the required dose of 85.3 GeV/g to get a measurable count is needed 66.6 neutrons. For the scintillator front area of 9.1 cm^2 and the distance of ~250 cm where neutron's signal detected in 50% over the shots, a solid angle of 1.46x10^{-4} steradians calculated. So, an amount of 4.56x10^5 neutrons/steradians is evaluated and for 4π emission we get a yield of 5.7x10^6 neutrons per shot.

A correlation of the neutron yield to the measured signal characteristics was attempted. The neutron's signal peak amplitude versus the time difference between hard x-ray and soft x-ray emission are depicted in Figure 8a. Although not so clear, it seems that the highest number of neutrons are produced when HXR is emitted closer to the time of SXR emission. A correlation of the pinch efficiency to the neutron yield was tested. The neutron's signal peak amplitude versus the deep of the current derivative (dI/dt) is plotted in Figure 8b. The signal deep is defined by the difference of the values it has at the instant of pinch and at the instant of HXR emission. Because of noisy signals not all shots gave information in this graph. There is not a clear dependence of the neutron yield to the strengthen of pinch, although whenever there was not signal from scintillator/PMT was accompany by a poor pinch as derived from a shallow deep of the current derivative signal.

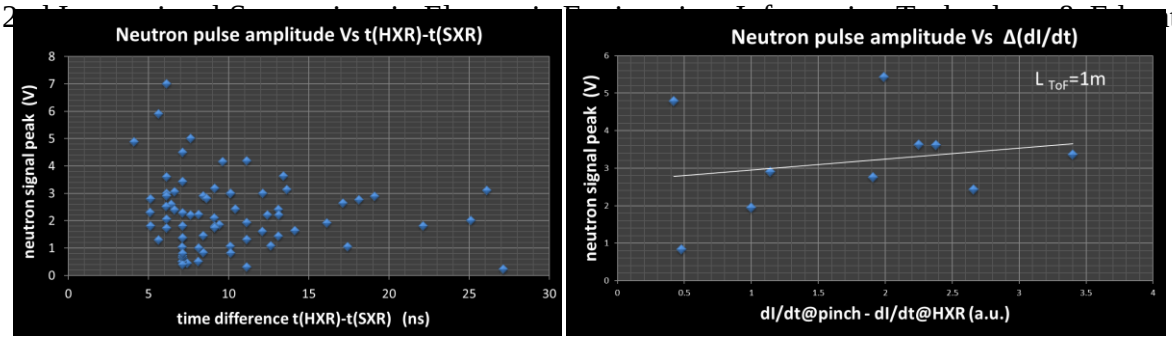

(a) (b)

Figure 8. Neutron yield correlation to (a) the time difference between hard x-rays (HXR) and soft x-rays (SXR) emission and (b) the difference of the current derivative signal (dI/dt) between the time of pinch and the time of HXR emission

5. Conclusion – Future work

A low-cost miniature Plasma Focus Device was constructed and characterized. The time evolution of plasma dynamic was recorded using laser probing shadowgraphy and interferometry. The plasma density distribution as evaluated from interferometry images show that at the pinch time of maximum compression the density reaches more than $1 \cdot 10^{25}$ m^{-3}. The emission of x-ray and neutrons was recorded and the monoenergetic neutrons was evaluated by ToF method. A method for the neutron yield evaluation was performed giving the production of 5.7×10^{6} neutrons per shot. Also the relation of the neutron yield to other recorded diagnostics signals was performed, although not a clear conclusion derived from that.

There is planning to upgrade the system to support energy up to 3 kJ, with new capacitors of low inductance and higher capacity and new spark gap switch, while a new design of the chamber and electrodes configuration will properly match the electrical characteristics to the plasma dynamic.

6. Acknowledgment

We acknowledge support of this work by the project “ELI - LASERLAB Europe Synergy, HiPER& IPERION-CH.gr” (MIS 5002735) which is implemented under the Action “Reinforcement of the Research and Innovation Infrastructure”, funded by the Operational Programme "Competitiveness, Entrepreneurship and Innovation" (NSRF 2014-2020) and co-financed by Greece and the European Union (European Regional Development Fund).

7. References

Böhlen T.T., Cerutti F., Chin M.P.W, Fassò A., Ferrari A., Ortega P.G., Mairani A., Sala P.R., Smirnov G., Vlachoudis V. 2014 Nuclear Data Sheets 120, p.p. 211-214 .

Brzosko J S, Robouch B V and Klobukowska J 1987 FusionTechnol. 12, p. 71.

Czekaj S, Kasperczuk A, Miklaszewski R, Paduch M, Pisarczyk T and Wereszczynski Z 1989 Plasma Phys. Control. Fusion 31, p. 587

Filipov N V, Filipova T I and Vinogradov V P 1962 Nucl. Fusion (Suppl.) 2, p. 577.

Ferrari A., Sala P.R., Fasso A., Ranft J. 2005 CERN-2005-10, INFN/TC_05/11, SLAC-R-773

Krompholz H., Rühl F., Schneider W., Schönbach K., HerzigerKrompholtz G., 1981 Physics Letters 82, p. 82.

Lee S, 2008 Plasma Phys. Control. Fusion 50, 105005

Mahabadi T D and Tafreshi M A 2007 Plasma Phys. Control. Fusion 49, p. 1447.

Mather JM (1965), Phys. Fluids 8,No. 2, pp. 366-377.

Mohammadi M A, Verma R, Sobhanian S, Wong C S, Lee S, Springham S V, Tan T L, Lee P and Rawat R S 2007 Plasma Sources Sci. Technol. 16, p. 785.

Schmidt H, Kasperczuk A, Paduch M, Pisarczyk T, Scholz M, Tomaszewski K and zydłowski A 2002 Phys. Scr. 66 168.

Soto L, 2005 Plasma Phys. Control. Fusion 47, p.361

Saw S.H., Lee S, 2017 AIP Conference Proceedings 1824, 020002
Zakaullah M, Akhtar I, Waheed A, Alamgir K, Shah A and Murtaza G 1998 Plasma Sources Sci. Technol. 7, p. 206.

ADVANCES IN PLASMA PARTICLE ACCELERATOR SUDIES VIA PIC SIMULATIONS ON THE HPC FACILITY – ARIS

Tazes I.[1,2], Andrianaki G.[1], Grigoriadis A.[1], Koundourakis G.[1], Skoulakis A. [1], Clark E.L. [1], Kaselouris E. [1], Y. Orphanos[1,3], J. Chatzakis[1,2], Fitilis I.[1,2], Bakarezos M.[1,3], Dimitriou V.[1,3], Papadogiannis N.A.[1,3] and M. Tatarakis[1,2]

[1]*Institute of Plasma Physics & Lasers - IPPL, Hellenic Mediterranean University Research Centre, 74100 Rethymno, Greece*
[4]*Department of Electronic Engineering, Hellenic Mediterranean University, 73133 Chalepa, Chania, Greece*
[3]*Department of Music Technology and Acoustics, Hellenic Mediterranean University, 74133 Perivolia, Rethymno, Greece*

g.tazes@chania.teicrete.gr

1. INTRODUCTION

Laser-induced charged particle accelerators have attracted the interest of the scientific community due to their numerous applications that are directly connected to human quality of life. Energy production by Inertial Confinement Fusion – ICF, specifically the ion driven Fast Ignition – FI [1,2] scheme, offer the possibility of energy production, clean of nuclear wastes that uses as a fuel Hydrogen isotopes. Hadron therapy [3,4] is possible due to the protons and electrons *Bragg peak*, that allows the energetic protons and ions to focus and damage tissue targets, allocated deep under the body skin, while the organic surroundings remain safe. High energy electrons are used for X-rays generation by synchrotron and betatron radiation for medical purposes. Conventional accelerators have already achieved charge particle acceleration in extreme energies while ultra-intense lasers offer the compelling alternative of developing compact and affordable tabletop laser-plasma particle accelerators. The state of the art in proton acceleration is 85*MeVs* by F. Wagner et.al [8] performing Target Normal Sheath Acceleration – TNSA [5-7] on sub-micrometer thick, using a combined Ti:sapphire Nd:glass laser system of 500*fs* pulse duration with an intensity of $10^{20}W/cm^2$. I. Jong Kim et. al. [9] accelerated proton with 93*MeVs* energy by using 30*fs* duration, circularly polarized laser pulse with intensity 6 $10^{20}W/cm^2$ interacting with a 15*nm* thick polymer target. For those laser-target parameters, the dominant acceleration mechanism, beyond charge separation, is the Radiation Pressure Acceleration – RPA [10]. While electrons of GeV energies have been achieved by Laser Wakefield Acceleration – LWFA.
Typically for TNSA, proton energies scale as $(I\lambda^2)^{1/2}$, where I is the laser intensity in W/cm^2 and λ is the laser wavelength in μm. To date, there are several *PW* laser facilities around the world although the available laser intensities to accelerate protons in the required energies are not yet available. Ti:sapphire lasers commonly suffer from the laser systems inherent Amplified Spontaneous Emission – ASE prepulse, that may deform or destroy the target *ns* before the main pulse arrives, suppressing the TNSA mechanism[11]. In laser-solid target interaction experiments, there is the need for replacing and repositioning the target and after every laser shot. This prosses can take up several minutes and so forth prohibits the possibility of high repetition rate laser-induced ion/proton sources. Additionally, solid targets are the source of debris that can damage the optics inside the vacuum chamber.

2. IPPL EXPERIMENTAL RESULTS

Proton acceleration experiments were performed with the 45*TW* laser system ZEUS. During these experiments, a parametric scan of target widths and pulse durations were performed to maximize the accelerated protons cut-off energies and populations. The main diagnostic for energetic protons were CR39 nuclear track detectors accompanied by a multisector filter mask. CR39, is a transparent plastic polymer allyl diglycol carbonate. It is an ideal detector for measuring ions and protons, while it is not sensitive to electrons and x-rays. When a proton or ion of certain energy deliver most of its energy on the surface of a CR39 it will cause localized damage and forming a crater. For this crater to become visible, CR39 must be chemically etched. To do so the CR39 is placed into a bath of 30% *w/v* Sodium Hydroxide solution heated to the temperature of 90° C for 3 hours. This process, dissolves the damaged plastic, broadening the size of the formed pits, making them visible to the naked eye. The pits formed by protons will grow to a size of 10μm in diameter while other ions will create larger pits. The sectors of the filter mask were ranging from widths of 13 μm to 104μm of Al foil. The mask is used as a filter of low energy protons. When a proton beam with a broad spectrum of energies passes through the mask, each sector filters out deferent low energy protons. The thinner sector will filter out the lowest energy protons while each consecutive sector will filter increasingly higher energy protons. Protons of specific energy will pass through the mask and deliver their energy exactly at the surface of the CR39. Figure 1 presents a schematic representation of the CR39 diagnostic while Figure 2 presents the scanned CR39 with the optimum experimental results of accelerated protons. To measure the accelerated electrons during the solid target irradiation, a stack of Radiocromic films along with a filter for the laser IR light were used.

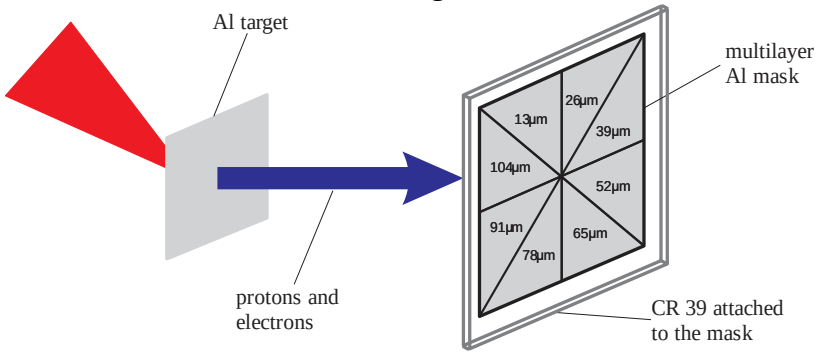

Figure 1: Schematic representation of the multisector filter mask – CR39 diagnostic.

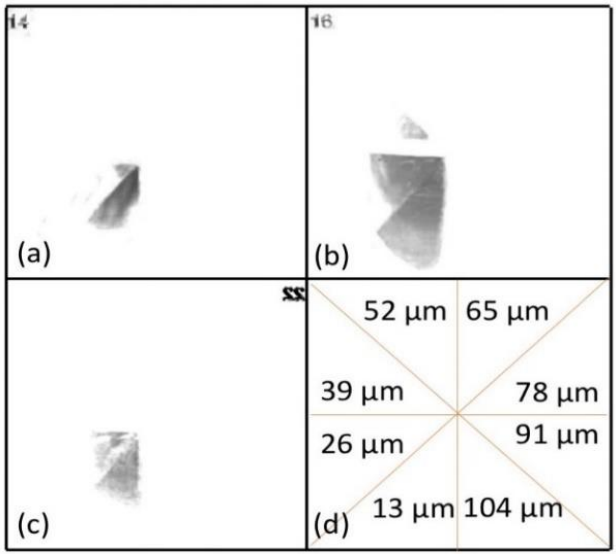

Figure 2: The scanned CR39 of the shots with the best results. (a) 70μm aluminum target irradiated by 25fs pulse with cut off proton energy 1.5MeV. (b) 30μm aluminum target, 80fs pulse, cut off proton energy 2MeV. (c) 30μm aluminum

target, 150fs pulse, cut off proton energy 1.5MeV. (d) Schematic representation of the thicknesses of the different sectors of the aluminum filter mask.

Figure 3 shows a schematic representation of the RCF diagnostic for measuring electrons while Figure 4 presents the electron dose in consecutive RCF and the minimum energy required for an electron to penetrate to that depth. Each RCF have 110μm thickness.

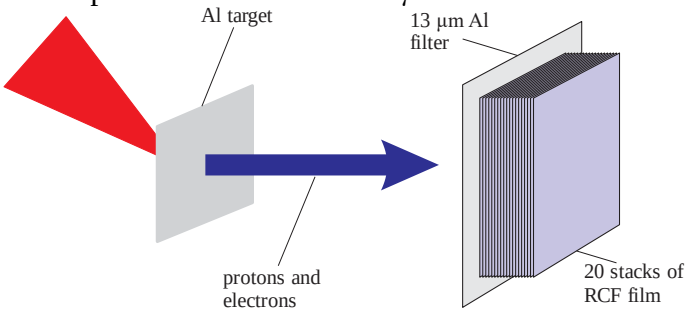

Figure 3: The RCF diagnostic for measuring dose from electrons.

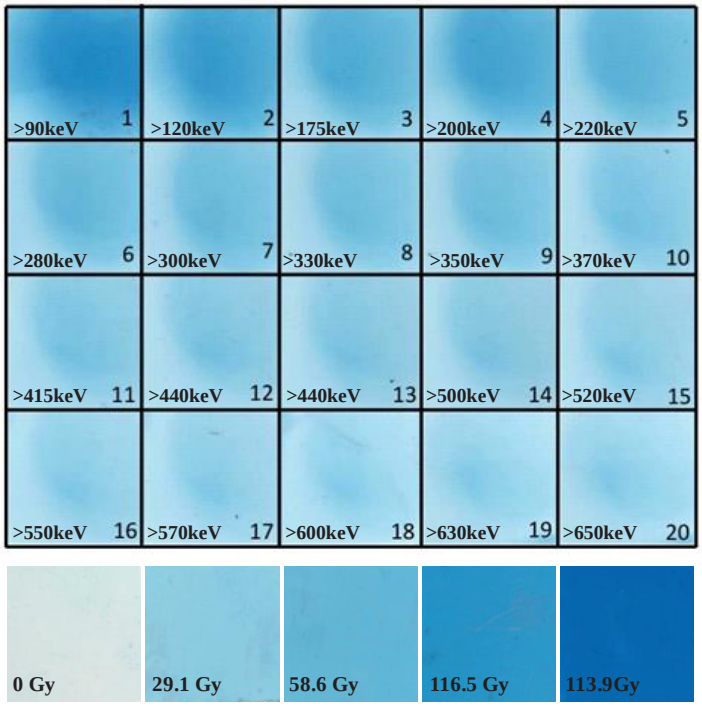

Figure 4: The dose on the 20 consecutive RCF films. On each film the minimum energy that can penetrate up to its depth appears. Below, the calibrated RCF films with their corresponding doses

3. PARTICLE-IN-CELL SIMULATION RESULTS

PIC simulations were performed using EPOCH [12] code for CPU parallelization and PIConGPU [13] code for GPU parallelization. PIC algorithms couple the Maxwell equations with the Vlasov equation that describes the temporal evolution of the distribution function of plasma. In order to have reliable results free of numerical errors such as numerical heating, the following criteria must be resolved.

$$\delta t < 1/\omega_{pe}\,, \qquad \delta x < \varsigma \lambda_{De}$$

Where δt is the simulation time step, ω_{pe} is the electron plasma frequency, δx the cell size of the simulation, λ_{De} is the plasma debye length and ς is a factor that varies based on the particle shape function. PIC codes use macroparticles which represent a huge number of real particles, acting collectively. Increasing the number of macroparticles in a simulation will result in each macroparticle to correspond to a lower number of real particles. A convergence test must be

performed that the number of macroparticles in the simulation will be consecutively increased until the energy spectra results converge to the same values, indicating that the simulation is free of numerical heating. Figure 5 presents the execution time for each simulation as a function of number of macroparticle per cell per species – N_{ppc} and the order of particle shape functions for both EPOCH and PIConGPU.

PIC simulations are extremely computationally demanding and require high degree of parallelization. Higher number of CPUs or GPUs tends to dramatically decrease the required execution time. Further Increase of the CPUS or GPUs, beyond a certain number that is based on the total number of nodes of the simulation domain, will lead to a plateau or even slowdown due to the reduction of the efficiency of the Massage Passing Interface (MPI) communication. The cores will need more time to exchange the information than to perform the calculations. Figure 6 presents simulation execution time as a function of the number of CPUs used for EPOCH and the GPUs used for PIConGPU. For more than 400 CPUs and 16 GPUs a plateau appears on the code's performance.

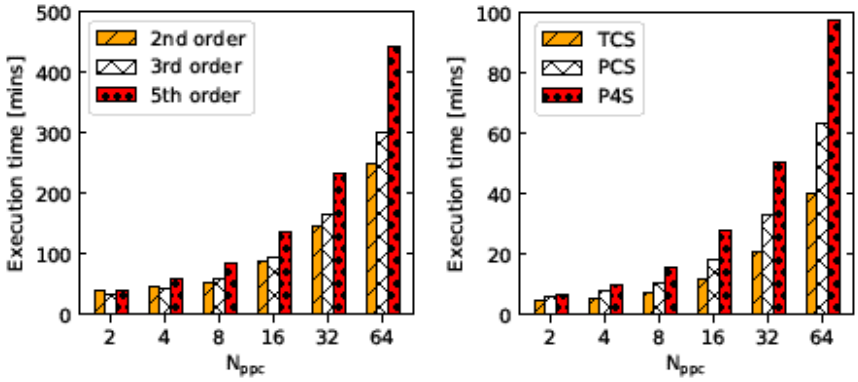

Figure 5: Simulation execution time as a function of number of macroparticles per cell per species – N*ppc* and order of particle shape functions for EPOCH using 400 CPUs (Left) and PIConGPU (right) using 16 GPUs [14].

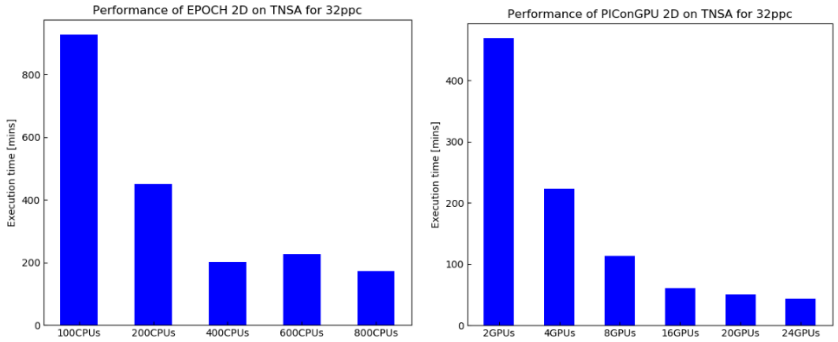

Figure 6: Simulation execution time as a function of number CPUs for EPOCH (Left) and GPUs for PIConGPU (right) [14].

In Figure 7 the proton density of the target contamination layer at 225*fs* of the simulation is presented for both Codes. The proton acceleration takes place in the rear of the targets due to TNSA charge separation and in the front of the target due to the mechanism of Collisionless Electrostatic Shock – CESA [15]. Figure 8 presents the accelerated proton energies as well as the electron energies at deferent times of interest and the electron Temperatures. According to Moras model [16-18] the Protons cut-off energies can be analytically calculated by the electron temperature.

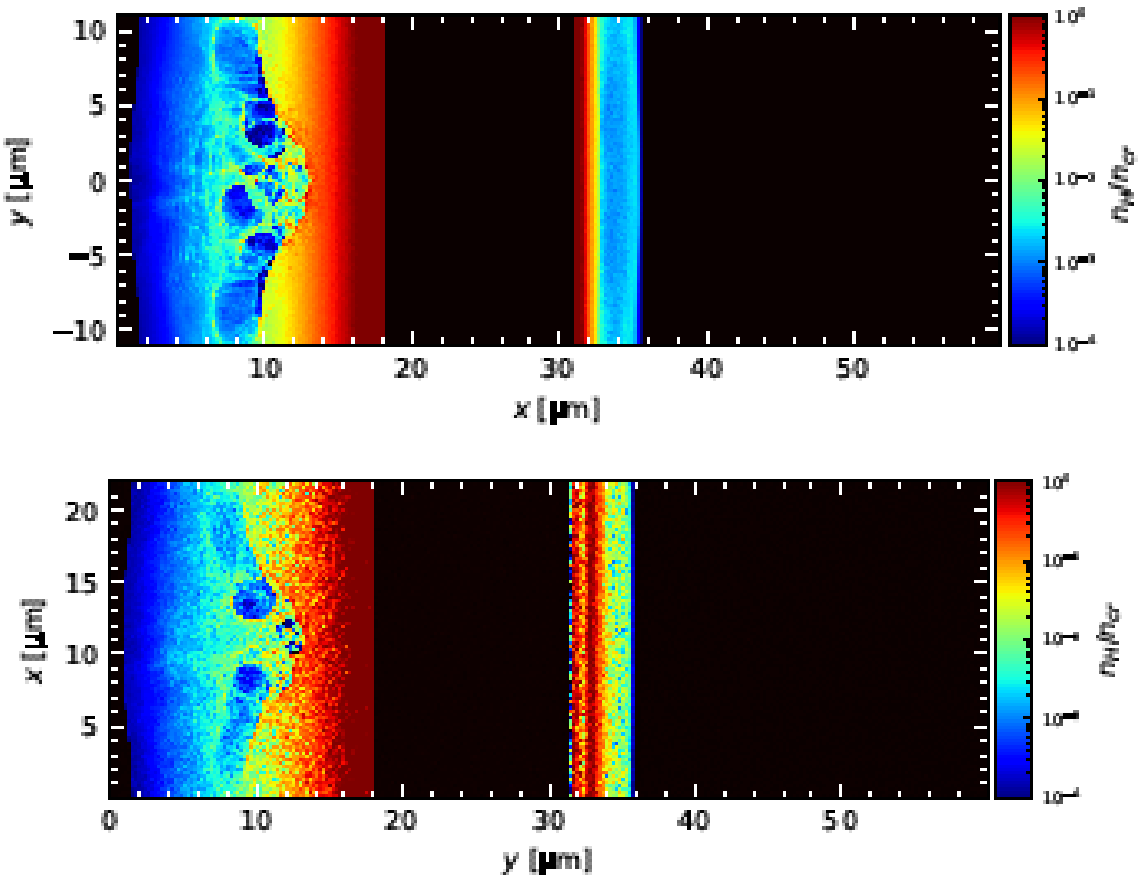

Figure 7: proton density of the target *contamination* layer at 225*fs* of the simulation for EPOCH (top), PIConGPU (bottom) [14].

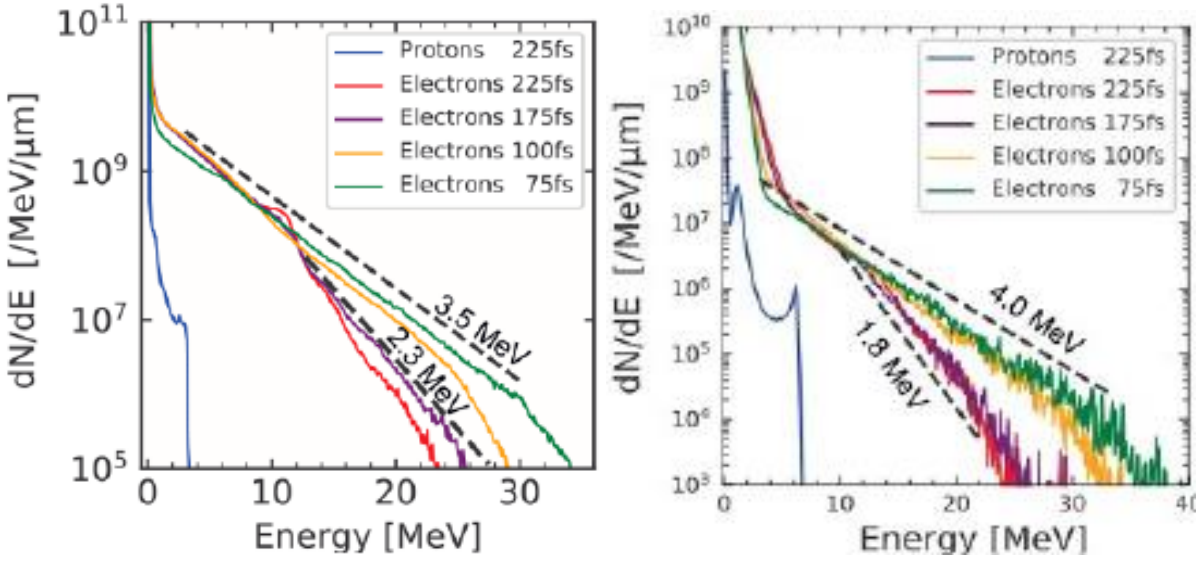

Figure 8: Energy spectra of protons for 225fs of the simulations and electrons for different times of interest for EPOCH (left) and PIonGPU (right). The dashed black line shows the electron temperature [14].

PIC simulations were performed for electron acceleration through the Laser Wake Field Acceleration – LWFA techniques for the 100TW laser system of ELI-NP. The proton density, energy spectra and execution time as a function of N_{ppc} and order of particle shape function are presented in Figure 9.

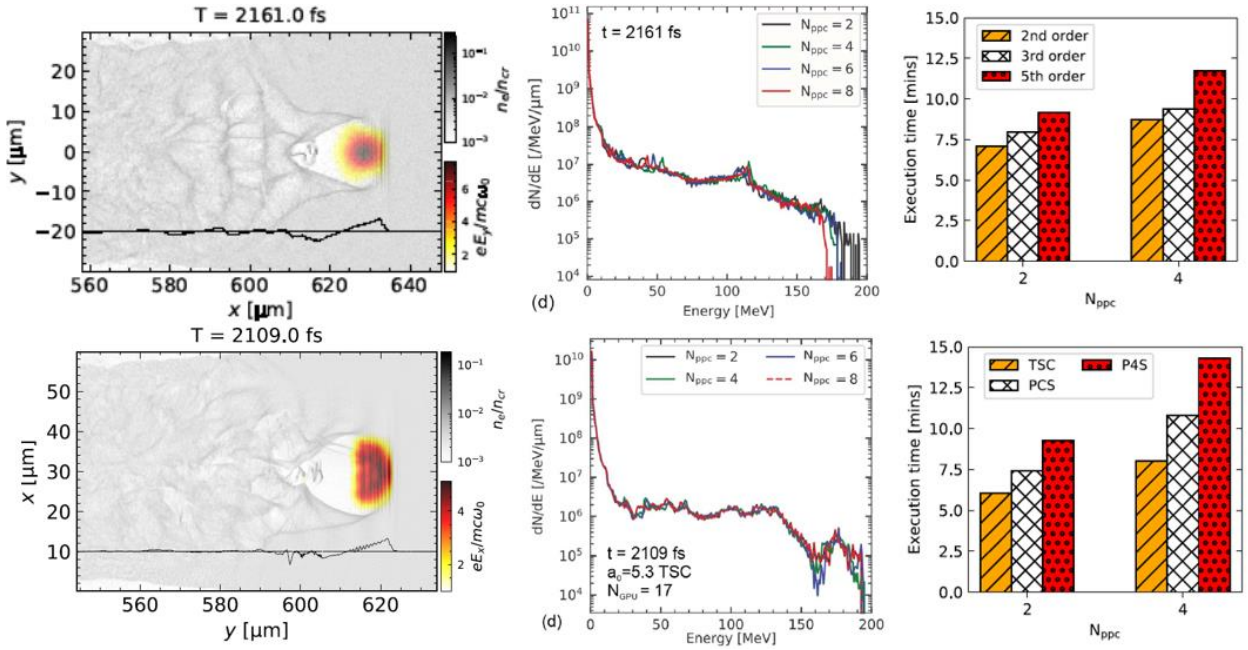

Figure 9: PIC simulations of LWFA for the 100TW laser system of ELI-NP. The proton densities (Left), electron energy spectra (middle) and execution time as a function of N_{ppc} and order of particle shape function (right) For EPOCH (top) and PIConGPU (bottom) [14].

4. FUTURE WORK AND DISCUSSION

In order to achieve high repetition rate proton sources, solid targets must be replaced with extremely high-density profiles. While solid densities of $n > 30n_{cr}$ where n_{cr} is the critical density ($n_{cr} = 1.7 \times 10^{21}/cm^3$ for wavelength λ=800nm) high-pressure gas-jets can deliver densities $n{\sim}10^{20}/cm^3$ which is far from the over-dense regime of the solid targets but close to the near-critical density regime. In the near-critical density regime, new proton acceleration mechanisms emerge, like the Magnetic Vortex Acceleration – MVA [19]. CESA exists in the overdense regime but it is more efficient in the near-critical density regime.

In order to further increase the density of the high-pressure gas-jet to values closer to the n_{cr}, a novel method has been proposed. This method suggests the tailoring of the density profile of the gas-get, with a secondary pre-successor pulse. These pulses will generate Sedov type Blast Waves – BWs inside the gas density profile [20,21]. The propagating, steep density gradient boundary of the BW will reach densities many times greater of the initial unperturbed gas density and will locally act as a solid target. The main TW pulse will then interact with the boundary of the BW where the proton acceleration will take place via MVA and CESA mechanisms. This will allow for high repletion rate proton sources, without the need of replacing and repositioning a solid target after each shot and without the debris that are generated during the interaction with solid targets that can damage the optics inside the chamber.

Figure 10 presents the core principle behind the Sedov BW tailoring of the gas target and the interaction of the main pulse with the BWs boundary. Figure 11 presents the preliminary results of MVA performed with EPOCH code. The energy spectra suggest proton energy enchancement compared to the TNSA numerical and experimental results.

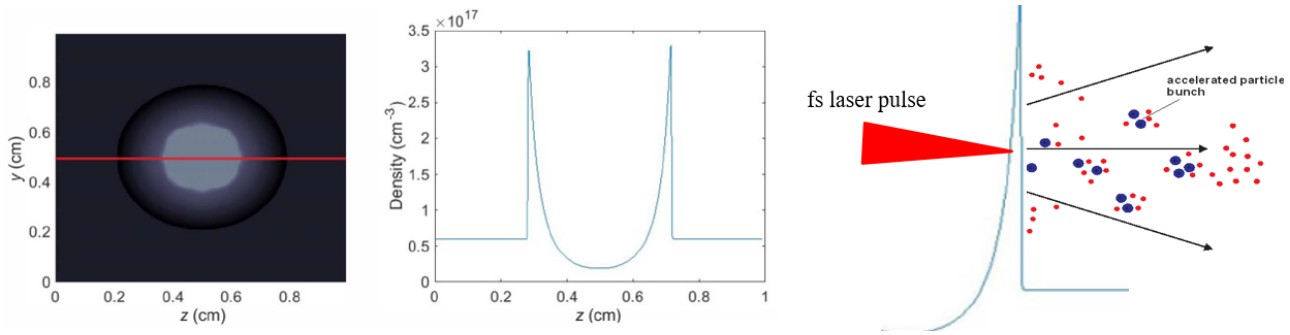

Figure 10: Base principal of the density profile tailoring with secondary pre-successor pulses, performed for CO_2 lasers [20]. The same principal can be applied for higher density for Ti:Sapphire lasers (left). The interaction of the TW, 25fs main pulse with the boundary of the Blast Wave (right)

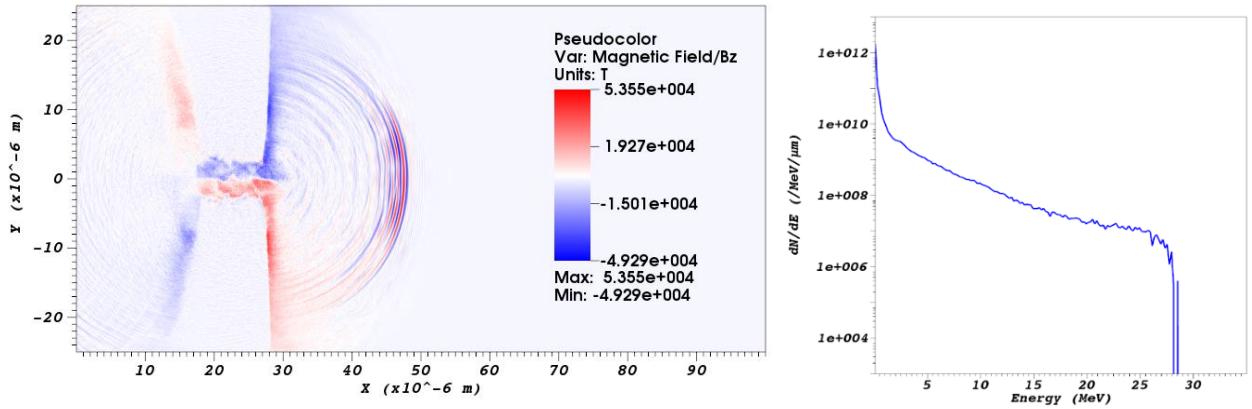

Figure 11: Plot of the azimuthal magnetic field that indicates the existence of MVA mechanism (left). Proton energy spectra that suggest cut-off energy enhancement in comparison with TNSA.

5. ACKNOWLEDGMENT

Part of this work has been performed under the Project HPC-EUROPA3 (INFRAIA-2016-1-730897), with the support of the EC Research Innovation Action under the H2020 Programme. This work is partially based on COST Action TUMIEE, supported by COST (European Cooperation in Science and Technology). IPPL Authors acknowledge the support of this work by the project 'ELI - LASERLAB Europe Synergy, HiPER & IPERION-CH.gr' (MIS 5002 735) which is implemented under the Action 'Reinforcement of the Research and Innovation Infrastructure', funded by the Operational Programme 'Competitiveness, Entrepreneurship and Innovation' (NSRF 2014-2020) and co-financed by Greece and the European Union (European Regional Development Fund). This work was supported by computational time granted from the Greek Research & Technology Network (GRNET) in the National HPC facility ARIS under project ID pr007 020 LaMIPlaS-II. ELI-NP Authors acknowledge the partially support of this work by the Extreme Light Infrastructure Nuclear Physics (ELI-NP) Phase II, a project co-financed by the Romanian Government and the European Union through the European Regional Development Fund the Competitiveness Operational Programme (1/07.07.201 6, COP, ID 1334). The EPOCH code was developed under the UK EPSRC grants EP/G054 950/1, EP/G056 803/1, EP/ G055 165/1 and EP/ M022 463/1. We acknowledge A. Huebl and all further contributors to the open-source code PIConGPU for enabling our simulations.

6. REFERENCES

[1] Betti, R., and O. A. Hurricane. "Inertial-confinement fusion with lasers." *Nature Physics* 12.5 (2016): 435.

[2] Roth, M., et al. "Fast ignition by intense laser-accelerated proton beams." *Physical Review Letters* 86.3 (2001): 436

[3] Linz, U., & Alonso, J. (2007). What will it take for laser driven proton accelerators to be applied to tumor therapy?. *Physical Review Special Topics-Accelerators and Beams*, *10*(9), 094801

[4] Malka, Victor, et al. "Practicability of protontherapy using compact laser systems." *Medical physics* 31.6 (2004): 1587-1592.

[5] Clark, E. L., et al. "Energetic heavy-ion and proton generation from ultraintense laser-plasma interactions with solids." *Physical Review Letters* 85.8 (2000): 1654.

[6] Clark, E. L., et al. "Measurements of energetic proton transport through magnetized plasma from intense laser interactions with solids." *Physical Review Letters* 84.4 (2000): 670.

[7] Tatarakis, M., et al. "Plasma formation on the front and rear of plastic targets due to high-intensity laser-generated fast electrons." *Physical review letters* 81.5 (1998): 999.

[8] Wagner, F., et al. "Maximum proton energy above 85 mev from the relativistic interaction of laser pulses with micrometer thick ch 2 targets." *Physical review letters* 116.20 (2016): 205002.

[9] Kim, I. Jong, et al. "Radiation pressure acceleration of protons to 93 MeV with circularly polarized petawatt laser pulses." *Physics of Plasmas* 23.7 (2016): 070701.

[10] Robinson, A. P. L., et al. "Radiation pressure acceleration of thin foils with circularly polarized laser pulses." *New journal of Physics* 10.1 (2008): 013021.

[11] Kaluza, Malte, et al. "Influence of the laser prepulse on proton acceleration in thin-foil experiments." *Physical review letters* 93.4 (2004): 045003.

[12] Arber, T. D., et al. "Contemporary particle-in-cell approach to laser-plasma modelling." *Plasma Physics and Controlled Fusion* 57.11 (2015): 113001

[13] Bussmann M *et al* 2013 Radiative signatures of the relativistic kelvin-helmholtz instability *Proc. of the Int. Conf. on High Performance Computing, Networking, Storage and Analysis*, ser. SC '13 New York, NY, USA p 5:1–5:12 ACM

[14] Tazes, I., et al. "Target normal sheath acceleration and laser wakefield acceleration particle-in-cell simulations performance on CPU & GPU architectures for high-power laser systems." *Plasma Physics and Controlled Fusion* 62.9 (2020): 094005.

[15] Silva, Luís O., et al. "Proton shock acceleration in laser-plasma interactions." *Physical Review Letters* 92.1 (2004): 015002

[16] Mora P 2003 Plasma expansion into a vacuum *Phys. Rev. Lett.* **90** 185002

[17] Mora P 2005 Thin-foil expansion into a vacuum *Phys. Rev.* E **72** 056401

[18] Mora P 2005 Collisionless expansion of a gaussian plasma into a vacuum *Phys. Plasmas* **12** 112102

[19] Park, Jaehong, et al. "Ion acceleration in laser generated megatesla magnetic vortex." *Physics of Plasmas* 26.10 (2019): 103108.

[20] Passalidis, Stylianos, et al. "Hydrodynamic computational modelling and simulations of collisional shock waves in gas jet targets." *High Power Laser Science and Engineering* 8 (2020).

[21] Marquès, J-R., et al. "Over-critical sharp-gradient plasma slab produced by the collision of laser-induced blast-waves in a gas jet; Application to high-energy proton acceleration." *arXiv preprint arXiv:2009.14770* (2020).

NEW TRENDS IN PLASTIC RECYCLING FOR 3D PRINTING

Bolanakis, N[1], Driukas, A[2], Kalderis, D[1], and Maravelakis, E[1]

[1]Hellenic Mediterranean University, Chania, Crete, Greece
[2]Gediminas Technical University, Vilnius, Lithuania
bolanakis@hmu.gr

ABSTRACT

Plastic is currently one of the most popular materials from which various products are made. This material is also used in the manufacture of household goods, clothing, technical details, and even medical devices. Global demand for plastics is growing rapidly and in 2018, about 359 million metric tons were produced. However, plastic has also a major effect on global pollution and many countries and global organizations have already started legislative actions and initiatives for reducing plastic consumption as well as for recycling plastic waste.

Additive manufacturing, or otherwise known as 3D printing, has a very high potential to gain a foothold in the global market as its application in various fields is expanding. Nowadays, new studies present alternative uses of plastic waste, focused on 3D printing. This technique includes shredders, for cutting the plastic waste to small pieces and an extruder in order to melt the plastic and produce 3Dprinting filament. Furthermore, the effect of adding additional carbon-based additional material, such as biochar is been researched. In this paper, we will present a short review with the latest trends in plastic recycling for 3D printing.

INTRODUCTION

Plastic is everywhere in our daily lives. In just a few decades it has managed to establish itself and is now a key ingredient in a huge variety of objects and materials due to its characteristics (it is flexible, durable and lightweight) and its low price. Because much of it is used to make a wide variety of disposable packaging, plastic is the perfect symbol of the wasteful lifestyle that characterizes our time. Improper or no management of plastic waste can result in a huge source of environmental pollution.

3D printers brought a great revolution in the field of plastic use, which with their low cost can be in every home now. This, of course, resulted in an increase in the volume of plastic waste from them and the need for substantial recycling of plastic and its reuse in its original form or even with the use of bio-impurities and the creation of new printing materials with new properties.

PLASTICS RECYCLING FOR 3D PRINTING

Biopolymer, is a non-toxic and biocompatible and so pet this material has become increasingly applicable in 3D printing over the last 10 years. A group of scientists selected beeswax and gum rosin as additives for the production of filaments from polycaprolactone. They produced a new environmentally biocompatible friendly material (Queiroz & Collares-Queiroz, 2009; Arrieta, 2017). It is very important to mention that, they could be used to make surgical instruments, medical devices and prosthetic parts (Cristina Pavon, 2020) due to their biocompatibility and antimicrobial properties.

In view of the current global contamination of plastic products, a group of students from the Indian Academy of Sciences studied the physical and mechanical properties of a filament made

from recycled high-density polyethylene (HDPE) and polypropylene (PP) blended with active carbon extracted from coconut fiber waste. Active carbon was chosen for research because it is not a widely studied additive for polymers such as HDPE and PP. The study had to show whether active carbon due to its high specific surface area can improve the plasticity and elongation of filaments during fracture (Chong S C. H., 2015; Kreiger M A, 2014; Chong S P. G., 2017).

In response to the current global situation regarding the current Covid-19 pandemic, a team of scientists from Mashhad University of Medical Sciences decided to encourage the use of 3D printed splints. As the current emergency situation forced the minimization of patient-physician contact time, a great opportunity opened up for the wider application of 3D printed casts. Fiberglass casts require significantly more contact between the patient and the physician, as its removal requires follow up where in the meantime the conventional plaster cast can be removed by the patient himself using water and scissors (Hoogervorst P, 2019). This is why the wider use of 3D printed casts would allow the required splint to be ordered at a distance and would reduce the frequency of potential contact. Also, 3D printed casts are washable not like conventional casting and this makes them easier to use in situations like now.

A device for the production of filament from recyclable plastic was developed in the Design, Manufacturing & Automation Laboratory at Hellenic Mediterranean University. The results of the device were remarkably good during the initial setup of the device filament produced was within the limits given by the manufacturer, that is 1.71mm (Figure 1), the filament trade is 1.75mm ± 0.05mm.

Figure 12: New filament from plastic waste at 1.71mm diameter

INTRODUCTION TO BIOCHAR

According to the International Biochar Initiative, biochar is defined as a solid material produced by the carbonization of biomass. The term "carbon black" is often used interchangeably with the term "biochar" (Figure 2). Biochar is a carbon-rich material, but its content of nutrients such as nitrogen, phosphorus and potassium is low. The key element of biochar is carbon but it contains hydrogen, oxygen and ash. Due to its good characteristics such as specific surface area, porosity, surface functional groups as well as the fact that it is a cheap and environmentally friendly material, biochar has gained a lot of attention in dealing with many environmental problems, including environmental restoration, greenhouse gas emission minimization, waste management and energy production. However, it can be used to remove heavy metals but also to adsorb organic and inorganic pollutants.

Figure 13: Various forms of Biochar

During pyrolysis, 3 types of products are produced, solid, liquid and gas. Specific conditions are required during the cracking process to produce high-yield biochar. Biochar is added to soils with the intention of improving its properties and reducing greenhouse gas emissions. Biochar is produced by the thermal decomposition of organic materials in conditions where there is no oxygen or it is limited and at relatively low temperatures. This process is reminiscent of the way coal is produced but differs from the production of similar materials because biochar is produced in order to be added to the soil as a means of improving soil performance, retaining nutrients from the water that penetrates the soil, and will offer carbon storage. Ertane E, 2018, published a paper that studied the wear behavior of bio-enhanced PLA filament (Figure 3). The results of his study showed that Biochar was successfully integrated into the PLA. Four different filaments using PLA with different amounts of loading levels of biochar were produced. Homogeneous distribution was achieved with the biochar and the filaments. Using the FDM 3D printer was created four samples with a 24mm diameter and 7.8mm height with different proportions of biochar filaments. The biochar - PLA applications are envisaged in the aerospace industry, etc. PLA and biochar are available in natural resources.

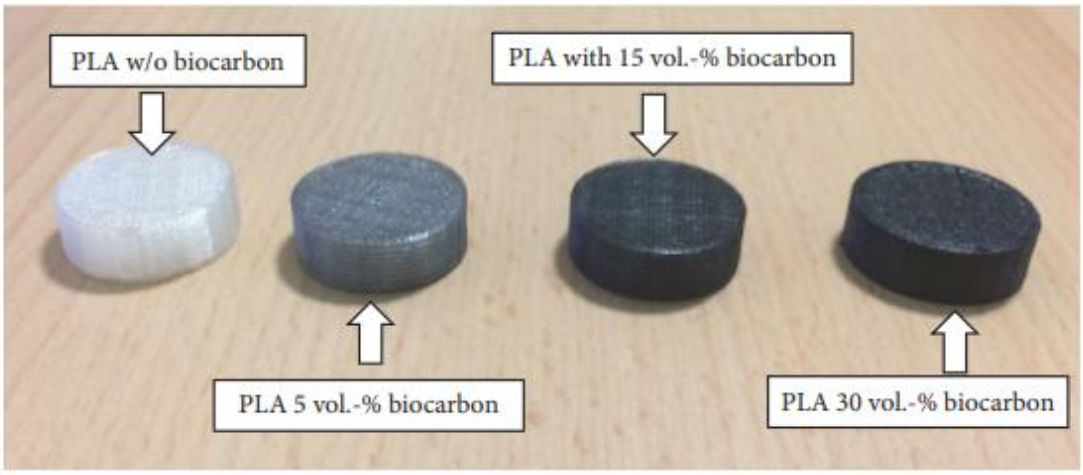

Figure 14: 3D printed Biopolymers with different biochar content.

ADDING BIOCHAR IN PLASTIC 3D PRINTING MATERIAL

Additive manufacturing, or otherwise known as 3D printing, has a very high potential to gain a foothold in the global market as its application in various fields is expanding. Nowadays, new studies present alternative uses of plastic waste, focused on 3d printing. This technique includes shredders, for cutting the plastic waste to small pieces and an extruder in order to melt the plastic and produce 3d printing filament (Figure 4). Furthermore, the effect of adding additional carbon-based additional material, such as biochar is been researched.

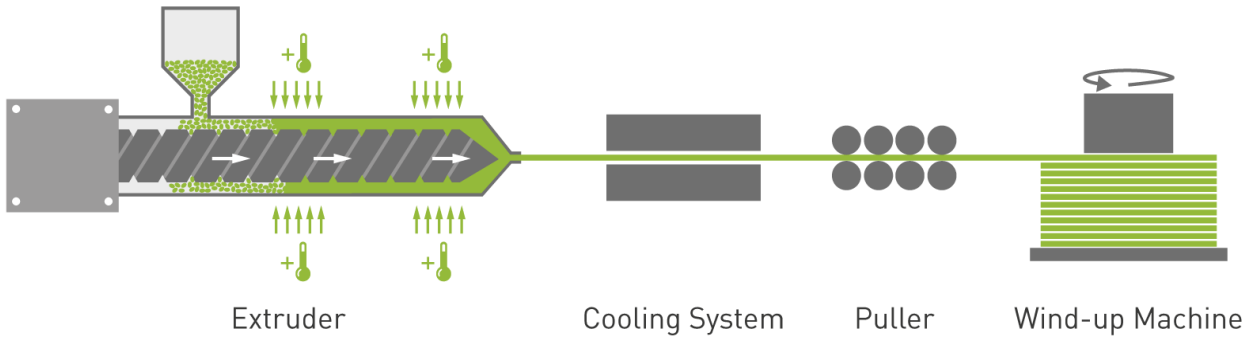

Figure 15: Extruder machine for plastic pellets (Profiles & Filaments Extrusion, NUREL Biopolymers)

More specifically, the biochar is created by the incineration of household waste (eg fruit peels, shells, etc.). The plastic waste (eg PET bottles) placed in a shredder and cut. After the crumbs of the plastic are placed in an oven after the biochar has been added on top of them and they are heated and created by the shrinkage of the plastic spherical objects of plastic-biochar. Finally, after coming to room temperature, they are placed on the extruder and using a metal screw are pushed to the top of the device, which at the same time melts at 200 – 250^{o}C and finally, the material passes through the nozzle with a diameter of 1.75mm to create the new filament (Figure 5).

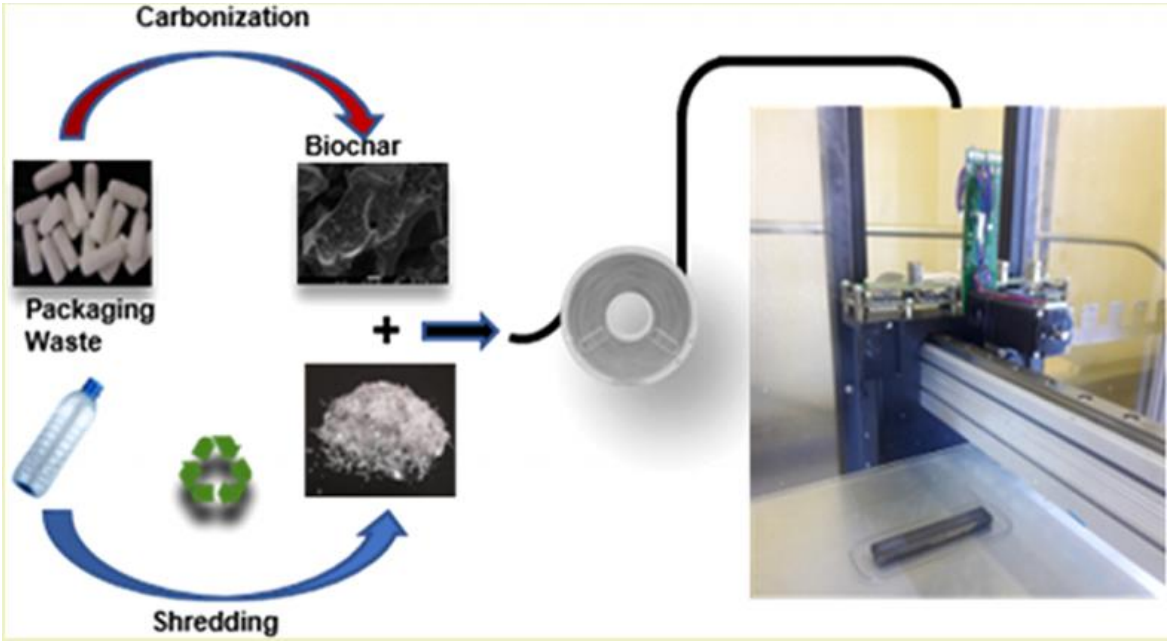

Figure 16: Schematic of composite fabrication (Idrees M., et. al, 2018)

Idrees M, et. al, 2018, use the above method to study the mechanical and thermal behaviors of such an admixture. In his work he states that this new material was successfully ejected from the 3D printer. Biochar had excellent properties in terms of texture and graphiziation. The incorporation of biochar has improved the mechanical, thermal and dynamic properties of 3D printed parts and can serve as a possible alternative to commercial graphene materials in polymer composites.

CONCLUSIONS & FUTURE RESEARCH

The use of biochar with recycled plastic opens new avenues in the 3D printing industry. Of course, more research is needed in terms of materials (eg ABS, PETG) but also household waste targeted at natural products of each place. An additional idea for a future study is the use of biochar in resin printers. In the first level to observe if you integrate the biochar with the resin in order to print successfully and in the second level to study the thermal, mechanical and biocompatible properties of the new materials that will result from their printing.

REFERENCES

1. Ahmad M., Lee S.S.., Dou X., Mohan D., Sung J.K., Yang J.E. and Ok Y.S., Biochar as a sorbent for contaminant management in soil and water
2. Arrieta, M. S.-L. (2017). Combined Effect of Linseed Oil and Gum Rosin as Natural Additives for PVC. Ind. Crops Prod, 196–204.
3. Ashkan Sedigh, e. a. (2020). Safety and Efficacy of Casting during COVID-19 Pandemic: A Comparison

of the Mechanical Properties of Polymers Used for 3D Printing to Conventional Materials Used for the Generation of Orthopaedic Orthoses. ARCHIVES OF BONE AND JOINT SURGERY, 281-285.

4. Beneficial role of Nano silica in cement-based materials – A review. L. P. Singh, S. R. Karade, S. K. Bhattacharyya, M. M. Yousuf, S. Ahalawat India 2013, Science Direct
5. Blaya F, P. P. (2018). Design of an orthopedic product by using additive manufacturing technology: the arm splint. J Med Syst. , 54.
6. Chemical composition and pulping of date palm rachis and Posidonia Oceanica – A comparison with other wood and non-wood fibre source. R. Khiariab, M. F. Mhennia, M. N. Belgacemb, E. Mauretb 2009, Science Direct
7. Chen, T., Zhang, Y., Wang, H., Lu, W., Zhou.ZhangY.Ren, L., 2014. Influence of pyrolysis temperature on characteristics and heavy metal adsorptive performance of biochar derived from municipal sewage sludge. Bio resource Technology. Article in Press.
8. Chong S, C. H. (2015). Design for 3D Printing. Chem. Eng. Trans., 1669-1674.
9. Chong S, P. G. (2017). Physical characterization and pre-assessment of recycled high-density polyethylene as 3D printing material. J. Polym. Environ, 136–145.
10. Cristina Pavon, M. A.-M. (2020). New Materials for 3D-Printing Based on. polymers.
11. Effect of mixing proportion on the properties of seaweed modified sustainable concrete. Md Nurul Islam Siddique, Zularisam bin Abd Wahid Malaysia 2017, aip.scitation.org
12. Ertane, E. G., Dorner-Reisel, A., Baran, O., Welzel, T., Matner, V., & Svoboda, S. (2018). Processing and wear behaviour of 3D printed PLA reinforced with biogenic carbon. Advances in Tribology, 2018.
13. Goldberg (1985). Black Carbon in the Environment. Wiley, New York. Geological Journal. 21
14. Hoogervorst P, K. R. (2019). A biomechanical comparison of fiberglass casts and 3-dimensional-printed, open-latticed, ventilated casts. Hand .
15. Hossain, M.K Strezov, V., Chan K.Y., Ziolkowski, A., Nelson, P.F., 2011. Influence of pyrolysis temperature on production and nutrient properties of wastewater sludge biochar, Journal of Environmental Management.
16. Hossain, M.K., Strezov, V., Nelson, P.F. 2009. Thermal characterization of the products of wastewater sludge pyrolysis. Journal of Analytical and Applied Pyrolysis.
17. Idrees, M., Jeelani, S., & Rangari, V. (2018). Three-dimensional-printed sustainable biochar-recycled PET composites. ACS Sustainable Chemistry & Engineering, 6(11), 13940-13948.
18. Inyang, M., Gao, B., Yao, Y., Xue, Y., Zimmerman, A.R. , Pullammanappallil, P., Cao, X., 2012. Removal of heavy metal; from aqueous solution by biochars derived from anaerobically digested biomass. Bioresource Technology
19. Jakubus M. and Czekała J., Heavy Metal Speciation in Sewage Sludge, Pol. J. Environ.

20. Khiari B., Marias F., Zagrouba F., Vaxelaire J., Analytical study of the pyrolysis process in a wastewater treatment pilot station, Desalination 167
21. Kreiger M A, M. M. (2014). Life cycle analysis of distributed recycling of post-consumer high density polyethylene for 3-D printing filamen. J. Clean. Prod., 90-96.
22. Lehmann J., (2007). Bio-energy in the black. Frontiers in Ecology and the Environment.
23. Lehmann J., Joseph S., (2015). Biochar for Environmental Management. Science, Technology and Implementation.
24. Lehmann, J., Joseph, S., 2009. Biochar for environmental management: An introduction. In: Lehmann J., Joseph, S. (Eds), Biochar for environmental management: science and technology. Earth scan, London.
25. Mechanical properties of Posidonia Oceanica fibers reinforced cement. L. Allegue, M. Zidi, S. Sghaier 2014, journals.sagepub.com
26. Pan G, C. S. (2018). The effects of iron, silicon, chromium, and aluminum additions on the physical and mechanical properties of recycled 3D printing filaments. Adv. Polym. Technol., 1176–1184.
27. Park, J.H., Choppola, G.K., Bolan, N.S., Chung, J.W., Chuasavathi, T., 2011. Biochar reduces the bioavailability and phytotoxicity of heavy metals.
28. Queiroz, A., & Collares-Queiroz, F. (2009). Innovation and Industrial Trends in Bioplastics. Polym. Rev., 65-78.
29. Schmidt M.W.I., Noack A.G., (2000). Black carbon in soils and sediments: Analysis, distribution, implications, and current challenges. Global Biogeochemical Cycles
30. Seaweed biopolymers as additives for unfired clay bricks C. A. Dove, F. F. Bradley, S. V. Patwardhan, Spingler Link
31. Siddique R., Naik T.R., (2004). Properties of concrete containing scrap-tire rubber - an overview. Waste Managment.
32. SIEWHUI CHONG, T. C.-K.-C.-F.-M.-T. (2020). Evaluation of the physico-mechanical properties of activated-carbon enhanced recycled polyethylene/polypropylene 3D printing filament. Sådhanå, 57.
33. Sontheimer H., Crittender J. C. and Summers R.S., Activated carbon for water treatment, Karlsruhe: DVGW-Forschungsstelle
34. Thermo physical characterization of Posidonia Oceanica marine fibers intended to be used as an insulation material in Mediterranean building. Ons Hamdaoui, Laurent Ibos, Atef Mazioud, Mohamed Safi, Oualid Limam2018, Science Direct
35. Ultimaker. (2020, 05 10). Ultimaker. Retrieved from The widest material choice on the market: https://ultimaker.com/materials
36. Wilbon, P. C. (2013). Progress in Renewable Polymers from Natural Terpenes, Terpenoids, and Rosin. Macromol. Rapid Commun, 8–37.

37. Yuan J.H., Xu R.K., (2011). The amelioration effects of low temperature biochar generated from nine crop residues on an acidic Ultisol. Soil Use and Management. 27

NEURAL NETWORK ESTIMATION OF THE ELECTROMAGNETIC FIELD SCATTERED BY A DIELECTRIC CIRCULAR CYLINDRICAL ROD IN CASE OF OBLIQUELY INCIDENT PLANE WAVES

Kapetanakis, T.N.[1], Baklezos, A.T.[1], Nikolopoulos, C.D.[1], Petrakis, N.[1], Konstantaras, A.[1], Ioannidou, M.P.[2], and Vardiambasis, I.O.[1] *

[1] Department of Electronic Engineering, Hellenic Mediterranean University
Chania, Crete, Greece

[2] Department of Information & Electronic Engineering, International Hellenic University
Thessaloniki, Greece

* ivardia@hmu.gr

1. INTRODUCTION

Soft computing techniques are biologically inspired techniques, Choudhury et al. (2015) and Kapetanakis et al. (2018a), suitable for complex problems requiring tedious and repeated analysis with fast and accurate convergence. They are classified into three main categories: the fuzzy logic systems (i.e. the adaptive neuro fuzzy inference system (ANFIS)), the artificial neural networks (i.e. the feed-forward back-propagation NNs) and the evolutionary algorithms. All these techniques have been widely used to effectively analyze and synthesize intensive nonlinear problems with extensive applications in telecommunication engineering, Liodakis et al. (2004) and Kapetanakis et al. (2021), chemical engineering, Vardiambasis et al. (2020), healthcare and medical diagnosis, Sergaki et al. (2018), geoscience and seismology, Konstantaras (2020), and many other scientific areas, so they are attractive for several electromagnetic wave propagation, radiation and scattering problems, Christodoulou and Georgiopoulos (2000), Devabhaktuni et al. (2001), Mishra (2001), Kapetanakis et al. (2012), Choudhury et al. (2015), Mishra et al. (2015), Kapetanakis et al. (2018a), Kapetanakis et al. (2018b). The biologically inspired artificial neural networks (NNs) mimick the human central nervous system and provide an efficient mean of simulating complex functions performed by the humans' brain. In particular, multi-layer perceptron neural networks (MLP-NNs) containing two or more hidden layers demonstrate the ability to approximate theoretically any non-linear function relating any pair of input and output data sets thereby reported in the literature as global approximators, Kapetanakis et al. (2018a), Kapetanakis et al. (2018b), and Kapetanakis et al. (2021), while the Levenberg–Marquardt (LM) and the Bayesian Regulation (BR) training algorithms are usually performing best as expected.

Electromagnetic scattering by cylindrical structures is an important problem with many applications in mobile communications, defense industry, geophysical exploration, remote sensing, and electromagnetic compatibility, such as simulation of complex bodies, target identification, biomedical imaging, control of the scattering cross-sections of several objects, communication inside tunnels, and remote sensing of pipelines or subsurface resources, Balanis (2012) and Ishimaru (2017).

Plane-wave scattering by two or more parallel, concentric or eccentric, conducting and/or dielectric, circular cylinders, at normal, Millar (1960), Olaofe (1970), Chang and Mei (1976), Hongo (1978), Uzunoglu and Fikioris (1979), Roumeliotis et al. (1980), Ragheb and Hamid (1985), Elsherbeni and Hamid (1987), Parrikar et al. (1991), Elsherbeni and Kishk (1992), Kishk et al. (1992), Kumar and Jain (1993), Roumeliotis and Kakogiannos (1994), Roumeliotis and Ziotopoulos (2000), or oblique incidence, Yousif and Kohler (1988), Tsalamengas et al. (1995), Stratigaki et al. (1996), Toyama and Yasumoto (2003), Vardiambasis et al. (2004), Osipov and Tretyakov (2017), has been treated by many researchers, using a variety of methods (separation of variables, moment

methods, integral equations, perturbational techniques). The most extensive study can be found in Konistis and Tsalamengas (1997), where scattering of obliquely incident waves from a bianisotropic cylinder enclosing other bianisotropic cylinders and placed in an unbounded bianisotropic space has been studied.

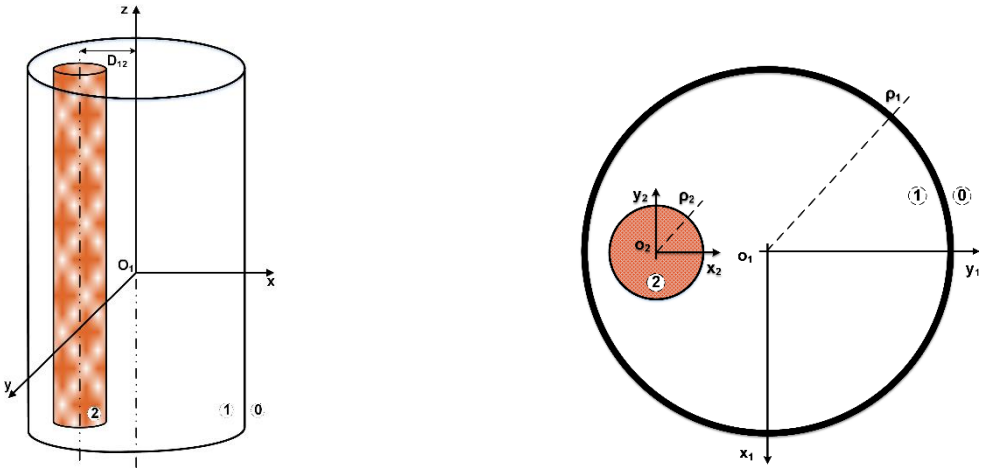

(a) (b)

Figure 1. (a) Geometry and (b) cross section of a circular cylindrical dielectric rod.

In this paper we use the analytical method applied in Konistis and Tsalamengas (1997) and Vardiambasis et al. (2004), in order to address the problem shown in Figure 1, of a dielectric circular cylinder (region 1) in free space (region 0) loaded by a parallel dielectric circular cylindrical rod (region 2). Each region i $(i=0,1,2)$ is identified through the corresponding dielectric constant ε_i, magnetic permeability μ_i, and electric conductivity σ_i. The radius of the cylindrical region l $(l=1,2)$ is denoted by α_l. The cylinders are parallel, with off-axis distance D_{12}. For the analysis we employ 2 cylindrical coordinate systems (one for each cylinder): $O_1(\rho_1,\varphi_1,z)$ for regions 0 and 1 and $O_2(\rho_2,\varphi_2,z)$ for region 2.

We consider an arbitrarily polarized plane wave, propagating in the external free space (region 0), and obliquely incident on the structure, as the primary excitation. Applying the generalized separation of variables method yields infinite series solutions for the scattered field in region i, consisting of Bessel and Hankel functions with unknown expansion coefficients. Then implementing the corresponding boundary conditions and using the translational addition theorems for Bessel and Hankel functions, results in an infinite linear algebraic system for the field expansion constants. Solving this system after truncation yields to analytical expressions for the scattered fields and the scattering cross-section of the structure of Figure 1.

2. ANALYTICAL SOLUTION OF THE SCATTERING PROBLEM

Assume a plane wave propagating inside free space (region 0), in the direction of

$$\bar{k}^{inc}(\theta',\varphi') = k_\rho \hat{k}_\rho^{inc} + \beta\hat{z} = k\sin\theta'\,(\cos\varphi'\,\hat{x} + \sin\varphi'\,\hat{y}) + k\cos\theta'\,\hat{z} \qquad [1]$$

where θ' and φ' are the angles of incidence shown in Figure 2, $\beta = k\cos\theta'$ and $k_\rho = k\sin\theta'$.

This plane wave, which is obliquely incident on the configuration of Figure 1, is the primary excitation of the structure. The arbitrarily polarized field $[\bar{E}^{0,inc}(\bar{\rho}),\bar{H}^{0,inc}(\bar{\rho})]e^{-j\beta z}$, excited at $\bar{\rho}\in(0)$ and given by Eq. [2], is the incident field.

$$\begin{bmatrix}\bar{E}^{0,inc}(\bar{\rho})\\ \bar{H}^{0,inc}(\bar{\rho})\end{bmatrix}e^{-j\beta z} = \begin{bmatrix}\hat{z}E_z^{0,inc}(\bar{\rho})+\bar{E}_t^{0,inc}(\bar{\rho})\\ \hat{z}H_z^{0,inc}(\bar{\rho})+\bar{H}_t^{0,inc}(\bar{\rho})\end{bmatrix}e^{-j\beta z} \qquad [2a]$$

$$\begin{bmatrix} E_z^{0,inc}(\bar{\rho}) \\ H_z^{0,inc}(\bar{\rho}) \end{bmatrix} = \begin{bmatrix} E_0 \\ H_0 \end{bmatrix} \exp(-j\,\bar{k}_\rho^{inc} \cdot \bar{\rho}) = \begin{bmatrix} E_0 \\ H_0 \end{bmatrix} \sum_{n=-\infty}^{\infty} J_n(k_{c0}\rho_1)\, j^n\, e^{jn(\varphi_1-\varphi')} \qquad [2b]$$

$$\begin{bmatrix} E_\varphi^{0,inc}(\bar{\rho}) \\ H_\varphi^{0,inc}(\bar{\rho}) \end{bmatrix} = \begin{bmatrix} E_0 \\ H_0 \end{bmatrix} \sum_{n=-\infty}^{\infty} \begin{bmatrix} \frac{\beta n}{k_{c0}^2\rho_1} J_n(k_{c0}\rho_1) & \frac{j\omega\mu_0}{k_{c0}} J_n'(k_{c0}\rho_1) \\ -\frac{j\omega\varepsilon_0+\sigma_0}{k_{c0}} J_n'(k_{c0}\rho_1) & \frac{\beta n}{k_{c0}^2\rho_1} J_n(k_{c0}\rho_1) \end{bmatrix} j^n\, e^{jn(\varphi_1-\varphi')} \qquad [2c]$$

where (E_0, H_0) are the magnitudes of the incident electric and magnetic fields, (ρ_1, φ_1) are the polar coordinates of $\bar{\rho}$ in (O_1), $k_{c0} = \sqrt{k_0^2 - \beta^2}$, $k_0 = \omega\sqrt{\varepsilon_0\mu_0}$, $\beta = k_0 \cos\theta'$ is the propagation constant, $J_n(.)$ stands for the Bessel function of order n, and $J_n'(.)$ is the derivative of the Bessel function of order n with respect to its argument. The φ-components of the incident field are expressed in terms of E_z^{inc} and H_z^{inc} by Eq. [2c]. The $\exp[j(\omega t - \beta z)]$ time- and *z*- dependence is suppressed throughout the analysis.

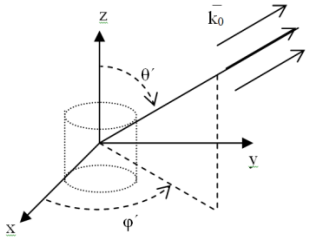

Figure 2. The obliquely incident (upon the cylindrical structure) plane wave.

The field $[\bar{E}^{i,sc}(\bar{\rho}), \bar{H}^{i,sc}(\bar{\rho})]e^{-j\beta z}$, excited at $\bar{\rho} \in (i)$; $i = 0,1,2$, because of the presence of the cylindrical structure of Figure 1, is the scattered field. In the cylindrical coordinate system (O_i), the z- and φ- components of the scattered field are given by Eq. (3):

$$\begin{bmatrix} E_z^{0,sc}(\bar{\rho}) \\ H_z^{0,sc}(\bar{\rho}) \end{bmatrix} = \sum_{n=-\infty}^{\infty} H_n(k_{c0}\rho_1) e^{jn\varphi_1} \begin{bmatrix} c_n^1 \\ d_n^1 \end{bmatrix} \qquad [3a]$$

$$\begin{bmatrix} E_\varphi^{0,sc}(\bar{\rho}) \\ H_\varphi^{0,sc}(\bar{\rho}) \end{bmatrix} = \sum_{n=-\infty}^{\infty} \begin{bmatrix} \frac{\beta n}{k_{c0}^2\rho_1} H_n(k_{c0}\rho_1) & \frac{j\omega\mu_0}{k_{c0}} H_n'(k_{c0}\rho_1) \\ -\frac{j\omega\varepsilon_0+\sigma_0}{k_{c0}} H_n'(k_{c0}\rho_1) & \frac{\beta n}{k_{c0}^2\rho_1} H_n(k_{c0}\rho_1) \end{bmatrix} e^{jn\varphi_1} \begin{bmatrix} c_n^1 \\ d_n^1 \end{bmatrix} \qquad [3b]$$

$$\begin{bmatrix} E_z^{1,sc}(\bar{\rho}) \\ H_z^{1,sc}(\bar{\rho}) \end{bmatrix} = \sum_{n=-\infty}^{\infty} \left\{ J_n(k_{c1}\rho_1) e^{jn\varphi_1} \begin{bmatrix} a_n^1 \\ b_n^1 \end{bmatrix} + H_n(k_{c1}\rho_2) e^{jn\varphi_2} \begin{bmatrix} c_n^2 \\ d_n^2 \end{bmatrix} \right\} \qquad [3c]$$

$$\begin{bmatrix} E_\varphi^{1,sc}(\bar{\rho}) \\ H_\varphi^{1,sc}(\bar{\rho}) \end{bmatrix} = \sum_{n=-\infty}^{\infty} \left\{ \begin{bmatrix} \frac{\beta n}{k_{c1}^2\rho_1} J_n(k_{c1}\rho_1) & \frac{j\omega\mu_1}{k_{c1}} J_n'(k_{c1}\rho_1) \\ -\frac{j\omega\varepsilon_1+\sigma_1}{k_{c1}} J_n'(k_{c1}\rho_1) & \frac{\beta n}{k_{c1}^2\rho_1} J_n(k_{c1}\rho_1) \end{bmatrix} e^{jn\varphi_1} \begin{bmatrix} a_n^1 \\ b_n^1 \end{bmatrix} + \right.$$
$$\left. + \begin{bmatrix} \frac{\beta n}{k_{c1}^2\rho_2} H_n(k_{c1}\rho_2) & \frac{j\omega\mu_1}{k_{c1}} H_n'(k_{c1}\rho_2) \\ -\frac{j\omega\varepsilon_1+\sigma_1}{k_{c1}} H_n'(k_{c1}\rho_2) & \frac{\beta n}{k_{c1}^2\rho_2} H_n(k_{c1}\rho_2) \end{bmatrix} e^{jn\varphi_2} \begin{bmatrix} c_n^2 \\ d_n^2 \end{bmatrix} \right\} \qquad [3d]$$

$$\begin{bmatrix} E_z^{2,sc}(\bar{\rho}) \\ H_z^{2,sc}(\bar{\rho}) \end{bmatrix} = \sum_{n=-\infty}^{\infty} J_n(k_{c2}\rho_2) e^{jn\varphi_2} \begin{bmatrix} a_n^2 \\ b_n^2 \end{bmatrix} \quad [3e]$$

$$\begin{bmatrix} E_\varphi^{2,sc}(\bar{\rho}) \\ H_\varphi^{2,sc}(\bar{\rho}) \end{bmatrix} = \sum_{n=-\infty}^{\infty} \begin{bmatrix} \frac{\beta n}{k_{c2}^2\rho_2} J_n(k_{c2}\rho_2) & \frac{j\omega\mu_2}{k_{c2}} J_n'(k_{c2}\rho_2) \\ -\frac{j\omega\varepsilon_2+\sigma_2}{k_{c2}} J_n'(k_{c2}\rho_2) & \frac{\beta n}{k_{c2}^2\rho_2} J_n(k_{c2}\rho_2) \end{bmatrix} e^{jn\varphi_2} \begin{bmatrix} a_n^2 \\ b_n^2 \end{bmatrix} \quad [3f]$$

where i designates the cylindrical region, (ρ_i, φ_i) denote the polar coordinates of $\bar{\rho}$ in the corresponding coordinate system (O_i), a_n^i, c_n^i are the electric field expansion coefficients, b_n^i, d_n^i are the magnetic field expansion coefficients, $k_{ci} = \sqrt{k_i^2 - \beta^2}$, $k_i = \sqrt{\varepsilon_i \mu_i \omega^2 - j\omega\mu_i\sigma_i}$, and $H_n(.)$ denotes the Hankel function of the second kind and of order n.

Using the translational addition theorem, Abramowitz and Stegun (1972), Konistis and Tsalamengas (1997), Vardiambasis et al. (2004):

$$J_n(k_{c1}\rho_1)e^{jn\varphi_1} = \sum_{m=-\infty}^{\infty} J_{n-m}\left(k_{c1}D_{1q}\right)e^{j(n-m)\varphi_{1q}} J_m\left(k_{c1}\rho_q\right)e^{jm\varphi_q} \quad [4a]$$

$$H_n(k_{c1}\rho_s)e^{jn\varphi_s} = \sum_{m=-\infty}^{\infty} H_{n-m}\left(k_{c1}\rho_{q,s}^{>}\right)e^{j(n-m)\varphi_{q,s}^{>}} J_m\left(k_{c1}\rho_{q,s}^{<}\right)e^{jm\varphi_{q,s}^{<}} \quad [4b]$$

$$\rho_{q,s}^{>} = \max\{\rho_q, D_{sq}\}, \quad \rho_{q,s}^{<} = \min\{\rho_q, D_{sq}\} \quad [4c]$$

$$\varphi_{q,s}^{<} = \begin{cases} \varphi_q, \, if \; \rho_{q,s}^{<} = \rho_q \\ \varphi_{sq}, \, if \; \rho_{q,s}^{<} = D_{sq} \end{cases}, \quad \varphi_{q,s}^{>} = \begin{cases} \varphi_q, \, if \; \rho_{q,s}^{>} = \rho_q \\ \varphi_{sq}, \, if \; \rho_{q,s}^{>} = D_{sq} \end{cases} \quad [4d]$$

where (O_s) and (O_q) are the coordinate systems corresponding to s- and q- cylinder, respectively.

Substituting (4) in (3), we get the excitation field in any region (i). The total field $[\bar{E}^{i,tot}(\bar{\rho}), \bar{H}^{i,tot}(\bar{\rho})]e^{-j\beta z}$ at $\bar{\rho} \in (i)$ can be expressed, with the help of (2)-(4), as:

$$\begin{bmatrix} E_z^{0,tot}(\bar{\rho}) \\ H_z^{0,tot}(\bar{\rho}) \end{bmatrix} = \begin{bmatrix} E_z^{0,sc}(\bar{\rho}) \\ H_z^{0,sc}(\bar{\rho}) \end{bmatrix} + \begin{bmatrix} E_z^{0,inc}(\bar{\rho}) \\ H_z^{0,inc}(\bar{\rho}) \end{bmatrix} = \\ = \sum_{n=-\infty}^{\infty} \left\{ H_n(k_{c0}\rho_1)e^{jn\varphi_1} \begin{bmatrix} c_n^1 \\ d_n^1 \end{bmatrix} + J_n(k_{c0}\rho_1)\, j^n\, e^{jn(\varphi_1-\varphi')} \begin{bmatrix} E_0 \\ H_0 \end{bmatrix} \right\} \quad [5a]$$

$$\begin{bmatrix} E_\varphi^{0,tot}(\bar{\rho}) \\ H_\varphi^{0,tot}(\bar{\rho}) \end{bmatrix} = \begin{bmatrix} E_\varphi^{0,sc}(\bar{\rho}) \\ H_\varphi^{0,sc}(\bar{\rho}) \end{bmatrix} + \begin{bmatrix} E_\varphi^{0,inc}(\bar{\rho}) \\ H_\varphi^{0,inc}(\bar{\rho}) \end{bmatrix} = \\ = \sum_{n=-\infty}^{\infty} \left\{ \begin{bmatrix} \frac{\beta n}{k_{c0}^2\rho_1} H_n(k_{c0}\rho_1) & \frac{j\omega\mu_0}{k_{c0}} H_n'(k_{c0}\rho_1) \\ -\frac{j\omega\varepsilon_0+\sigma_0}{k_{c0}} H_n'(k_{c0}\rho_1) & \frac{\beta n}{k_{c0}^2\rho_1} H_n(k_{c0}\rho_1) \end{bmatrix} e^{jn\varphi_1} \begin{bmatrix} c_n^1 \\ d_n^1 \end{bmatrix} + \right. \quad [5b]$$

$$\left. + \begin{bmatrix} \frac{\beta n}{k_{c0}^2\rho_1} J_n(k_{c0}\rho_1) & \frac{j\omega\mu_0}{k_{c0}} J_n'(k_{c0}\rho_1) \\ -\frac{j\omega\varepsilon_0+\sigma_0}{k_{c0}} J_n'(k_{c0}\rho_1) & \frac{\beta n}{k_{c0}^2\rho_1} J_n(k_{c0}\rho_1) \end{bmatrix} j^n\, e^{jn(\varphi_1-\varphi')} \begin{bmatrix} E_0 \\ H_0 \end{bmatrix} \right\}$$

$$\begin{bmatrix} E_z^{1,tot}(\bar{\rho}) \\ H_z^{1,tot}(\bar{\rho}) \end{bmatrix} = \begin{bmatrix} E_z^{1,sc}(\bar{\rho}) \\ H_z^{1,sc}(\bar{\rho}) \end{bmatrix} = \\ = \sum_{n=-\infty}^{\infty} \left\{ J_n(k_{c1}\rho_1) e^{jn\varphi_1} \begin{bmatrix} a_n^1 \\ b_n^1 \end{bmatrix} + H_n(k_{c1}\rho_2) e^{jn\varphi_2} \begin{bmatrix} c_n^2 \\ d_n^2 \end{bmatrix} \right\} \quad [5c]$$

$$\begin{bmatrix} E_\varphi^{1,tot}(\bar{\rho}) \\ H_\varphi^{1,tot}(\bar{\rho}) \end{bmatrix} = \begin{bmatrix} E_\varphi^{1,sc}(\bar{\rho}) \\ H_\varphi^{1,sc}(\bar{\rho}) \end{bmatrix} = \\ = \sum_{n=-\infty}^{\infty} \left\{ \begin{bmatrix} \frac{\beta n}{k_{c1}^2 \rho_1} J_n(k_{c1}\rho_1) & \frac{j\omega\mu_1}{k_{c1}} J_n'(k_{c1}\rho_1) \\ -\frac{j\omega\varepsilon_1 + \sigma_1}{k_{c1}} J_n'(k_{c1}\rho_1) & \frac{\beta n}{k_{c1}^2 \rho_1} J_n(k_{c1}\rho_1) \end{bmatrix} e^{jn\varphi_1} \begin{bmatrix} a_n^1 \\ b_n^1 \end{bmatrix} + \right. \quad [5d]$$
$$\left. + \begin{bmatrix} \frac{\beta n}{k_{c1}^2 \rho_2} H_n(k_{c1}\rho_2) & \frac{j\omega\mu_1}{k_{c1}} H_n'(k_{c1}\rho_2) \\ -\frac{j\omega\varepsilon_1 + \sigma_1}{k_{c1}} H_n'(k_{c1}\rho_2) & \frac{\beta n}{k_{c1}^2 \rho_2} H_n(k_{c1}\rho_2) \end{bmatrix} e^{jn\varphi_2} \begin{bmatrix} c_n^2 \\ d_n^2 \end{bmatrix} \right\}$$

$$\begin{bmatrix} E_z^{2,tot}(\bar{\rho}) \\ H_z^{2,tot}(\bar{\rho}) \end{bmatrix} = \begin{bmatrix} E_z^{2,sc}(\bar{\rho}) \\ H_z^{2,sc}(\bar{\rho}) \end{bmatrix} = \sum_{n=-\infty}^{\infty} J_n(k_{c2}\rho_2) e^{jn\varphi_2} \begin{bmatrix} a_n^2 \\ b_n^2 \end{bmatrix} \quad [5e]$$

$$\begin{bmatrix} E_\varphi^{2,tot}(\bar{\rho}) \\ H_\varphi^{2,tot}(\bar{\rho}) \end{bmatrix} = \begin{bmatrix} E_\varphi^{2,sc}(\bar{\rho}) \\ H_\varphi^{2,sc}(\bar{\rho}) \end{bmatrix} = \\ = \sum_{n=-\infty}^{\infty} \begin{bmatrix} \frac{\beta n}{k_{c2}^2 \rho_2} J_n(k_{c2}\rho_2) & \frac{j\omega\mu_2}{k_{c2}} J_n'(k_{c2}\rho_2) \\ -\frac{j\omega\varepsilon_2 + \sigma_2}{k_{c2}} J_n'(k_{c2}\rho_2) & \frac{\beta n}{k_{c2}^2 \rho_2} J_n(k_{c2}\rho_2) \end{bmatrix} e^{jn\varphi_2} \begin{bmatrix} a_n^2 \\ b_n^2 \end{bmatrix} \quad [5f]$$

Finally, we apply the continuity conditions for the E_z, H_z, E_φ and H_φ components of the total field of Eq. [5] over both cylindrical boundaries of the structure $\rho_1 = \alpha_1$ and $\rho_2 = \alpha_2$:

$$\begin{bmatrix} E_z^{0,tot} \\ H_z^{0,tot} \end{bmatrix}_{\rho_1=\alpha_1} = \begin{bmatrix} E_z^{1,tot} \\ H_z^{1,tot} \end{bmatrix}_{\rho_1=\alpha_1} \Rightarrow \sum_{n=-\infty}^{\infty} \left\{ H_n(k_{c0}\alpha_1)\, e^{jn\varphi_1} \begin{bmatrix} c_n^1 \\ d_n^1 \end{bmatrix} + J_n(k_{c0}\alpha_1)\, j^n\, e^{jn(\varphi_1-\varphi')} \begin{bmatrix} E_0 \\ H_0 \end{bmatrix} \right\} = \\ = \sum_{n=-\infty}^{\infty} \left\{ J_n(k_{c1}\alpha_1)\, e^{jn\varphi_1} \begin{bmatrix} a_n^1 \\ b_n^1 \end{bmatrix} + H_n(k_{c1}\rho_2)\, e^{jn\varphi_2} \begin{bmatrix} c_n^2 \\ d_n^2 \end{bmatrix} \right\} \Rightarrow \quad [6a]$$
$$\Rightarrow \sum_{n=-\infty}^{\infty} \left\{ J_n(k_{c1}\alpha_1)\, e^{jn\varphi_1} \begin{bmatrix} a_n^1 \\ b_n^1 \end{bmatrix} - H_n(k_{c0}\alpha_1) e^{jn\varphi_1} \begin{bmatrix} c_n^1 \\ d_n^1 \end{bmatrix} + \right.$$
$$\left. + \sum_{m=-\infty}^{\infty} \mathrm{H}_{n-m}(k_{c1}D_{21})\, e^{j(n-m)\varphi_{21}} J_m(k_{c1}\alpha_1)\, e^{jm\varphi_1} \begin{bmatrix} c_n^2 \\ d_n^2 \end{bmatrix} \right\} = \sum_{n=-\infty}^{\infty} J_n(k_{c0}\alpha_1)\, j^n\, e^{jn(\varphi_1-\varphi')} \begin{bmatrix} E_0 \\ H_0 \end{bmatrix}$$

$$\begin{bmatrix} E_\varphi^{0,tot} \\ H_\varphi^{0,tot} \end{bmatrix}_{\rho_1=\alpha_1} = \begin{bmatrix} E_\varphi^{1,tot} \\ H_\varphi^{1,tot} \end{bmatrix}_{\rho_1=\alpha_1} \Rightarrow \sum_{n=-\infty}^{\infty} \left\{ \begin{bmatrix} \frac{\beta n}{k_{c0}^2 \alpha_1} H_n(k_{c0}\alpha_1) & \frac{j\omega\mu_0}{k_{c0}} H_n'(k_{c0}\alpha_1) \\ -\frac{j\omega\varepsilon_0+\sigma_0}{k_{c0}} H_n'(k_{c0}\alpha_1) & \frac{\beta n}{k_{c0}^2 \alpha_1} H_n(k_{c0}\alpha_1) \end{bmatrix} e^{jn\varphi_1} \begin{bmatrix} c_n^1 \\ d_n^1 \end{bmatrix} + \right.$$

$$\left. + \begin{bmatrix} \frac{\beta n}{k_{c0}^2 \alpha_1} J_n(k_{c0}\alpha_1) & \frac{j\omega\mu_0}{k_{c0}} J_n'(k_{c0}\alpha_1) \\ -\frac{j\omega\varepsilon_0+\sigma_0}{k_{c0}} J_n'(k_{c0}\alpha_1) & \frac{\beta n}{k_{c0}^2 \alpha_1} J_n(k_{c0}\alpha_1) \end{bmatrix} j^n e^{jn(\varphi_1-\varphi')} \begin{bmatrix} E_0 \\ H_0 \end{bmatrix} \right\} =$$

$$= \sum_{n=-\infty}^{\infty} \left\{ \begin{bmatrix} \frac{\beta n}{k_{c1}^2 \alpha_1} J_n(k_{c1}\alpha_1) & \frac{j\omega\mu_1}{k_{c1}} J_n'(k_{c1}\alpha_1) \\ -\frac{j\omega\varepsilon_1+\sigma_1}{k_{c1}} J_n'(k_{c1}\alpha_1) & \frac{\beta n}{k_{c1}^2 \alpha_1} J_n(k_{c1}\alpha_1) \end{bmatrix} e^{jn\varphi_1} \begin{bmatrix} a_n^1 \\ b_n^1 \end{bmatrix} + \right.$$

$$\left. + \begin{bmatrix} \frac{\beta n}{k_{c1}^2 \rho_2} H_n(k_{c1}\rho_2) & \frac{j\omega\mu_1}{k_{c1}} H_n'(k_{c1}\rho_2) \\ -\frac{j\omega\varepsilon_1+\sigma_1}{k_{c1}} H_n'(k_{c1}\rho_2) & \frac{\beta n}{k_{c1}^2 \rho_2} H_n(k_{c1}\rho_2) \end{bmatrix} e^{jn\varphi_2} \begin{bmatrix} c_n^2 \\ d_n^2 \end{bmatrix} \right\} \Rightarrow$$

$$\Rightarrow \sum_{n=-\infty}^{\infty} \left\{ \begin{bmatrix} \frac{\beta n}{k_{c1}^2 \alpha_1} J_n(k_{c1}\alpha_1) & \frac{j\omega\mu_1}{k_{c1}} J_n'(k_{c1}\alpha_1) \\ -\frac{j\omega\varepsilon_1+\sigma_1}{k_{c1}} J_n'(k_{c1}\alpha_1) & \frac{\beta n}{k_{c1}^2 \alpha_1} J_n(k_{c1}\alpha_1) \end{bmatrix} e^{jn\varphi_1} \begin{bmatrix} a_n^1 \\ b_n^1 \end{bmatrix} - \right.$$

$$- \begin{bmatrix} \frac{\beta n}{k_{c0}^2 \alpha_1} H_n(k_{c0}\alpha_1) & \frac{j\omega\mu_0}{k_{c0}} H_n'(k_{c0}\alpha_1) \\ -\frac{j\omega\varepsilon_0+\sigma_0}{k_{c0}} H_n'(k_{c0}\alpha_1) & \frac{\beta n}{k_{c0}^2 \alpha_1} H_n(k_{c0}\alpha_1) \end{bmatrix} e^{jn\varphi_1} \begin{bmatrix} c_n^1 \\ d_n^1 \end{bmatrix} +$$

$$\left. + \sum_{m=-\infty}^{\infty} \mathrm{H}_{n-m}(k_{c1} D_{21})\, e^{j(n-m)\varphi_{21}} \begin{bmatrix} \frac{\beta m}{k_{c1}^2 \alpha_1} J_m(k_{c1}\alpha_1) & \frac{j\omega\mu_1}{k_{c1}} J_m'(k_{c1}\alpha_1) \\ \frac{-j\omega\varepsilon_1+\sigma_1}{k_{c1}} J_m'(k_{c1}\alpha_1) & \frac{\beta m}{k_{c1}^2 \alpha_1} J_m(k_{c1}\alpha_1) \end{bmatrix} e^{jm\varphi_1} \begin{bmatrix} c_n^2 \\ d_n^2 \end{bmatrix} \right\} =$$

$$= \sum_{n=-\infty}^{\infty} \begin{bmatrix} \frac{\beta n}{k_{c0}^2 \alpha_1} J_n(k_{c0}\alpha_1) & \frac{j\omega\mu_0}{k_{c0}} J_n'(k_{c0}\alpha_1) \\ -\frac{j\omega\varepsilon_0+\sigma_0}{k_{c0}} J_n'(k_{c0}\alpha_1) & \frac{\beta n}{k_{c0}^2 \alpha_1} J_n(k_{c0}\alpha_1) \end{bmatrix} j^n e^{jn(\varphi_1-\varphi')} \begin{bmatrix} E_0 \\ H_0 \end{bmatrix} \qquad [6b]$$

$$\begin{bmatrix} E_z^{1,tot} \\ H_z^{1,tot} \end{bmatrix}_{\rho_2=\alpha_2} = \begin{bmatrix} E_z^{2,tot} \\ H_z^{2,tot} \end{bmatrix}_{\rho_2=\alpha_2} \Rightarrow \sum_{n=-\infty}^{\infty} \left\{ J_n(k_{c1}\rho_1)\, e^{jn\varphi_1} \begin{bmatrix} a_n^1 \\ b_n^1 \end{bmatrix} + H_n(k_{c1}\alpha_2) e^{jn\varphi_2} \begin{bmatrix} c_n^2 \\ d_n^2 \end{bmatrix} \right\} =$$

$$= \sum_{n=-\infty}^{\infty} J_n(k_{c2}\alpha_2)\, e^{jn\varphi_2} \begin{bmatrix} a_n^2 \\ b_n^2 \end{bmatrix} \Rightarrow \sum_{n=-\infty}^{\infty} \left\{ \sum_{m=-\infty}^{\infty} J_{n-m}(k_{c1} D_{12})\, e^{j(n-m)\varphi_{12}} J_m(k_{c1}\alpha_2)\, e^{jm\varphi_2} \begin{bmatrix} a_n^1 \\ b_n^1 \end{bmatrix} - \right. \qquad [6c]$$

$$\left. - J_n(k_{c2}\alpha_2)\, e^{jn\varphi_2} \begin{bmatrix} a_n^2 \\ b_n^2 \end{bmatrix} + \sum_{n=-\infty}^{\infty} H_n(k_{c1}\alpha_2)\, e^{jn\varphi_2} \begin{bmatrix} c_n^2 \\ d_n^2 \end{bmatrix} \right\} = \begin{bmatrix} 0 \\ 0 \end{bmatrix}$$

$$\begin{bmatrix} E_{\varphi}^{1,tot} \\ H_{\varphi}^{1,tot} \end{bmatrix}_{\rho_2=\alpha_2} = \begin{bmatrix} E_{\varphi}^{2,tot} \\ H_{\varphi}^{2,tot} \end{bmatrix}_{\rho_2=\alpha_2} \Rightarrow \sum_{n=-\infty}^{\infty} \left\{ \begin{bmatrix} \frac{\beta n}{k_{c1}^2 \rho_1} J_n(k_{c1}\rho_1) & \frac{j\omega\mu_1}{k_{c1}} J_n'(k_{c1}\rho_1) \\ -\frac{j\omega\varepsilon_1+\sigma_1}{k_{c1}} J_n'(k_{c1}\rho_1) & \frac{\beta n}{k_{c1}^2 \rho_1} J_n(k_{c1}\rho_1) \end{bmatrix} e^{jn\varphi_1} \begin{bmatrix} a_n^1 \\ b_n^1 \end{bmatrix} + \right.$$

$$\left. + \begin{bmatrix} \frac{\beta n}{k_{c1}^2 \alpha_2} H_n(k_{c1}\alpha_2) & \frac{j\omega\mu_1}{k_{c1}} H_n'(k_{c1}\alpha_2) \\ -\frac{j\omega\varepsilon_1+\sigma_1}{k_{c1}} H_n'(k_{c1}\alpha_2) & \frac{\beta n}{k_{c1}^2 \alpha_2} H_n(k_{c1}\alpha_2) \end{bmatrix} e^{jn\varphi_2} \begin{bmatrix} c_n^2 \\ d_n^2 \end{bmatrix} \right\} =$$

$$= \sum_{n=-\infty}^{\infty} \begin{bmatrix} \frac{\beta n}{k_{c2}^2 \alpha_2} J_n(k_{c2}\alpha_2) & \frac{j\omega\mu_2}{k_{c2}} J_n'(k_{c2}\alpha_2) \\ -\frac{j\omega\varepsilon_2+\sigma_2}{k_{c2}} J_n'(k_{c2}\alpha_2) & \frac{\beta n}{k_{c2}^2 \alpha_2} J_n(k_{c2}\alpha_2) \end{bmatrix} e^{jn\varphi_2} \begin{bmatrix} a_n^2 \\ b_n^2 \end{bmatrix} \Rightarrow$$

$$\Rightarrow \sum_{n=-\infty}^{\infty} \left\{ \sum_{m=-\infty}^{\infty} J_{n-m}(k_{c1}D_{12})\, e^{j(n-m)\varphi_{12}} \begin{bmatrix} \frac{\beta m}{k_{c1}^2 \alpha_2} J_m(k_{c1}\alpha_2) & \frac{j\omega\mu_1}{k_{c1}} J_m'(k_{c1}\alpha_2) \\ -\frac{j\omega\varepsilon_1+\sigma_1}{k_{c1}} J_m'(k_{c1}\alpha_2) & \frac{\beta m}{k_{c1}^2 \alpha_2} J_m(k_{c1}\alpha_2) \end{bmatrix} e^{jm\varphi_2} \begin{bmatrix} a_n^1 \\ b_n^1 \end{bmatrix} - \right.$$

$$- \begin{bmatrix} \frac{\beta n}{k_{c2}^2 \alpha_2} J_n(k_{c2}\alpha_2) & \frac{j\omega\mu_2}{k_{c2}} J_n'(k_{c2}\alpha_2) \\ -\frac{j\omega\varepsilon_2+\sigma_2}{k_{c2}} J_n'(k_{c2}\alpha_2) & \frac{\beta n}{k_{c2}^2 \alpha_2} J_n(k_{c2}\alpha_2) \end{bmatrix} e^{jn\varphi_2} \begin{bmatrix} a_n^2 \\ b_n^2 \end{bmatrix} +$$

$$\left. + \begin{bmatrix} \frac{\beta n}{k_{c1}^2 \alpha_2} H_n(k_{c1}\alpha_2) & \frac{j\omega\mu_1}{k_{c1}} H_n'(k_{c1}\alpha_2) \\ -\frac{j\omega\varepsilon_1+\sigma_1}{k_{c1}} H_n'(k_{c1}\alpha_2) & \frac{\beta n}{k_{c1}^2 \alpha_2} H_n(k_{c1}\alpha_2) \end{bmatrix} e^{jn\varphi_2} \begin{bmatrix} c_n^2 \\ d_n^2 \end{bmatrix} = \begin{bmatrix} 0 \\ 0 \end{bmatrix} \right. \quad [6d]$$

Then we multiply both sides of Eq. [6a] and Eq. [6b] by $\exp(-jM\varphi_1)$ and integrate them from $\varphi_1 = 0$ to $\varphi_1 = 2\pi$, while we multiply both sides of Eq. [6c] and [6d] by $\exp(-jM\varphi_2)$ and integrate them from $\varphi_2 = 0$ to $\varphi_2 = 2\pi$.

We thus obtain an infinite, linear, algebraic system for the unknown expansion constants, whose matrix elements and constant terms are given in closed form by simple analytical expressions (mostly single-term Bessel or Hankel functions). Solving this system leads to an extremely accurate, very fast and efficient (requiring small truncation sizes N_r) evaluation of the field expansion coefficients $a_M^1, b_M^1, c_M^1, d_M^1, a_M^2, b_M^2, c_M^2, d_M^2$. Then, we can use Eq. [5] to compute to total (incident and scattered) electromagnetic field at any point of the cylindrical structure of Figure 1.

Overview of the corresponding linear algebraic system reveals that the physical, geometrical, and electrical parameters affecting the scattered and total electromagnetic field, and consequently the active radar scattering cross section $k_0\sigma_t$, are: the direction of the incident plane wave (θ', φ'), the wavelength λ_0, as well as the radii a_i, the dielectric permittivities ε_i, the dielectric losses σ_i, and the relative positions (expressed by the distance D_{12}, in case of Figure 1) of the circular cylinders.

As described thoroughly in Section 2, the mathematical procedure needed for the calculation of the scattered electromagnetic field components, even though analytical, it is rather complex and time demanding. An alternative way, based on a neural network model, is proposed herein. Neural

networks are deployed to investigate the aforementioned relations and determine the near field values. For this purpose, in the following Section we develop an artificial neural network aiming to predict the value of E_z^{tot} at any point of the cross section of the structure of Figure 1, when the radius α_2 and the dielectric permittivity ε_2 of the cylindrical dielectric rod, along with the observer's (x, y) position, are given input factors.

3. NEURAL NETWORK MODELING

Figure 3 displays a typical architecture of a four-layer MLP ANN. By M_n, where $n = 1,2,\text{K},N$ is denoted the number of neurons in each layer. The n index indicates the ANN's layers of which $n=1$ refers to the input (left-most) layer, and $n=N$ refers to the output (last) layer. The input to ANN's first layer is denoted by vector $\mathbf{x} = \left\{x_1, x_2, \text{K}, x_{M_0}\right\}$, where M_0 corresponds to the inputs' number. The n-th layer output is denoted by vector $\mathbf{y}^n = \left\{y_1^n, y_2^n, \text{K}, y_{M_i}^n\right\}$. The MLP ANN shown in Figure 3 is of sequential architecture meaning that the output of any n-th layer is propagated as input to the immediate successive (n+1)-th layer. Each neuron's output for either layer emerges from $\mathbf{y}^n = \Psi^n\left(\mathbf{y}^{n-1}\mathbf{w}^n + \mathbf{b}^n\right)$, where Ψ^n is an appropriately selected activation function, $\mathbf{b}^n$ is a vector containing the bias weighing of the n-th layer, and $\mathbf{w}^n$ is a matrix containing the synaptic weights $w_{i,j}^n$ (with $i = 1,2,\text{K},M_{n-1}$, $j = 1,2,\text{K},M_n$), that are readily adjustable pending training by a suitable algorithm.

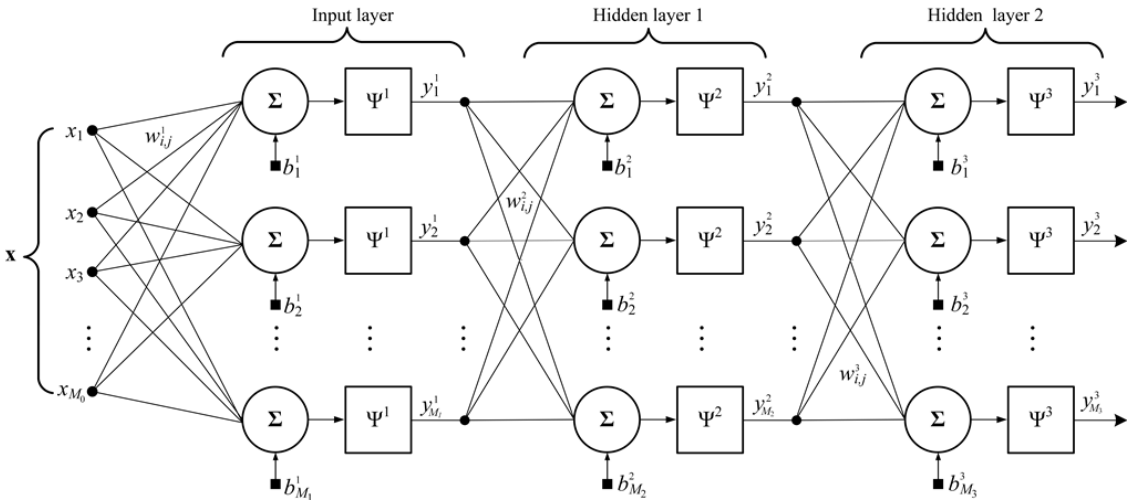

Figure 3. Typical architecture of an one input, two hidden and one output layered feed-forward MLP ANN.

A neural network (NN) model was designed in order to solve the forward problem of the total near field prediction. The NN model, with 1 output and 4 inputs, was trained, validated and tested using 330 full sets of the analytically computed data. NN analysis, modeling and simulations were performed in MATLAB environment, using the deep learning toolbox, MathWorks (2019). The powerful Levenberg-Marquardt (LM) learning algorithm was selected, and the hyperbolic tangent sigmoid activation function was adapted for the hidden layer neurons. The training procedure continued until either the training mean square error was less than the error goal of 10^{-6} (error achievement criterion), or the maximum number of 1000 consecutive times (epochs) was reached (slow convergence criterion), or the validation mean square error was increasing for more than 6 epochs (overfitting avoidance criterion).

The block diagram of the artificial NN model is shown in Figure 4. The dense, sequential, multilayer perceptron (MLP) architecture was selected for the implementation of the NN model, as it is reported to be a well-established universal approximator, Kapetanakis et al. (2018a), Kapetanakis et al. (2018b), and Kapetanakis et al. (2021).

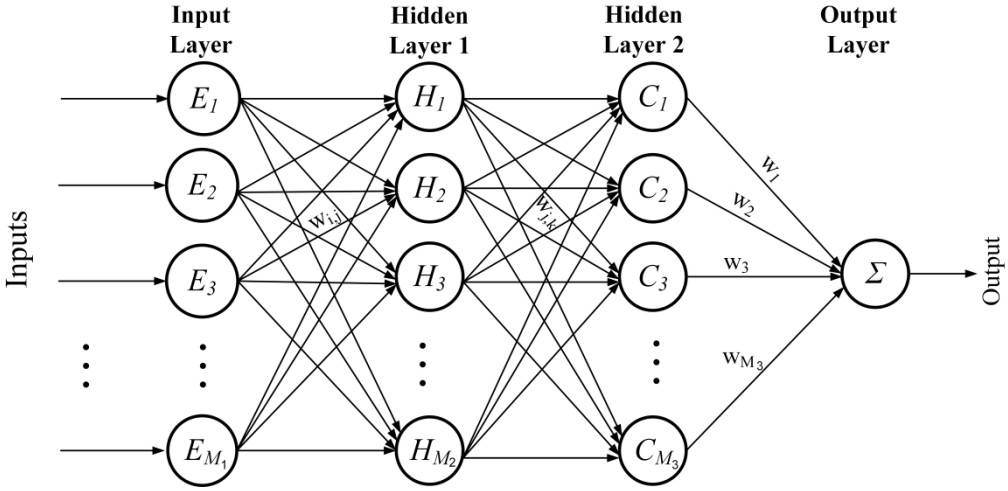

Figure 4. Layout of the neural network models for the near field estimation. M_1, M_2, M_3, and M_4 indicate the numbers of neurons in the input, hidden and output layers. Input parameters appear on the left, the output parameter appears on the right, and the in-box information corresponds to the values of M_1, M_2, M_3, and M_4.

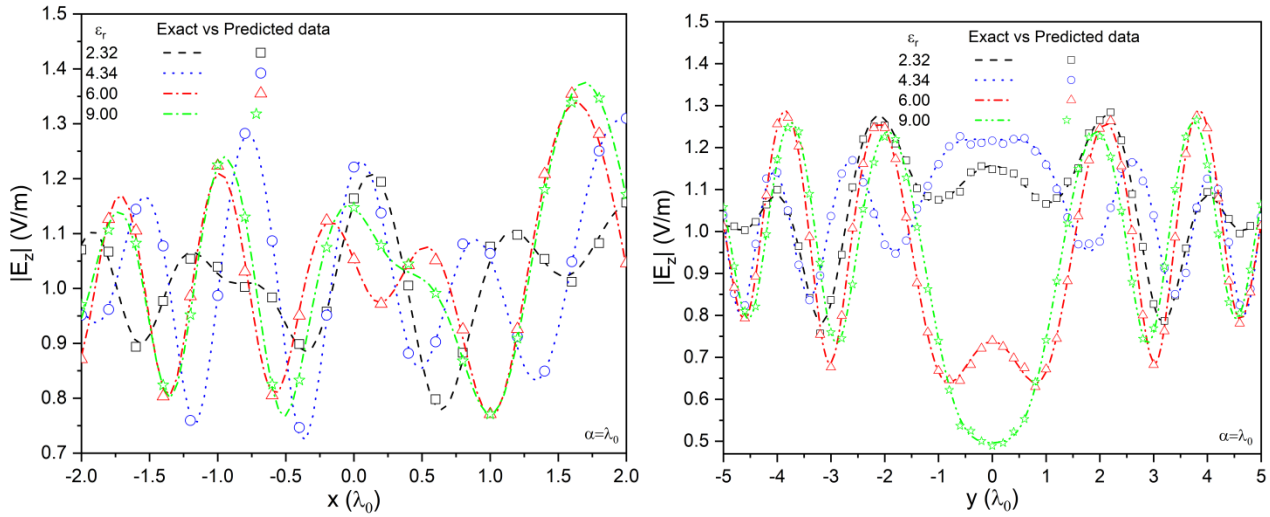

Figure 4. Near field pattern (in Cartesian coordinates) at the cross section of the structure of Figure 1 in case $\varepsilon_1 = \varepsilon_0$, $\varepsilon_2 = \varepsilon_r \varepsilon_0$, $\alpha_2 = \lambda_0$, $D_{12} = 0$, $E_0 = 1$, $H_0 = 0$, $\theta' = 90^o$ (normal incidence). (a) $\left|E_z^{tot}\right|$ vs x (for $-2\lambda_0 \le x \le 2\lambda_0$), (b) $\left|E_z^{tot}\right|$ vs y (for $-5\lambda_0 \le y \le 5\lambda_0$), for several values of ε_r. The exact values (lines) of $\left|E_z^{tot}\right|$ are plotted in comparison to their corresponding predicted from the NN values (symbols). Lines (black dashed, blue dotted, red dash-dotted, green dash-dot-dotted) correspond to the exact values of $\left|E_z^{tot}\right|$, while symbols (black squares, blue circles, red triangles, green stars) represent the predicted values, for $\varepsilon_r = 2.32,\ 4.34,\ 6.0,\ 9.0$, respectively.

Aiming to solve the forward problem of predicting the values of the electromagnetic total near field, the architecture of the NN model displayed in Figure 4 contain a single output and four inputs of the rod characteristic parameters. The architecture for the NN model shown in Figure 4 follows the general block diagram presented in Figure 3. The number of neurons per hidden layer was

selected following multiple experiments targeted at minimizing the Mean Square Error (MSE), defined as shown in Eq. (7):

$$MSE = \frac{1}{K}\sum_{k=1}^{K}(p_k - e_k)^2 \qquad [7]$$

where p_k and e_k stand for the *k*-th predicted by the NN model and the analytically obtained E_z^{tot} values, respectively, while *K* corresponds to the multitude of values used during training. The trial-and-error approach for the NN model that minimizes the MSE in each case concluded with 15x15 neurons in the first and second hidden layers of the NN.

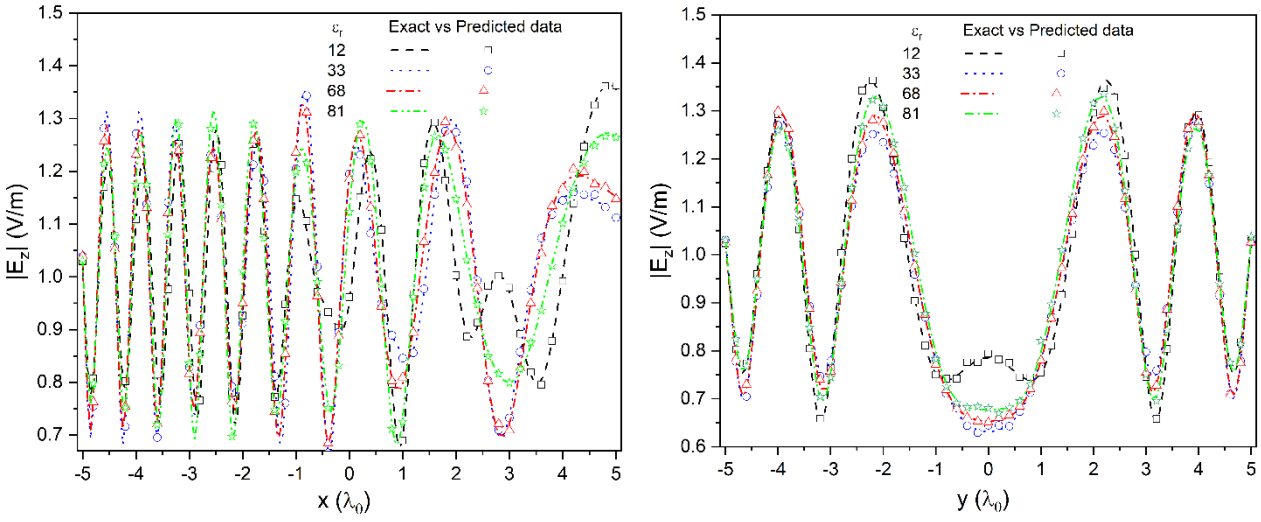

(a) **(b)**

Figure 5. Near field pattern (in Cartesian coordinates) at the cross section of the structure of Figure 1 in case $\varepsilon_1 = \varepsilon_0$, $\varepsilon_2 = \varepsilon_r\varepsilon_0$, $\alpha_2 = \lambda_0$, $D_{12} = 0$, $E_0 = 1$, $H_0 = 0$, $\theta' = 90^o$ (normal incidence). (a) $|E_z^{tot}|$ vs x (for $-5\lambda_0 \le x \le 5\lambda_0$), (b) $|E_z^{tot}|$ vs y (for $-5\lambda_0 \le y \le 5\lambda_0$), for several values of ε_r. The exact values (lines) of $|E_z^{tot}|$ are plotted in comparison to their corresponding predicted from the NN values (symbols). Lines (black dashed, blue dotted, red dash-dotted, green dash-dot-dotted) correspond to the exact values of $|E_z^{tot}|$, while symbols (black squares, blue circles, red triangles, green stars) represent the predicted values, for $\varepsilon_r = 12, 33, 68, 81$, respectively.

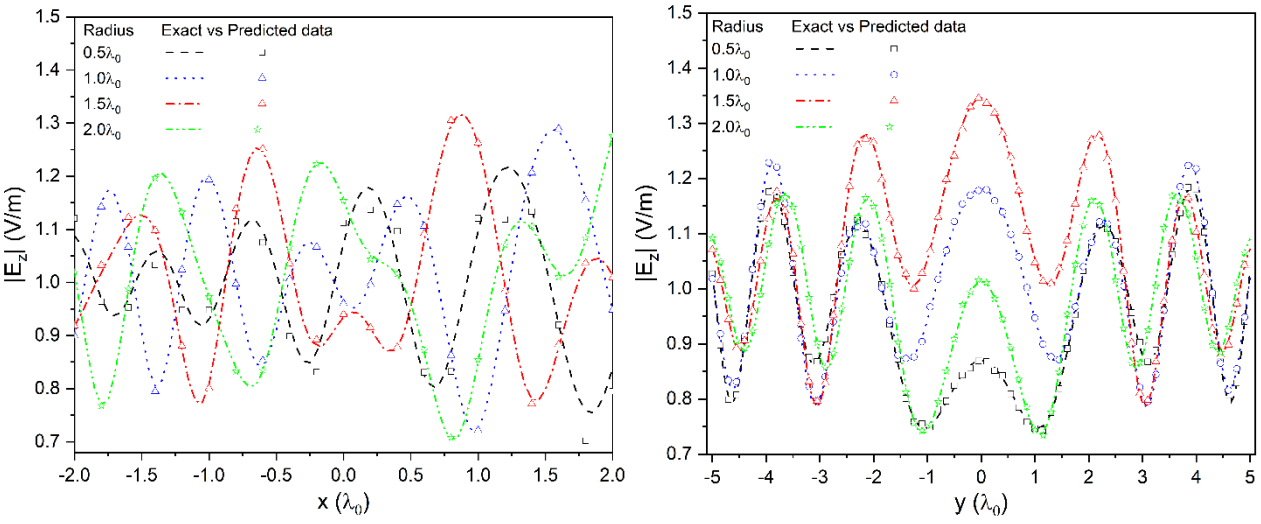

(a) **(b)**

Figure 6. Near field pattern (in Cartesian coordinates) at the cross section of the structure of Figure 1 in case $\varepsilon_1 = \varepsilon_0$, $\varepsilon_2 = 3.5\varepsilon_0$, $D_{12} = 0$, $E_0 = 1$, $H_0 = 0$, $\theta' = 90^o$ (normal incidence). (a) $|E_z^{tot}|$ vs x (for $-2\lambda_0 \le x \le 2\lambda_0$), (b)

$\left|E_z^{tot}\right|$ vs y (for $-5\lambda_0 \le y \le 5\lambda_0$), for several values of α_2. The exact values (lines) of $\left|E_z^{tot}\right|$ are plotted in comparison to their corresponding predicted from the NN values (symbols). Lines (black dashed, blue dotted, red dash-dotted, green dash-dot-dotted) correspond to the exact values of $\left|E_z^{tot}\right|$, while symbols (black squares, blue circles, red triangles, green stars) represent the predicted values, for $\alpha_2 / \lambda_0 = 0.5, 1.0, 1.5, 2.0$, respectively.

3.1. NN model's performance

Following the NN training and validation processes, the implemented model was tested with respect to its performance, using the previously unseen testing datasets consisting of quintets in the form of $\left(\alpha_k^{te}, \varepsilon_{rk}^{te}, x_k^{te}, y_k^{te}; \left|E_z\right|_k^{te}\right)$, where $k = 1,2,\mathrm{K},K$, α_k^{te}, ε_{rk}^{te}, x_k^{te}, and y_k^{te} are the input testing values of the rod radius, the rod dielectric constant, the x and y coordinates of the observing point's position, respectively, and $\left|E_z\right|_k^{te}$ is the output testing value of the $z-$component of the total electric near field at the cross section of the scatterer.

Comparisons of the predicted values of the near field component $\left|E_z\right|$ produced from the NN model, versus their corresponding analytically computed values are given in Figures 4-6. Colored lines (dashed, dotted, dash-dotted, and dash-dot-dotted) correspond to the exact field values, whereas same colored markers (squares, circles, triangles, and stars) indicate the equivalent predicted by the NN electric field values. The results make apparent that the developed NN model is capable to predict the exact near field values. The overall performance of the NN model exhibits excellent accuracy.

4. CONCLUSION

Electromagnetic scattering by a dielectric circular cylindrical rod has been investigated in the case of obliquely incident arbitrarily polarized waves. The solution technique uses the generalized separation variables method and results in a linear algebraic system for the field expansion coefficients, with single-term matrix elements. To validate the developed numerical codes, several comparisons with available results have been carried out. Plotted results for the near field reveal that the geometrical and electrical parameters of the cylindrical structure may control its scattering properties. Moreover a neural network model was proposed to predict the near field on the cross section of the circular dielectric rod. The results predicted from the proposed algorithm were found to perfectly match with the corresponding analytical values. In general, neural networks are effective alternative numerical methods, which can be used to solve the cylindrical structure scattering problem.

5. REFERENCES

Abramowitz, M. and I.A. Stegun. 1972. Handbook of Mathematical Functions, Chapter 9. Dover: New York.

Balanis, C.A. 2012. Advanced Engineering Electromagnetics, 2nd Edition. Wiley.

Chang, S.K. and K.K. Mei. 1976. Application of the unimoment method to electromagnetic scattering of dielectric cylinders. IEEE Transactions on Antennas and Propagation, 24 (1): 35-42.

Choudhury, B., S. Thomas, and R.M. Jha. 2015. Implementation of soft computing optimization techniques in antenna engineering. IEEE Antennas and Propagation Magazine, 57 (6): 122-131.

Christodoulou, C. and M. Georgiopoulos. 2000. Applications of Neural Networks in Electromagnetics. Artech House.

Devabhaktuni, V., M.C.E. Yagoub, Y. Fang, J. Xu, and Q. Zhang. 2001. Neural networks for microwave modeling: model development issues and nonlinear modeling techniques. International Journal of RF and Microwave Computer-Aided Engineering, 11: 4–21.

Elsherbeni, A.Z. and M. Hamid. 1987. Scattering by parallel conducting circular cylinders. IEEE Transactions on Antennas and Propagation, 35 (3): 355-358.

Elsherbeni, A.Z. and A.A. Kishk. 1992. Modeling of cylindrical objects by circular dielectric and conducting cylinders. IEEE Transactions on Antennas and Propagation, 40 (1): 96-99.

Hongo, K. 1978. Multiple scattering by two conducting circular cylinders. IEEE Transactions on Antennas and Propagation, 26 (5): 748-751.

Ishimaru, A. 2017. Electromagnetic Wave Propagation, Radiation, and Scattering: From Fundamentals to Applications, 2nd Edition. Prentice-Hall: New Jersey.

Kapetanakis, T.N., I.O. Vardiambasis, G. Liodakis, and A. Maras. 2012. Neural network solution of the circular loop antenna radiation problem. 20th Telecommunications Forum (TELFOR 2012), Belgrade, Serbia: 1193-1196.

Kapetanakis, T.N., I.O. Vardiambasis, E.I. Lourakis, and A. Maras. 2018a. Applying neuro-fuzzy soft computing techniques to the circular loop antenna radiation problem. IEEE Antennas and Wireless Propagation Letters, 17 (9): 1673–1676.

Kapetanakis, T.N., I.O. Vardiambasis, M.P. Ioannidou, and A. Maras. 2018b. Neural network modeling for the solution of the inverse loop antenna radiation problem. IEEE Transactions on Antennas and Propagation, 66: 6283–6290.

Kapetanakis, T.N., I.O. Vardiambasis, M.P. Ioannidou, and A.I. Konstantaras. 2021. Chapter 7 in Recent Trends on Electromagnetic Environmental Effects for Aeronautics and Space Applications, IGI Global: 186-225.

Kishk, A.A., R.P. Parricar, and A.Z. Elsherbeni. 1992. Electromagnetic scattering from an eccentric multilayered circular cylinder. IEEE Transactions on Antennas and Propagation, 40 (3): 295-303.

Konistis, K. and J.L. Tsalamengas. 1997. Plane wave scattering by an array of bianisotropic cylinders enclosed by another one in an unbounded bianisotropic space: Oblique incidence. Journal of Electromagnetic Waves and Applications, 11 (8): 1073-1090.

Konstantaras, A. 2020. Deep learning and parallel processing spatio-temporal clustering unveil new Ionian distinct seismic zone. Informatics, 7, 39.

Kumar, C. and D.L. Jain. 1993. Scattering of electromagnetic plane waves by an arbitrary dielectric infinite cylinder. International Journal of Mathematical Education in Science and Technology, 24 (2), 251-265.

Liodakis, G., D. Arvanitis, and I.O. Vardiambasis. 2004. Neural network based digital receiver for radio communications. WSEAS Transactions on Systems, 3 (10): 3308-3313.

MathWorks, The Inc. 2019. Deep Learning Toolbox v12.1 (2019a), Natick, Massachusetts, United States.

Millar, R. 1960. The scattering of a plane wave by a row of small cylinders. Canadian Journal of Physics, 38 (2): 272-289.

Mishra, R.K. 2001. An overview of neural network methods in computational electromagnetics. International Journal of RF and Microwave Computer-Aided Engineering, 12: 98–108.

Mishra, S., R.N. Yadav, and R.P. Singh. 2015. Directivity estimations for short dipole antenna arrays using radial basis function neural networks. IEEE Antennas and Wireless Propagation Letters, 14: 1219–1222.

Olaofe, G.O. 1970. Scattering by two cylinders. Radio Science, 5 (11): 1351-1360.

Osipov, A.V. and S.A. Tretyakov. 2017. Modern Electromagnetic Scattering Theory with Applications. Wiley.

Parrikar, R.P., A.A. Kishk, and A.Z. Elsherbeni. 1991. Scattering from an impedance cylinder embedded in a nonconcentric dielectric cylinder. IEE Proceedings H - Microwaves, Antennas and Propagation, 138 (2): 169-175.

Ragheb, H.A. and M. Hamid. 1985. Scattering by N parallel conducting circular cylinders. International Journal of Electronics, 59 (4): 407-421.

Roumeliotis, J.A., J.G. Fikioris, and G.P. Gounaris. 1980. Electromagnetic scattering from an eccentrically coated infinite metallic cylinder. Journal of Applied Physics, 51 (8): 4488-4493.

Roumeliotis, J.A. and N.B. Kakogiannos. 1994. Scattering from an infinite cylinder of small radius embedded into a dielectric one. IEEE Transactions on Microwave Theory and Techniques, 42 (3): 463-470.

Roumeliotis, J.A. and A.-P. Ziotopoulos. 2000. Electromagnetic scattering by a circular cylinder parallel with another one of small radius. Journal of Electromagnetic Waves and Applications, 14 (1): 27-43.

Sergaki, E., G. Spiliotis, I.O. Vardiambasis, T. Kapetanakis, A. Krasoudakis, G.C. Giakos, M. Zervakis, and A. Polydorou. 2018. Application of ANN and ANFIS for detection of brain tumors in MRIs by using DWT and GLCM texture analysis. International Conference on Imaging Systems & Techniques (IST 2018): 1–6.

Stratigaki, L.G., M.P. Ioannidou, and D.P. Chrissoulidis. 1996. Scattering from a dielectric cylinder with multiple eccentric cylindrical dielectric inclusions. IEE Proceedings – Microwaves, Antennas and Propagation, 143 (6): 505-511.

Toyama, H. and K. Yasumoto. 2003. Electromagnetic scattering from a dielectric cylinder with multiple eccentric cylindrical inclusions. Progress In Electromagnetics Research, 40: 113-129.

Tsalamengas, J.L., I.O. Vardiambasis, and J.G. Fikioris. 1995. Plane-wave scattering by strip-loaded circular dielectric cylinders in the case of oblique incidence and arbitrary polarization. IEEE Transactions on Antennas and Propagation, 43 (10): 1099-1108.

Uzunoglu, N.K. and J.G. Fikioris. 1979. Scattering from an infinite dielectric cylinder embedded into another. Journal of Physics A: Mathematical and General, 12 (6): 825-834.

Vardiambasis, I.O., G. Liodakis, G. Karonis, and J.P. Makris. 2004. Studying electromagnetic scattering by dielectric cylinders: an engineering electromagnetics' exercise at the Technological Educational Institute of Crete. WSEAS Transactions on Advances in Engineering Education, 1 (1): 77-82.

Vardiambasis, I.O., T.N. Kapetanakis, C.D. Nikolopoulos, T.K. Trang, T. Tsubota, R. Keyikoglu, A. Khataee, and D. Kalderis. 2020. Hydrochars as emerging biofuels: Recent advances and application of artificial neural networks for the prediction of heating values. Energies, 13(17), 4572: 1-20.

Yousif, H.A. and S. Kohler. 1988. Scattering by two penetrable cylinders at oblique incidence: I. The analytical solution. Journal of the Optical Society of America A, 5 (7): 1085-1096.

Yousif, H.A. and S. Kohler. 1988. Scattering by two penetrable cylinders at oblique incidence: II. Numerical exambles. Journal of the Optical Society of America A, 5 (7): 1097-1103

ISSN 2654-2099 **ISBN 978-618-84774-3-8**